New Physics Search in Dijet Mass Spectrum with Compact Muon Solenoid

by

Chiyoung Jeong

A Dissertation

In

PHYSICS

Submitted to the Graduate Faculty
of Texas Tech University in
Partial Fulfillment of
the Requirements for
the Degree of

DOCTOR OF PHILOSOPHY

Approved

Sung-Won Lee
Chair of Committee

Nural Akchurin

Robert Harris

Juyang Huang

Igor Volobouev

Peggy Gordon Miller
Dean of the Graduate School

December, 2011

Acknowledgements

I am grateful to my supervisor Sung-Won Lee for his encouragement and advice. Whenever I lost track, he led me in the right direction. I feel honored I had him as my supervisor. I am beholden to Robert Harris for all his support and guidance. I was able to finish this dissertation because he led me in this analysis. He showed how scientists work. He is the best mentor for any graduate students.

I also want to thank all the people who were involved in dijet analysis (John Paul Chou, Selda Esen, Kazim Ziya Gumus, Maxime Gouzevitch, Kenichi Hatakeyama, Jim Hirschauer, Jason st. John, Konstantinos Kousouris, Kalanand Mishra, Sertac Ozturk, Marek Zelinski). I learned a lot of things through these people.

I really appreciate Dan Green for giving me a chance to work at LPC. Working at LPC as a graduate student for the last three years was really a good experience. I'll miss it. I would like to thank other LPC members for your help and friendship.

Finally I do not know how to thank my parents Byung-Joo Jang and Jae-Mook Jeong, my wife Youn Jung Roh, and my son Thomas Hansun Jeong for their support. I can be here because of them. I cannot imagine my life without them.

Table of Contents

Abstract

Many extensions of the SM predict the existence of new massive objects that couple to quarks and gluons and result in resonances in the dijet mass spectrum. In this thesis we present a search for narrow resonances in the dijet mass spectrum using data corresponding to an integrated luminosity of 1 fb^{-1} collected by the CMS experiment at the LHC, at a proton-proton collision energy of $\sqrt{s} = 7\ TeV$. The dijet mass distribution of two leading jets is measured and compared to QCD predictions, simulated by PYTHIA with the CMS detector simulation. We select events which have two leading jets with $\mid \Delta\eta \mid < 1.3$ and $\mid \eta \mid < 2.5$. We fit the dijet mass spectrum with QCD parameters. Since no evidence of new physics was found, we set upper limits at 95% CL on the resonance cross section and compare to the theoretical prediction for several models of new particles: string resonances, axigluons, colorons, excited quarks, E_6 diquarks, Randall-Sundrum gravitons, W' and Z'. We exclude at 95% CL string resonances in the mass range $1.0 < M(S) < 4.00$ TeV, excited quarks in the mass range $1.0 < M(q*) < 2.49$ TeV, axigluons and colorons in the mass range $1.0 < M(A) < 2.47$ TeV, E_6 diquarks in the mass range $1.0 < M(D) < 3.52$ TeV, and W' bosons in the mass range $1.0 < M(W') < 1.51$ TeV.

List of Tables

List of Figures

List of Abbreviations

ALICE : A Large Ion Collider Experiment

ATLAS : A Toroidal LHC ApparatuS

CDF : Collider Detector at Fermilab

CERN : European Organization for Nuclear Research

CL : Confidence Level

CMS : Compact Muon Solenoid

CSC : Cathode Strip Chamber

CTEQ : Coordinated Theoretical Experimental project on QCD

DT : Drift Tube

ECAL : Electromagnetic CALorimeter

ES : Endcap preShower

HB : Hadronic Barrel

HCAL : Hadronic CALorimeter

HE : Hadronic Endcap

HF : Hadronic Forward

HLT : High Level Trigger

HO : Hadronic Outer

JES : Jet Energy Scale

JER : Jet Energy Resolution

L1T : level 1 trigger

LHC : Large Hadron Collider

LHCb : Large Hadron Collider Beauty experiment

LINAC : LINear ACcelerator

MC : Monte Carlo

MET : Missing E_T

PDF : Parton Distribution Function

PF : Particle Flow

PS : Proton Synchrotron

QCD : Quantum Chromo Dynamics

QED : Quantum Electro Dynamics

RPC : Resistive Plate Chamber

SM : Standard Model

SPS : Super Proton Synchrotron

TEC : The two End Cap detector system

TIB : The Inner Barrel detector system

TID : The Inner Discs detector system

TOB : The Outter Barrel detector system

Chapter 1

Introduction

Mankind has long tried to explain what comprises the world we live in and how the elementary particles interact with each other. Many theories have been established and have been verified or abandoned through experiments. In the 1960s, Sheldon Glashow, Steven Weinberg, and Abdus Salam established SM. The SM has been verified by the experiments except the existence of Higgs boson has never been discovered. Although the SM has succedded in present data, it is believed that SM is not the completed theory since it leaves many unanswered questions. Why do quarks coms in different flavors? Why are there generations? How do we unify gravitation with other forces? Why is gravity so weak? and many other questions.. Theories have appeared to answer questions to the SM. Among those theories, some of them anticipate short lived particles, called resonances decaying to two jets (dijet). This thesis shows how we search those resonances at CMS which is one of the experiments of the LHC. Theoretical motivation behind this study is written in Chapter 1. Chapter 2 gives the brief introduction of the LHC and CMS. Chapter 3 shows how data was handled and what dijet mass spectrum of data looks like. Chapter 4 covers signal shape study and setting excluded mass range. Chapter 5 discusses the systematic uncertainties. Results are presented in the Chapter 6. Finally the conclusion is in Chapter. 7.

1.1 Jet Production

A coupling constant(α_s) determines the strength of an interaction. The QCD coupling constant is given by

$$\alpha_s(Q^2) = \frac{12\pi}{(33-2n_f)ln(\frac{Q^2}{\Lambda^2})} \tag{1.1}$$

where Q is the magnitude of momentum transferred in the interaction, n_f is the number of quark flavor, and Λ is defined by

$$\Lambda^2 = \mu^2 exp(\frac{-12\pi}{(33-2n_f)\alpha_s(\mu^2)}) \tag{1.2}$$

where μ is the normalization scale. As Eq. 1.1 shows, the interaction becomes weak when interaction transfers large momentum. This is called "asymptotic freedom," so quark can be free from hadron when $Q \to \infty$. When the coupling constant decreases with Q^2, the color force increases as distance between quarks increase. This increasing color force makes new quark-antiquark pairs from vacuum. This is called "color confinement." These quark-antiquark pairs then create lots of colorless particles (mesons and baryons). This process is called hadronization, fragmentation or string breaking. Fig. 1.1 shows the parton model picture of this process in QCD. These hadrons scatters at wide angles into outgoing partons and can be collected with cone shape. This collection is called jet.

The cross section is the probability of the given process between initial state and a final state. The cross section for the hadronic reaction $a+b \to c+d$ is given by

$$\sigma(a+b \to c+d) = \sum_{ij} f_i^{(a)}(x_a, Q^2) f_j^{(b)}(x_b, Q^2) \hat{\sigma}(i+j \to c+d) \tag{1.3}$$

where x_a, x_b are the fraction of momenta of hadron including the parton a and b; $f_i^{(a)}$ and $f_j^{(b)}$ are the probability of finding constituent i and j in the hadron a and b; $\hat{\sigma}$ is the short-

distance cross section for the elementary process leading to the final state, and Q is a hard scattering scale.

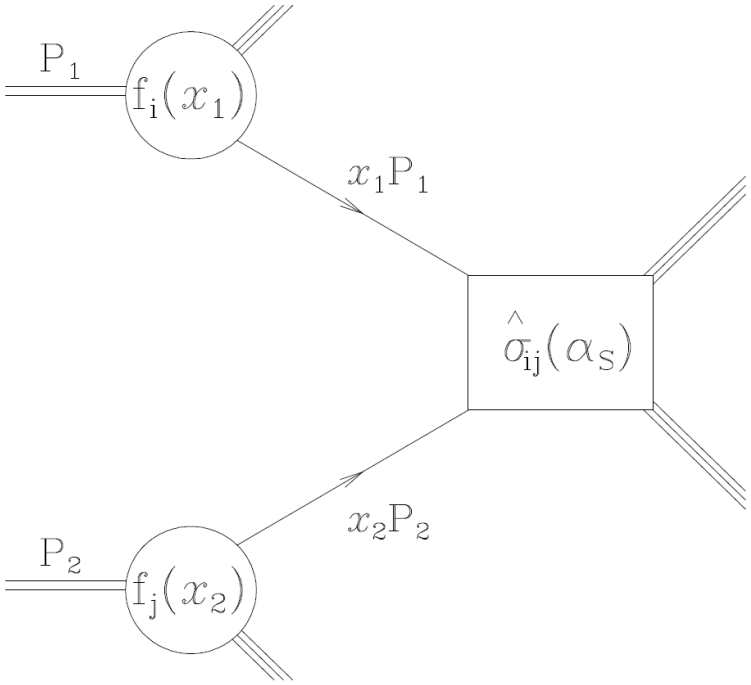

Figure 1.1: The parton model description of a hard scattering process [1]

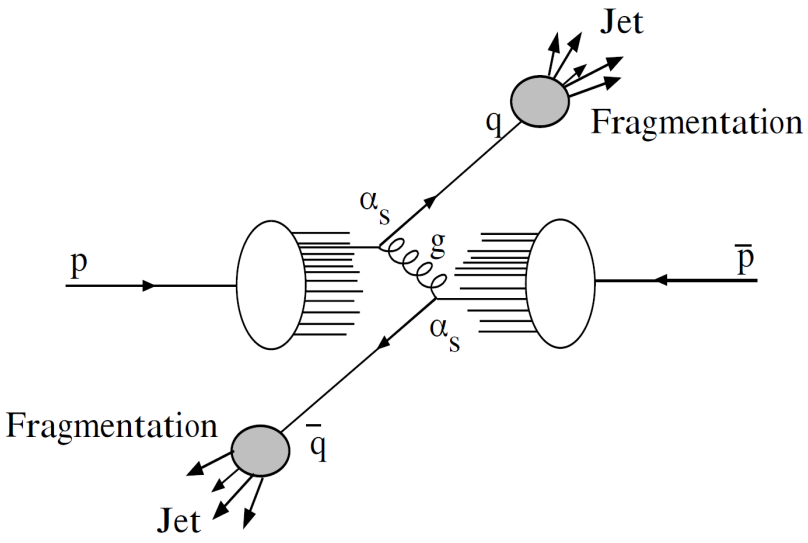

Figure 1.2: Jet production in a hadron collision.

1.2 Dijet Production

This analysis searchs for a process which produce narrow resonances which decay to dijets as shown in Fig. 1.3: $pp \rightarrow X \rightarrow$ jet + jet (inclusive).

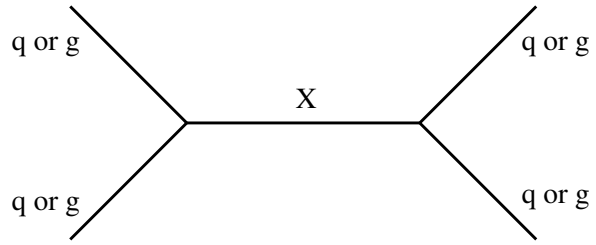

Figure 1.3: Feynman Diagram of dijet resonance. The initial state and final state both contain two partons (quarks, antiquarks or gluons) and the intermediate state contains an s-channel resonance X.

This analysis looks at the dijet mass distribution to see if it agrees with expectation of SM or shows evidence of new physics. In this research, eight different dijet resonance models were searched. These resonances have narrow width so they can be easily detected. Table 1.1 shows some properties of these models.

Table 1.1: Properties of Some Resonance Models

Model Name	X	Color	J^P	$\Gamma/(2M)$	Chan
Excited Quark	q*	Triplet	$1/2^+$	0.02	qg
E_6 Diquark	D	Triplet	0^+	0.004	qq
Axigluon	A	Octet	1^+	0.05	$q\bar{q}$
Coloron	C	Octet	1^-	0.05	$q\bar{q}$
RS Graviton	G	Singlet	2^+	0.01	$q\bar{q}$, gg
Heavy W	W'	Singlet	1^-	0.01	$q\bar{q}$
Heavy Z	Z'	Singlet	1^-	0.01	$q\bar{q}$
String	S	mixed	mixed	$0.003-0.037$	qg, $q\bar{q}$, gg

At the end of this chapter, Fig. 1.4 and Table 1.2.7 show cross section $\times$ branching ratio $\times$ kinematic acceptance for dijet resonances in pp collisions at $\sqrt{s} = 7$ TeV with the eta cuts $|\Delta\eta| < 1.3$ and $|\eta| < 2.5$ on the two jets for 8 different resonance models.

1.2.1 Axigluon

Chiral color is an one of the theories used to explain beyound SM. [2] It seems true that unbroken gauge group is the $SU(3)_C$ of QCD and QED. In chiral color, QCD comes from a spontaneous breakdown of a larger gauge group $SU(3)_L \times SU(3)_R$. One prediction of chiral color model is the axigluon particle which produced from quark-antiquark interaction. The axigluon has a strong gauge coupling to all quark by the gauge symmetry: [3]

$$\mathscr{L}_A = -ig_s t^a_{ij} q^{-i} \gamma_5 \gamma_\mu A^{\mu a} q^j \tag{1.4}$$

where the t_{ij} are the usual $SU(3)$ color matrices. The Axigluon cannot be produced from gluon-gluon interaction because of the parity conservation. In p-p collision, Axigluon is produced mainly from sea - valence quark collisions. [3] The width of the axigluon is

$$\Gamma_A = \frac{N_A \alpha_s m_A}{6} \tag{1.5}$$

where m_A is mass of the axigluon, α_s is QCD coupling constant, and N_A is the number of open decay channel.

Branching fraction into jets of axigluon is 1 when $m_A < 2m_t$ where, m_t is mass of top quark and [3]

$$BR(A \to q\bar{q}) = \frac{1}{5 + [1 - (2m_t/m_A)^2]^{3/2}} (m_A > 2m_t) \tag{1.6}$$

The total cross section for axigluon production is given by integrating the differential cross section in the narrow width approximation

$$\sigma = \int_{y_b^{min}}^{y_b^{max}} \frac{16\pi^2 \alpha_s}{9s} L(x_p, x_{\bar{p}}) A(y_b, y_{cut}, cos\theta^*_{cut}) dy_b \tag{1.7}$$

where the minimum boost is $y_b^{min} = max(-y_{cut}, ln\sqrt{\tau})$, the maximum boost is $y_b^{max} = min(y_{cut}, -ln\sqrt{\tau})$, and $\tau = M^2/s = x_p x_{\bar{p}}$. The parton luminosity $L(x_p, x_{\bar{p}})$ is given by

$$\sum_i (q_i(x_p)\bar{q}_i(x_{\bar{p}}) + \bar{q}_i(x_p)q_i(x_{\bar{p}})) \tag{1.8}$$

$A(y_b, y_{cut}, cos\theta^*{}_{cut})$ is the acceptance for the jet rapidity and $cos\theta^*{}_{cut}$ is the cut which is evaluated at each value of y_b within the integral using the axial-vector decay angular distribution:

$$\frac{dN}{dcos\theta^*} = 1 + cos\theta^* \tag{1.9}$$

This cross section is then multipilied by Eq. 1.6 to obtain the cross section times branching ratio we compare to our limit.

1.2.2 Coloron

A flavor-universal coloron model was introduced to explain the apparent excess of high-E_T jets in the inclusive jet spectrum measured by the collider detector at Fermilab collaboration [4]. Also the flavor-universal coloron model gives an explanation why there are different quark flavors. In the flavor-universal coloron model, the strong gauge group is extended to $SU(3)_1 \times SU(3)_2$ with gauge coupling ξ_1 and ξ_2 respectively, $\xi_2 \gg \xi 1$ [4]. The original gauge bosons mix to form a color octet of massless gluons and a color octet of massive colorons [5]. The gluons interact with quarks through a conventional QCD coupling with strength g_3. The colorons ($C^{\mu a}$) interact with quarks through a new QCD-like coupling. [5] :

$$\mathscr{L} = -g_3 cot\theta J^a_\mu C^{\mu a} \tag{1.10}$$

where J^a_μ is the color current: [5]

$$\sum_f \bar{q}_f \gamma_\mu \frac{\lambda^a}{2} q_f \tag{1.11}$$

and $cot\theta = \xi_2/\xi_1$. The colorons decay to all adequately light quarks. When there are n flavors lighter than $M_c/2$, where M_2 is coloron mass, the decay width is [5]

$$\Gamma_C \approx \frac{n}{6}\alpha_s cot^2\theta M_C \tag{1.12}$$

where $\alpha_s = g_3^2/4\pi$ and $cot\theta$ is expected to be greater than 1. The values of colorons with mixing $cot\theta = 1$ such as width, coupling strength to quark, and production cross sections times branching ratio for jet are same as them of axigluons. Since the cross sections times branching ratio for jet is increasing as the $cot\theta$ is increasing [5], the excluded mass region of $cot\theta = 1$ also excludes mass region with $cot\theta > 1$.Because of this, we use axigluon cross section for colorons in this analysis.

1.2.3 E_6 Diquarks

Superstring theory is another alternative theory for beyond SM. String theory in 10 dimensions is anomaly free if the gauge group is $E_8 \times E_8$ or SO(32). [6] $E_8 \times E_8$ is interesting since in $E_8 \times E_8$ allows chiral fermion while SO(32) does not. Because the fermions of the SM form chiral representations, $E_8 \times E_8$ can contain the SM. To make connection with our four-dimensional world, the extra six dimensions need to be compactified. Compactification on Calabi-Yau manifold results in the breaking $E_8 \to SU(3) \times E_6$ and lead E_6 as the grand unification group for the strong and electroweak interactions. [7] The E_6 models contain color triplet scalar diquarks $D(D^c)$ and have charge $\pm 1/3$. The E_6 models couple to $\bar{u}\bar{d}(ud)$. The interaction lagrangian for transitions between E_6 diquarks and up and down quark is [3]

$$\mathscr{L} = \lambda\varepsilon_{ijk}\bar{u}^{ci}\cdot\frac{1}{2}(1-\gamma_5)d^j D^k + \frac{1}{2}\lambda_c\varepsilon_{ijk}\bar{\mu}^i\cdot\frac{1}{2}(1+\gamma_5)d^{cj}D^{ck} + h.c. \tag{1.13}$$

where, λ and λ_c are Yukawa-type couplings($\lambda = \lambda_c = e$), i, j, k are colour indices and $m_D = m_{D^c}$. [3]. The width of E_6 diquarks is [7] :

$$\Gamma_D = \alpha M_D, \quad \Gamma_{D^c} = \alpha M_{D^c}/4 \tag{1.14}$$

where $\alpha = \lambda^2/4\pi$ is the electromagnetic coupling constant. α is 1/128 after running to high masses. E_6 diquarks in the first family decay into u and d quarks only.

Differential cross section is:

$$\frac{d^2\sigma}{dx_p dx_{\bar{p}}} = \frac{\hat{s}}{108\pi} \frac{16\lambda}{(\hat{s}-M_D^2)^2+\Gamma_D^2 M_D^2} [\bar{u}(x_p)\bar{d}(x_{\bar{p}}) + \bar{u}(x_{\bar{p}})\bar{d}(x_p)]P \tag{1.15}$$

and similarly for $\bar{D}$ with $\bar{q} \to q$ in the parton distributions. The cross section for D^c is:

$$\frac{d^2\sigma}{dx_p dx_{\bar{p}}} = \frac{\hat{s}}{108\pi} \frac{\lambda}{(\hat{s}-M_{D^c}^2)^2+\Gamma_{D^c}^2 M_{D^c}^2} [u(x_p)d(x_{\bar{p}}) + u(x_{\bar{p}})d(x_p)]P \tag{1.16}$$

and similarly for $\bar{D}^c$ with $q \to \bar{q}$ in the parton distributions. $\hat{s} = s x_{\bar{p}} x_p$ and the variable P is the kinematic acceptance. For the convenience, we integrate Eq. 1.15 and 1.16, over variables $m = \sqrt{s}$ and $y_b = (y_1 + y_2)/2 = (1/2) ln(x_p/x_{\bar{p}})$ using $dm dy_b = (s/2m) dx_{\bar{p}} dx_p$ from y_b^{min} to y_b^{max} to obtain the Breight-Wigner $d\sigma/dm$ for the diquark resonance. The kinematic acceptance is

$$P = P(y^{cut}, cos\theta^*) \tag{1.17}$$

which is the probability that both final state partons pass our cuts in rapidity and $cos\theta^* = tanh(y^*) = tanh(y_1 - y_2)$ as a function of the variable y_b.

1.2.4 Excited Quarks

The three generations of quarks and leptons might be a hint of composite structures which are made up of constituents. The existence of a quark substructure can be found from dijet mass spectrum as excited quarks. Only 1/2 spin and isospin of the excited states of the first generation is considered to limit the number of parameters. The coupling between excited (right-handed) quarks, ordinary (left-handed) quarks, and gauge boson is given by

the effective Lagrangian of the magnetic moment type [8]

$$\mathscr{L} = \frac{1}{2M^*}\bar{q}_R^*\sigma^{\mu\nu}(g_s f_s \frac{\lambda_a}{2}G_{\mu\nu}^a + gf\frac{\tau}{2}W_{\mu\nu} + g'f'\frac{Y}{2}B_{\mu\nu})q_L + h.c. \tag{1.18}$$

where M^* is excited quark mass; $G_{\mu\nu}^a$, $W_{\mu\nu}$, and $B_{\mu\nu}$ are the field-strength tensors of the SU(3), SU(2), and U(1) gauge fields; λ_a, τ, and Y are the corresponding gauge structure constants; and f_s, f, and f' are parameters determined by the composite dynamics and assumed as one. [8] For the decay of excited quarks into ordinary quarks and gluons, the partial width is given by :

$$\Gamma(q^* \to qg) = \frac{1}{3}\alpha f_s^2 M^* \tag{1.19}$$

The q^* full width for $f_s = f = f'$ is

$$\Gamma(q^*) \approx 0.04 f^2 M^* \tag{1.20}$$

which for $f \leq 1$ is narrower than our dijet mass resolution. The Branching ratio can be found in Table 1.2

Table 1.2: The decay modes and the branching ratios of excited up and down quarks for $f_s = f = f'$ and α_s =0.1

Decay Mode	Br. Ratio(%)	Decay Mode	Br. Ratio(%)
$u^* \to ug$	83.4	$d^* \to dg$	83.4
$u^* \to u\gamma$	2.2	$d^* \to d\gamma$	0.5
$u^* \to dW$	10.9 (e ν 1.2)	$d^* \to uW$	10.9
$u^* \to uZ$	3.5 (ee 0.27)	$d^* \to dZ$	5.1

Total cross section of excited quark is given by calculating the Breit-Wigner differential cross section versus dijet mass and integrating over dijet mass. The differential cross section is [8] :

$$\frac{d\sigma}{dm} = \frac{2}{m}\int_{y_b^{min}}^{y_b^{max}} \tau L(x_1,x_2)\hat{\sigma}(m^2)P dy_b \tag{1.21}$$

where τ is initial state related radiation by $\tau = x_1 x_2 = m^2/s$ (x_1,x_2 are initial state parton

fractional momenta); y_b is a kinematic variable which is given by $y_b = (y_{jet1} + y_{jet2})/2 = (1/2)ln(x_1/x_2)$; rapidity y is equal to pseudorapidity η assuming massless partons. The partonic luminosity function is the product of PDF:

$$\mathscr{L}(x_1,x_2) = q(x_1,m^2)g(x_2,m^2) + g(x_1,m^2)q(x_2,m^2) \tag{1.22}$$

From Breit-Wigner like resonance formula for an excited quark of mass M^* we can get the subprocess cross section following

$$\hat{\sigma}(m^2) = \pi \frac{\hat{\Gamma}^2(qg \to q^*)\hat{\Gamma}(q^* \to qg)}{(m^2 - M^{*2})^2 + \hat{\Gamma}(q^*)M^{*2}} \tag{1.23}$$

where $\hat{\Gamma}(q^*)$, is the full width of the q^* resonance from all decay channels, and $\hat{\Gamma}(qg \to q^*)$ is roughly the partial width in the qg channel. Finally, the probability P is the probability that both final state partons pass our rapidity cuts and p_T cut as a function of τ and y_b.

1.2.5 W' and Z'

The W' and Z' arise from various theories beyond SM. Finding W' and Z' could give us clues about what is extra dimension and how elementary particles have mass. Here we assume the W' and Z' have same production cross section and same fractional width as the W and Z since W' and Z' have almost similar characters as W and Z except mass. Subprocess cross section expression for W and Z production in reference [9] is used for W' and Z' with the Fermi constant, G_F, replaced by

$$G'_F = G_F(\frac{M}{M'}) \tag{1.24}$$

where M is the mass of the W and Z and M' is the mass of the W' and Z'. From Tevatron experiment, K factor is introduced. The K factor is multiplied to the lowest order SM cross

sections to take into account higher order terms. The K factor for W' is

$$K = 1 + \frac{8\pi\alpha_s}{9} \approx 1.3. \tag{1.25}$$

The K factor for Z' is

$$K = 1 + \frac{\alpha_s}{2\pi}\frac{4}{3}(1 + \frac{4}{3}\pi^2) \approx 1.3. \tag{1.26}$$

The total cross section is then calculated in the narrow width approximation. The angular distribution of these vector particles is handled in the same way as for the axigluon previously. The width of the W' is

$$\Gamma(W') = 2GeV\frac{M'_W}{M_W}. \tag{1.27}$$

The width of the Z' is

$$\Gamma(Z') = 2.5GeV\frac{M'_Z}{M_Z}. \tag{1.28}$$

These widths are significantly less than dijet mass resolution. The branching ratios for W' and Z' in the dijet channel is equal to the branching ratio to quarks other than the top quark.

1.2.6 Randall Sundrum Graviton

Randall Sundrum model predicts massive spin-2 graviton which is Kaluza-Klein resonance that result from the compactified extra dimensions. This is called Randall Sundrum graviton. [10] There are effectively only two parameters in the model. They are the mass of the light graviton resonance and a coupling strength parameter $k/\bar{M}_{PL}$, where k is Planck scale constant and M_{PL} is Planck mass. This analysis uses $k/\bar{M}_{PL} = 0.1$. With the narrow width approximation, the lowest order differential cross section for the Randall Sundrum graviton per unit of center-of-mass scattering angle $cos\theta$ and boost η is [11]

$$\frac{d\sigma}{dcos\theta d\eta_B} = \frac{1}{G_i}(\frac{2M}{s}\frac{\pi}{2}\Gamma)(\frac{20\pi}{M^2}B_iB_f\frac{1}{C_i})F(cos\theta^*)f(x_p)f(x_{\bar{p}}) \tag{1.29}$$

where M is mass of Randall Sundrum graviton; Γ is width of Randall Sundrum graviton; the boost $\eta_B = (\eta_1 + \eta_2)/2$ is average pseudorapidity of the final state partons; s is the square of the proton-proton collision energy; C_i is the color of the initial state (3 for $q\bar{q}$ and 8 for gg); B_i and B_f are the branching fractions for the initial state and the final state respectively; f(x_p) and f($x_{\bar{p}}$) are the parton distributions of the initial state; and $F(cos\theta^*)$ are the normalized angular distributions of the sub-process: [10]

$$F(gg \to G \to q\bar{q}) = F(q\bar{q} \to G \to gg) = \frac{5}{8}(1 - cos^4\theta) \quad (1.30)$$

$$F(gg \to G \to gg) = \frac{5}{32}(1 + 6cos^2\theta + cos^4\theta) \quad (1.31)$$

$$F(q\bar{q} \to G \to q\bar{q}) = \frac{5}{8}(1 - 3cos^2\theta + 4cos^4\theta). \quad (1.32)$$

The final state branching fractions are given by the ratio of the partial widths to the full width, where the partial width for photon is [12]

$$\Gamma(G \to \gamma\gamma) = \frac{2x_1^2}{160\pi}(\frac{k}{\bar{M}_{Pl}})^2 M, \quad (1.33)$$

for gluon is

$$\Gamma(G \to gg) = \frac{2x_1^2}{20\pi}(\frac{k}{\bar{M}_{Pl}})^2 M, \quad (1.34)$$

for each variety of lepton is

$$\Gamma(G \to l\bar{l}) = \frac{2x_1^2}{320\pi}(\frac{k}{\bar{M}_{Pl}})^2 M, \quad (1.35)$$

for each variety of light quark (u,d,s,c or b) is

$$\Gamma(G \to q\bar{q}) = \frac{6x_1^2}{320\pi}(\frac{k}{\bar{M}_{Pl}})^2 M, \quad (1.36)$$

for the top quark is

$$\Gamma(G \to t\bar{t}) = \frac{6x_1^2}{320\pi}(\frac{k}{\bar{M}_{Pl}})^2 M(1-\frac{4m_t^2}{M^2})^{3/2}(1+\frac{8m_t^2}{3M^2}), \tag{1.37}$$

for the W boson is

$$\Gamma(G \to W^+W^-) = \frac{2x_1^2}{80\pi}(\frac{k}{\bar{M}_{Pl}})^2 M(1-\frac{4m_W^2}{M^2})^{3/2}(\frac{13}{12}+\frac{14m_W^2}{3M^2}+\frac{4m_W^4}{M^4}), \tag{1.38}$$

and for the Z boson is

$$\Gamma(G \to ZZ) = \frac{x_1^2}{80\pi}(\frac{k}{\bar{M}_{Pl}})^2 M(1-\frac{4m_Z^2}{M^2})^{3/2}(\frac{13}{12}+\frac{14m_Z^2}{3M^2}+\frac{4m_Z^4}{M^4}), \tag{1.39}$$

where $x_1 = 3.8317$ is the first zero of the Bessel function $J_1(x)$ of order 1. [12] The full width $\Gamma(G)$ is the sum of the partial widths. For $\frac{k}{\bar{M}_{Pl}} = 0.1$, the percent of the width Γ/M is about 1%. The final state branching fractions B_f can be obtained by partial widths divided by the full width. The initial state branching fractions for quarks are identical to the final state branching fractions for quarks. The initial state branching fractions for gluons are twice the final state branching fractions for gluons, to remove a factor of 1/2 for identical particles in the final state. All other differences between quarks and gluons about spin and color statistics are already included in Eq. 1.32. The total cross section at lowest order is

$$\sigma = \int\int \frac{d\sigma}{dcos\theta d\eta_B} dcos\theta d\eta_B. \tag{1.40}$$

1.2.7 String Resonance

String theory is the theory which makes the connection between relativistic quantum field theory and general relativity. One prediction of string theory is that scattering amplitudes are modified near the string scale. This modification would appear as dijet resonance corresponding to excited string states. [13] [14] The physical process of dijet production at

the LHC is the collisions of two partons, producing two final partons that fragment into hadronic jets. The leading order $2 \to 2$ Veneziano scattering amplitudes in any string theory may be represented as field theory amplitudes modified by a universal form factor in the appropriate kinematic channels. [13] The Veneziano form factor as a function of Mandelstam variables s, t, u (constrained by $s+t+u=0$) is [13]:

$$V(s,t,u) = \frac{su}{tM_s^2} B(-s/M_s^2, -u/M_s^2) = \frac{\Gamma(1-s/M_s^2)\Gamma(1-u/M_s^2)}{\Gamma(1+t/M_s^2)} \tag{1.41}$$

where, M_s is mass scale of strings. By applying the expansion in term of s-channel resonance, the physical content of the form factor becomes clear. [15]

$$B(-s/M_s^2, -u/M_s^2) = -\sum_{n=0}^{\infty} \frac{M_s^{2-2n}}{n!} \frac{1}{s-nM_s^2} \times [\prod_{J=1}^{n}(u+M_s^2 J)] \tag{1.42}$$

which shows it has s-channel poles related to the propagation of virtual Regge excitation with mass $\sqrt{n}M_s$. Thus near the nth level pole ($s \to nM_s^2$):

$$V(s,t,u) \approx \frac{1}{s-nM_s^2} \times \frac{M_s^{2-2n}}{(n-1)!} \prod_{J=0}^{n-1}(u+M_s^2 J) \tag{1.43}$$

where J is the spin. The first Regge excitations at level n=1 includes excited gluons of spin $J=1,2$ ($g^*_{1,1}$ and $g^*_{1,2}$) and excited quarks of spin $J=\frac{1}{2},\frac{3}{2}$ ($q^*_{1,\frac{1}{2}}$ and $q^*_{1,\frac{3}{2}}$) with mass equal to the string scale. For s-channel scattering at a hadron collider, all these excitations contribute to produce a dijet resonance at the string scale. The specific form of $2 \to 2$ string scattering amplitudes depends on details of the string theory model. However, there are certain model-independent features that follow from Regge excitations that must exist in certain channels of string theory at the TeV scale. The model-independent Regge excitations that are included here are in channels that have the same flavor quantum numbers as those of massless particles in the SM. In Appendix. A, the matrix elements for all strongly interacting $2 \to 2$ parton level scattering processes that are modified by Veneziano form

factors in the appropriate channels are shown with this restriction.

This modified scattering amplitude allows model independent probe of the string scale by using dijet resonance search. The resonant matrix elements squared in this limit may be obtained from the ones given above. To obtain it, we replace the propagator factor of any Veneziano form factor that involves the s-channel with a Breit-Wigner form in that channel for $n = 1$ only, and ignore any interference between the s and t or u channels. In this limit, all Veneziano form factors in the matrix element squared may then be neglected except for the squares of ones that involve the s-channel

$$\frac{|V(s,y)^2|}{y^2} \simeq \frac{1}{(s-m_s^2)^2+m_s^2\Gamma^2} \tag{1.44}$$

where $y \in (t,u)$ and $\Gamma \equiv \Gamma(Initial \to R^{(1)} \to All)$ is the total width of the coherent superposition of $n = 1$ Regge excitations arising from initial state parton scattering channel. The By using the optical theorem width of the $n = 1$ Regge excitations in a given channel may be obtained from the residue of the leading order (ignoring the finite width) total cross sections near the n = 1 s-channel pole after dividing by the wave function factor for the external states obtained from the residue of the forward scattering amplitude

$$\frac{1}{m_S}\Gamma(Initial \to R^{(1)} \to All) = m_s^2 \frac{Res_2[\sigma(Initial \to R^{(1)} \to All)]}{Res_i[\mathscr{M}(Initial \to Initial)]} \tag{1.45}$$

where $Res_k[f(s)] = f(s)(s-m_s^2)^k$ extracts s-channel pooles. From this relation and matrix elements above, the decay total widths on the first Regge excitations for all non-trivial initial state helicity and color configuration $2 \to 2$ QCD scattering on these resonances are

$$\frac{1}{m_s}\Gamma(q_i^{\pm} g_a^{\pm} \to R^{(1)} \to All) = \alpha_s(\frac{1}{8}\mathbf{P_{15}}^{ai} + \frac{1}{8}\mathbf{P_{\bar{6}}}^{ai} + \frac{1}{24}\mathbf{P_3}^{ai}) \tag{1.46}$$

$$\frac{1}{m_s}\Gamma(q_i^{\pm} g_a^{\mp} \to R^{(1)} \to All) = \alpha_s(\frac{1}{16}\mathbf{P_{15}}^{ai} + \frac{1}{16}\mathbf{P_{\bar{6}}}^{ai} + \frac{1}{48}\mathbf{P_3}^{ai}) \tag{1.47}$$

$$\frac{1}{m_s}\Gamma(g_a^{\pm} g_b^{\mp} \to R^{(1)} \to All) = \alpha_s(\frac{19}{60}\mathbf{P_{8_S}}^{ab} + \frac{41}{60}\mathbf{P_1}^{ab}) \tag{1.48}$$

$$\frac{1}{m_s}\Gamma(q_i^{\pm}\bar{q}_j^{\mp} \to R^{(n)} \to All) \quad = \quad \alpha_s(\frac{79}{360}\mathbf{P_8}^{i\bar{j}} + \frac{49}{180}\mathbf{P_1}^{i\bar{j}}) \tag{1.49}$$

This optical theorem includes the effects of quantum interference between Regge excitations of different spin. The widths and cross section from the procedure of using optical theorem be more accurate than estimates in [13], [14] which ignore interference by using an incoherent sum over Regge excitations. For reference, for $\alpha_s 2TeV \simeq 0.082$, the width of the first Regge resonances in the dominant $qg \to R^{(1)} \to qg$ channel is at most 0.5 percent. So a narrow width approximation is good for Regge resonances. At a string resonance mass of 2.1 TeV the decays and branching fractions are $qg(91\%)$, $gg(5.5\%)$ and $g\bar{q}(3.5\%)$.

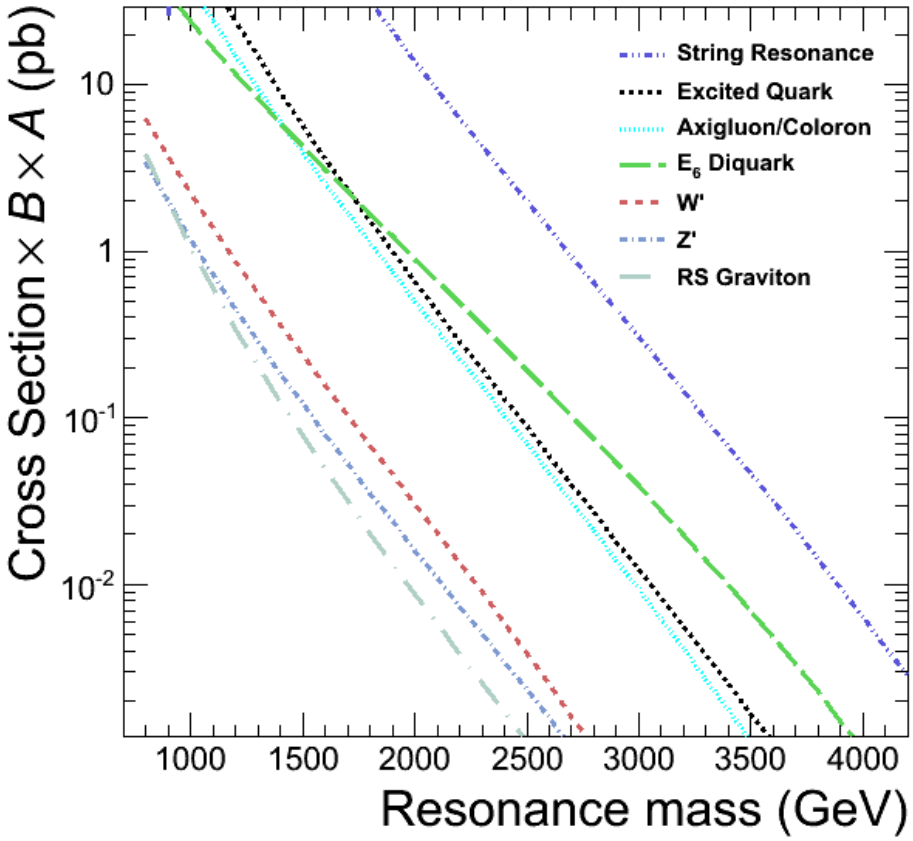

Figure 1.4: The cross section × branching ratio × kinematic acceptance for dijet resonance with $|\eta| < 2.5$ and $|\Delta\eta| < 1.3$ as a function of resonance mass for the following models: String Resonance, Excited quark, Axigluon and Coloron, W', Z', and Randal-Sundrum Graviton

Table 1.3: Cross section for dijet resonances in pp collisions at $\sqrt{s} = 7$ TeV with the eta cuts $|\Delta\eta| < 1.3$ and $|\eta| < 2.5$ on the two jets. The models are String Resonances (S) as described in this note, Excited Quark (q*), Axigluon or Coloron (A or C), E_6 diquark (D), Z', W' and Randall-Sundrum Graviton (G), for which the lowest order calculation was described in Sec. 1.2 .

Mass (GeV)	S (pb)	q^* (pb)	A or C (pb)	D (pb)	Z' (pb)	W' (pb)	G (pb)
500.0	0.4700E+05	0.2294E+04	0.9568E+03	0.2623E+03	0.2555E+02	0.4380E+02	0.4828E+02
600.0	0.1974E+05	0.9871E+03	0.4395E+03	0.1451E+03	0.1211E+02	0.2125E+02	0.1862E+02
700.0	0.9304E+04	0.4657E+03	0.2215E+03	0.8646E+02	0.6246E+01	0.1120E+02	0.8100E+01
800.0	0.4627E+04	0.2355E+03	0.1193E+03	0.5435E+02	0.3427E+01	0.6263E+01	0.3852E+01
900.0	0.2485E+04	0.1257E+03	0.6750E+02	0.3554E+02	0.1969E+01	0.3661E+01	0.1961E+01
1000.0	0.1392E+04	0.7005E+02	0.3967E+02	0.2393E+02	0.1172E+01	0.2212E+01	0.1053E+01
1100.0	0.7879E+03	0.4039E+02	0.2400E+02	0.1648E+02	0.7171E+00	0.1372E+01	0.5905E+00
1200.0	0.4731E+03	0.2394E+02	0.1486E+02	0.1154E+02	0.4486E+00	0.8673E+00	0.3426E+00
1300.0	0.2901E+03	0.1452E+02	0.9370E+01	0.8194E+01	0.2857E+00	0.5568E+00	0.2044E+00
1400.0	0.1776E+03	0.8982E+01	0.5998E+01	0.5877E+01	0.1845E+00	0.3616E+00	0.1248E+00
1500.0	0.1119E+03	0.5645E+01	0.3887E+01	0.4249E+01	0.1206E+00	0.2369E+00	0.7770E-01
1600.0	0.7212E+02	0.3596E+01	0.2544E+01	0.3090E+01	0.7961E-01	0.1562E+00	0.4911E-01
1700.0	0.4707E+02	0.2317E+01	0.1678E+01	0.2258E+01	0.5295E-01	0.1034E+00	0.3145E-01
1800.0	0.3106E+02	0.1507E+01	0.1115E+01	0.1656E+01	0.3545E-01	0.6872E-01	0.2036E-01
1900.0	0.2060E+02	0.9889E+00	0.7442E+00	0.1217E+01	0.2386E-01	0.4572E-01	0.1330E-01
2000.0	0.1382E+02	0.6531E+00	0.4988E+00	0.8953E+00	0.1611E-01	0.3043E-01	0.8743E-02
2100.0	0.9117E+01	0.4338E+00	0.3354E+00	0.6591E+00	0.1092E-01	0.2023E-01	0.5781E-02
2200.0	0.6244E+01	0.2896E+00	0.2260E+00	0.4852E+00	0.7413E-02	0.1342E-01	0.3840E-02
2300.0	0.4238E+01	0.1940E+00	0.1525E+00	0.3569E+00	0.5039E-02	0.8884E-02	0.2559E-02
2400.0	0.2881E+01	0.1304E+00	0.1030E+00	0.2622E+00	0.3426E-02	0.5859E-02	0.1708E-02
2500.0	0.1973E+01	0.8782E-01	0.6949E-01	0.1922E+00	0.2329E-02	0.3847E-02	0.1142E-02
2600.0	0.1367E+01	0.5925E-01	0.4684E-01	0.1406E+00	0.1580E-02	0.2513E-02	0.7635E-03
2700.0	0.9342E+00	0.4002E-01	0.3152E-01	0.1025E+00	0.1070E-02	0.1632E-02	0.5101E-03
2800.0	0.6449E+00	0.2704E-01	0.2116E-01	0.7449E-01	0.7231E-03	0.1053E-02	0.3402E-03
2900.0	0.4450E+00	0.1828E-01	0.1415E-01	0.5392E-01	0.4867E-03	0.6744E-03	0.2264E-03
3000.0	0.3040E+00	0.1234E-01	0.9428E-02	0.3885E-01	0.3261E-03	0.4287E-03	0.1501E-03
3100.0	0.2120E+00	0.8329E-02	0.6250E-02	0.2786E-01	0.2174E-03	0.2702E-03	0.9913E-04
3200.0	0.1439E+00	0.5613E-02	0.4119E-02	0.1987E-01	0.1440E-03	0.1688E-03	0.6512E-04
3300.0	0.9920E-01	0.3776E-02	0.2698E-02	0.1408E-01	0.9477E-04	0.1044E-03	0.4253E-04
3400.0	0.6700E-01	0.2535E-02	0.1754E-02	0.9920E-02	0.6190E-04	0.6403E-04	0.2759E-04
3500.0	0.4624E-01	0.1698E-02	0.1131E-02	0.6938E-02	0.4007E-04	0.3886E-04	0.1775E-04
3600.0	0.3136E-01	0.1135E-02	0.7222E-03	0.4815E-02	0.2570E-04	0.2335E-04	0.1133E-04
3700.0	0.2140E-01	0.7559E-03	0.4568E-03	0.3315E-02	0.1631E-04	0.1390E-04	0.7157E-05
3800.0	0.1415E-01	0.5021E-03	0.2858E-03	0.2261E-02	0.1024E-04	0.8199E-05	0.4475E-05
3900.0	0.9559E-02	0.3325E-03	0.1767E-03	0.1528E-02	0.6349E-05	0.4796E-05	0.2766E-05
4000.0	0.6426E-02	0.2195E-03	0.1079E-03	0.1022E-02	0.3889E-05	0.2787E-05	0.1689E-05
4100.0	0.4227E-02						
4200.0	0.2831E-02						
4300.0	0.1831E-02						
4400.0	0.1201E-02						
4500.0	0.7819E-03						
4600.0	0.4979E-03						
4700.0	0.3197E-03						
4800.0	0.2016E-03						
4900.0	0.1269E-03						
5000.0	0.8018E-04						

Chapter 2

The LHC and CMS Detector

2.1 The Large Hadron Collider (LHC)

The LHC is the world's largest and most powerful circular proton-proton (p-p) and lead ion (Pb-Pb) Collider, and it is at the CERN. The LHC is built 50 to 175 m underground and 26.7 km in circumference. The LHC is built to solve many questions among particle physics such as: What happened right after Big Bang? What gives matter mass? Why is there matter-antimatter asymmetry. The LHC started in 2009 with center of mass energy of 900 GeV, and the 7 TeV collision started in March 2010. There are four experiments at the LHC. CMS and ATLAS are built for multi purpose, and their main task of them is probing new physics at TeV scale and understanding already known physics. The LHCb is an experiment which is specialized in bottom quark physics. The last is ALICE. ALICE is optimized to study heavy ion collisions. Fig. 2.1 shows the layout of the LHC.

The beams are accelerated with several steps. The beams of protons start accelerating to an energy of 50 MeV by LINAC. Then the beams are transferred to the BOOSTER synchrotron and accelerated up to 1.4 Gev and up to 25 GeV in PS. After PS, SPS accelerates the beams up to 450 GeV and finally proton beams are injected into the LHC and accelerated to the energy of 3.5 TeV. In Table 2.1 the parameters of beam are presented. I present designed values in the table, and this is not the operating value the data which this analysis used. The LHC is raising it's performance slowly because the LHC is operating the machines at a level which never achived before.

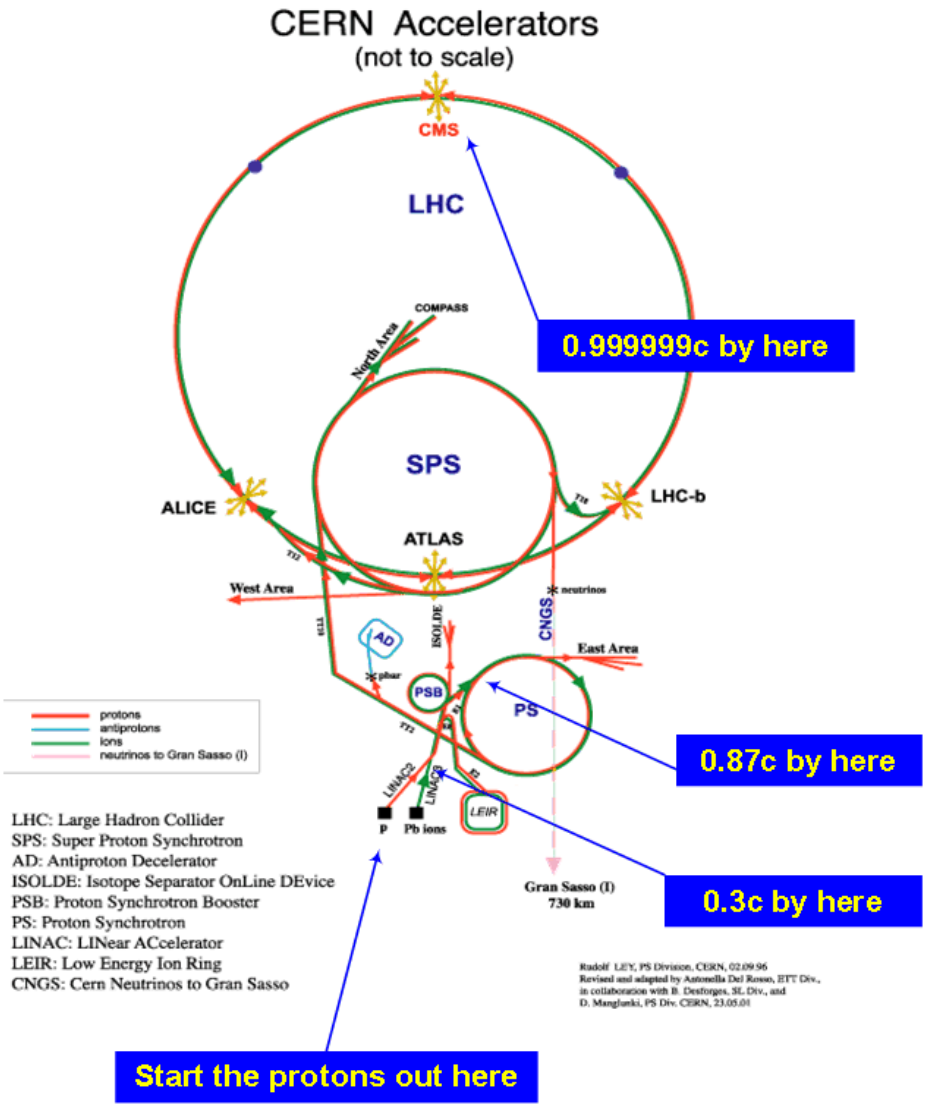

Figure 2.1: A schematic view of the LHC. [16]

The production rate per second for a physics process can be calculated by

$$R = \sigma L \tag{2.1}$$

where σ is the cross section of the physics process and L is the luminosity of the collider.

Table 2.1: The LHC beam parameters relevant for peak luminosity. Mostly designed values except energy per proton beam and energy loss per turn [17]

Beam parameter	vales
Energy per proton beam	3.5 TeV
Number of particles per bunch	1.15×10^{11}
Number of bunches	2808
Bunch spacing	25 ns
RMS bunch length	7.55 cm
Bunch crossing rate	40 MHz
Peak luminosity	1.0×10^{34} cm^{-2}sec^{-1}
Peak luminosity per bunch crossing	3.56×10^{30} cm^{-2}sec^{-1}
Luminosity lifetime	14.9 hours
Energy loss per turn	420 GeV

The accelerator luminosity is

$$L = \frac{f n_1 n_2}{2\pi\sqrt{\sigma_{x,1}^2 + \sigma_{x,2}^2}\sqrt{\sigma_{y,1}^2 + \sigma_{y,2}^2}} \tag{2.2}$$

where, f is the collision frequency, n_i is the number of protons in the bunch of beam i, and $\sigma_{x/y,i}$ is the transverse spread beam i in x and y direction.The total amount of data taken in a time period corresponds to an integrated luminosity , $\mathscr{L}$, which is defined by

$$\mathscr{L} = \int L dt \tag{2.3}$$

2.2 Compact Muon Solenoid

CMS is a multi purpose detector at the LHC. It has a diameter of 14.6 m, a length of 21.6 m, and a mass of 12.5 k tonnes. CMS is still smaller and lighter than ATLAS. That is why they call it "Compact" As the name of the detector shows, it has an excellent muon system. The following is the summary of the detector requirement to meet the goal of the LHC physics described at [18]

- Good muon identification and momentum resolution over wide range of momenta

and angles, good dimuon mass resolution ($\approx 1\%$ at 100 GeV), and ability to determine unambiguously the charge of muons with $p < 1$ TeV;

- Good charged particle momentum resolution and reconstruction efficiency in the inner tracker. Efficient triggering and offline tagging of τs and b quarks, requiring pixel detectors close to the interaction region;

- Good electromagnetic energy resolution, good diphton and dielectron mass resolution ($\approx 1\%$ at 100 GeV), wide geometric coverage, π^0 rejection, and efficient photon and lepton isolation at high luminosities;

- Good missing transverse energy and dijet mass resolution, requiring hadron calorimeters with a large hermetic geometric coverage and with fine lateral segmentation.

Fig. 2.2 shows the perspective view of the CMS detector

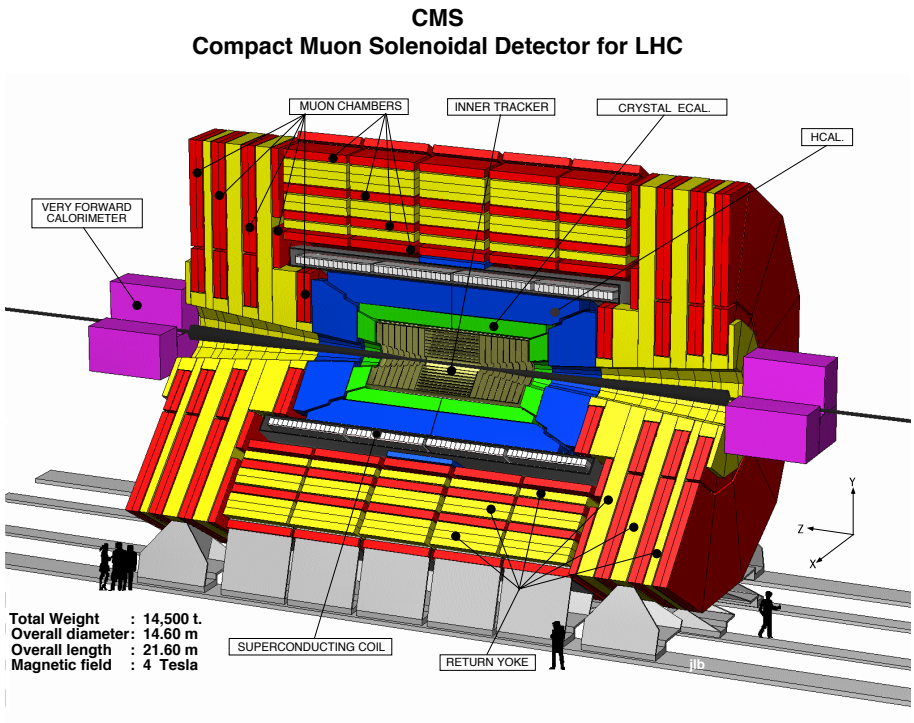

Figure 2.2: A schematic view of the CMS. [19]

2.2.1 The Tracker

The CMS tracking system is designed to reconstruct high energy muons, electrons, and charged hadrons with high momentum resolution and efficiency and to measure secondary vertices. It has a diameter of 2.5 m and a length of 5.8 m. Over the tracker, 4 T magnetic field is provided homogeneously by the CMS solenoid. The tracker consists of two parts. One is the silicon pixel detector and the other is the silicon strip detector. The silicon pixel detector with 3 barrel layers is located at the radius between 4.4 cm and 10.2 cm, at the core of the detector to deal with highest intensity of particles. The silicon strip detector with 10 barrel detection layer up to 11 m surrounds the silicon pixel detector. The pixel system contains 65 million pixels. The strip detector is composed of 15,148 detector modules distributed among the four different subsystems(TIB, TID, TOB, TEC). Both detectors cover up to 2.5 in pseudorapidity (η). For high momentum track (100 GeV) the transverse momentum resolution is around 1-2 % up to $|\eta| \approx 1.6$, beyond which it degrades due to the reduced lever arm. [18] More information can be found from [18], [20]. Fig. 2.3 shows the perspective view of the tracking system.

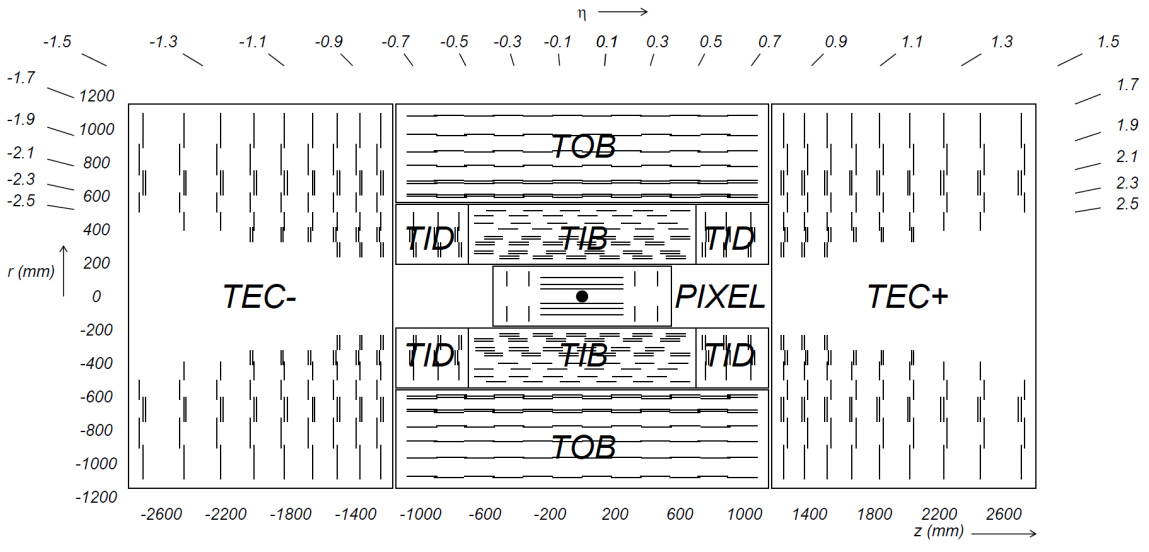

Figure 2.3: A schematic view of the track system. Each line represents a detector module. Double lines indicate back-to-back modules. [18]

2.2.2 The Calorimeters

A calorimeter is a detector measuring the energy of particles. Most particles interact with a material and deposit their energy. The CMS calorimeter measure energy of photons, electrons and hadrons (jets). There are two types of calorimeter in CMS. The one is ECAL which measure the energy of particles interacting electromagnetically (photons and electrons). The other is HCAL which measures the energy of strongly interacting particles, hadrons (e.g. $\pi^{\pm}, \pi^{0}$, K etc.). Fig. 2.4 shows the schmatic view of one quadrant of the calorimetry and tracking system.

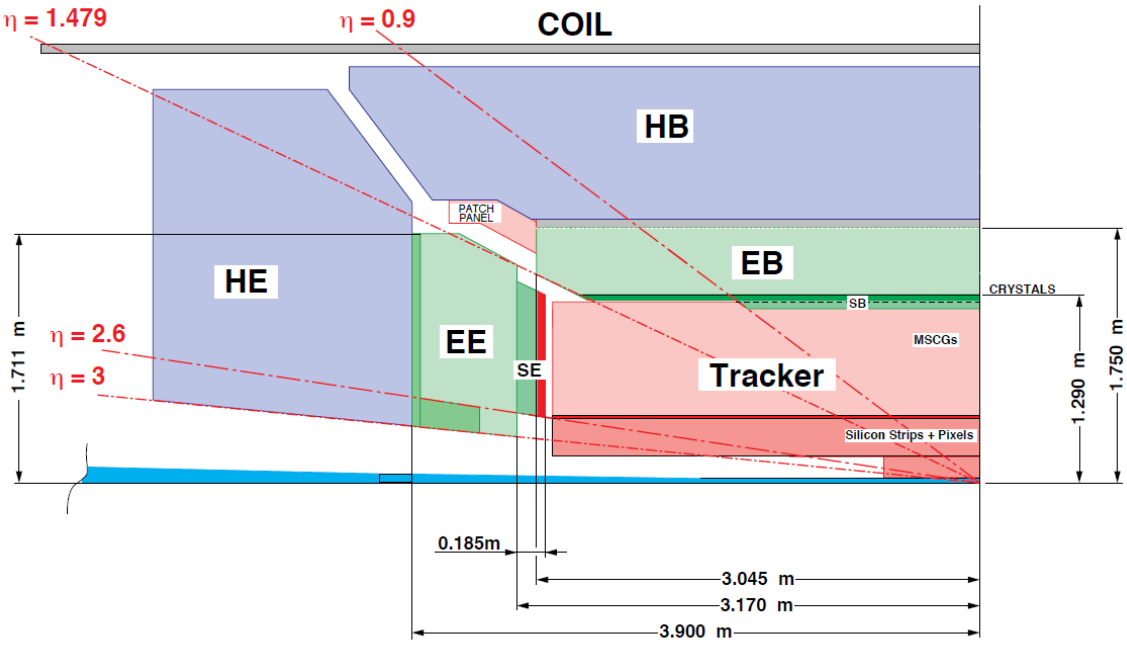

Figure 2.4: A schematic view of CMS.

2.2.2.1 The Electromagnetic Calorimeter (ECAL)

The ECAL of CMS is a hermetic homogeneous calorimeter made of 61200 lead tungstate ($PbWO_4$) crystals in the barrel part ($|\eta| < 1.48$,EB) and 7324 crystals in each of the two endcaps ($1.5 < |\eta| < 3.0$, EE). $PbWO_4$ crystals have high density($8.28 g/cm^3$), short radi-

ation length($X_0 = 0.89cm$), and small Moliere raius ($2.2cm$) which allow fine granularity and compact calorimeter. In front of EE, there is ES ($1.6 < |\eta| < 2.6$). ES is designed to reject the π^0s which decay into two closely separated photons since there is Higgs boson which decay into two photons. [18]. Fig. 2.5 shows layout of the ECAL.

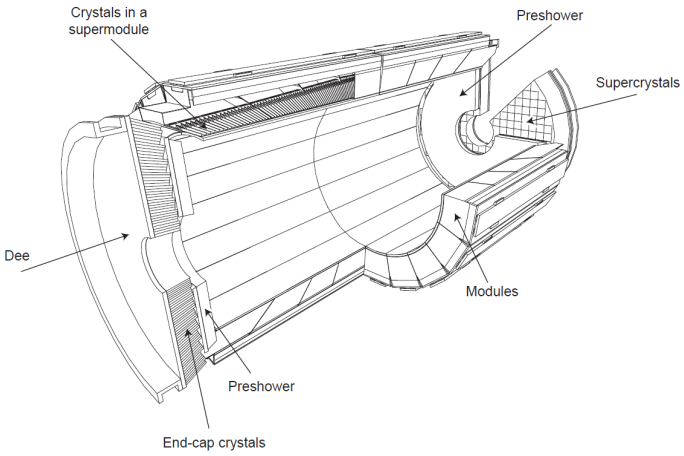

Figure 2.5: Layout of the ECAL showing the arrangement of crystal modules, super modules and endcaps, with preshower in front. [18]

For the energy below 500 GeV where shower leakage from the rear of the calorimeter start to become significant, The energy resolution is

$$(\frac{\sigma}{E})^2 = (\frac{S}{\sqrt{E}})^2 + (\frac{N}{E}) + C^2 \tag{2.4}$$

where S is the stochastic term which is connected to photo-statistics, N is the noise term which is from noise of the electrons and C is the constant term which is about calibration and non-uniformity and dominates at high energy. [21] Fig. 2.6 shows the ECAL energy resolution measured from a beam test. The energy was measured in an array of 3×3 crystals with an electron impacting the central crystal. In Fig. 2.6, points correspond to events taken restricting the incident beam to a narrow ($4 \times 4\ mm^2$) region.

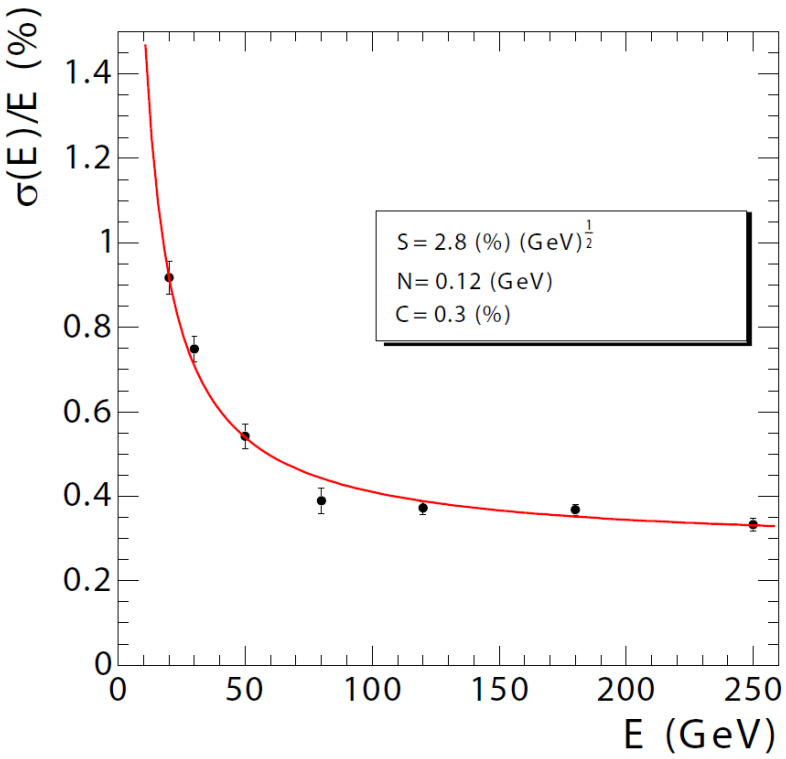

Figure 2.6: ECAL energy resolution, σ/E, as a function of electron energy as measured from a beam test. [18]

2.2.2.2 The Hadron Calorimeter (HCAL)

The HCAL [22] measures hadronic particles produced in CMS. It needs enough spatial and energy resolution. The HCAL consists of four subdetectors: HB, HE, HO, and HF. The HB is placed just inside the magnet ($|\eta| < 1.3$). The HE is positioned behind EE ($1.3 < |\eta| < 3.0$). The HF is located close to beam pipe outside the muon system ($3.0 < |\eta| < 5.0$). The HO is placed between the magnet and the muon detector to ensure that energy from hadronic showers does not leak ($|\eta| < 1.3$). The combined depth of the ECAL and HCAL is at least eleven interaction lengths. The HB, HE and HO are constructed of alternating layers of brass absorbers (5 8 cm) and plastic scintillators (3.7 mm think). Since the HF must deal with an extreme radiation environment, the HF is made by the steel as absorber and quartz fibers as active medium for this reason. Fig. 2.7 shows the schematic view of hcal.

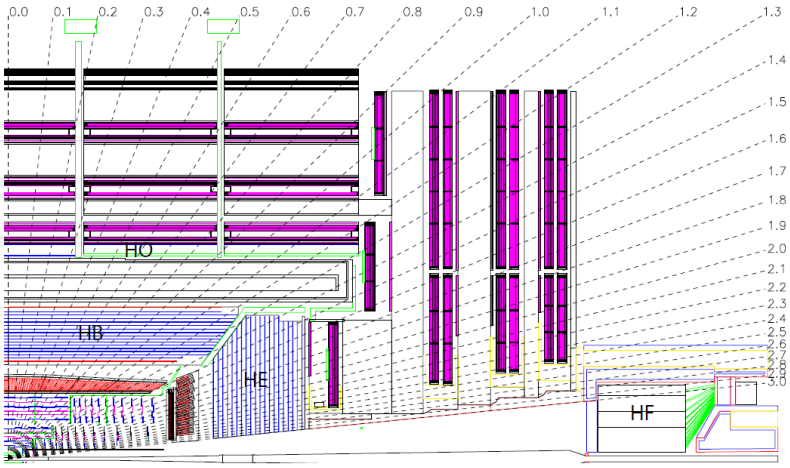

Figure 2.7: Schmatic view of HCAL showing HB, HE, HF, and HO. [18]

2.2.3 The Muon System

Muons are produced from many interesting particles including Higgs boson. Muons can be produced from $H \rightarrow ZZ$ or $ZZ' \rightarrow llll$ process. Since Muons are relatively easy to detect since they are highly penetrating which makes them almost background free. The main consideration of the CMS muon system is to have the capability of reconstructing the momentum and charge of muons over the entire kinematic range of the LHC. [23] The CMS muon system consists of three detector. They are DT in the barrel region ($|\eta| < 1.2$), CSC in the endcap region ($0.9 < |\eta| < 2.4$), and RPC in both barrel and endcap regions ($|\eta| < 1.6$). Fig. 2.8 shows the CMS muon system. The DT and CSC provide accurate and precise position measurement and RPC provides precise time measurement.

The muon system covers from 10° to 170° in θ. The efficiency of offline reconstruction of single-muon is between 95% and 99%. The resolution of the offline muon momentum is about 9% for small $|\eta|$ and transverse momentum up to 200 GeV. The resolution of the offline muon momentum is between 15% and 40% at 1 TeV depending on $|\eta|$. A global muon is the muon which is improved by including inner tracker when reconstruct. The global muon has the momentum resolution about 5%. More information can be found

at [23].

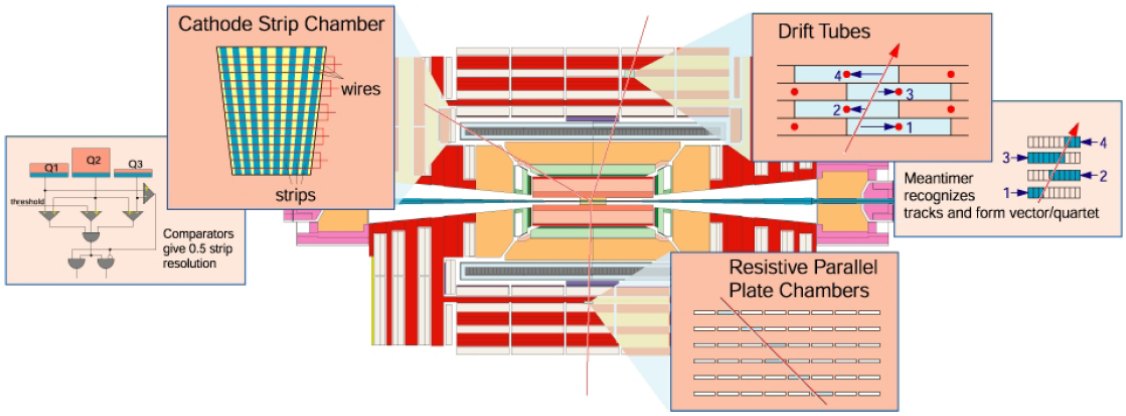

Figure 2.8: The CMS muon system.

2.2.4 The Magnet

High magnetic field is needed to measure momentum of highly energetic charged particles by bending them. The goal of the design of the magnet is to achieve reconstruction of 1 TeV muons with a 15% p_T resolution. The transverse momentum of a charged particle and magnetic field have following relation

$$p_T = 0.3BR \tag{2.5}$$

where p_T is the momentum of a charged particle; B is the magnetic field; and R is a radius of the curvature of the charged particle. The superconducting solenoid is designed to produce 4 tesla and now it produce 3.8 tesla uniform magnetic field over the inner tracking and calorimeter region. The field will be achieved by a 20 kA current. The superconducting solenoid has a inner diameter of 6 m, and a length of 13 m at the magnet core. The diameter is extended to 14 m with the return yoke. [24] Fig. 2.9 shows the CMS superconducting magnet.

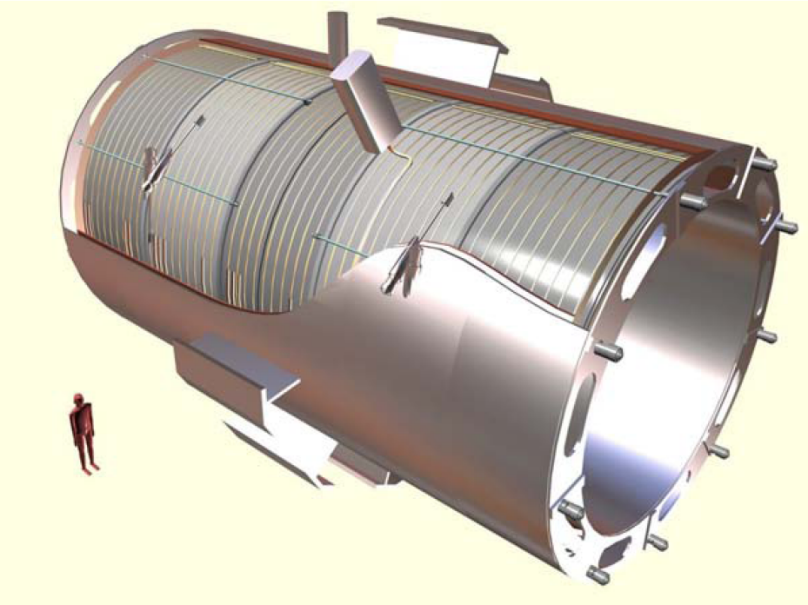

Figure 2.9: The CMS superconducting magnet.

2.2.5 The Trigger

At the LHC, the crossing frequency of the proton beam will reach 40 MHz according to initial design. Since we have limitation of cpu and storage, we need to select only interesting physics events among those rate of collision. This is the main goal of the trigger system. The CMS trigger consists of two main stages in order to achieve high efficiency. They are the L1T and the HLT. The L1T is designed to reduce the incoming average data rate from 40 MHz to a maximum of 100 kHz. The L1T uses information from the calorimeters and the muon system. The HLT reduces the rate of stored events to 100 Hz. Events passing the HLT are stored and made available for offline analyses. More detailed information can be found from [25] [26].

Chapter 3

Measurement of Dijet Mass Spectrum

In this section, how the dijet mass is measured is described.

3.1 Experiment Technique

In the section, the outline of this experiment is described. First we find dijet mass distributions for the inclusive process $pp \rightarrow jet + jet + anything$. Since this is general search we restrict the process to only dijet. The main background of this experiment is the QCD scattering which fall smoothly and steeply. The evidences of new particles which indicate new physics are going to be represented as bumps on the background dijet mass distributions. If there is no new particle, we compare 95 CL upper cross section limit to the cross section value from theory. Then we set excluded mass range for specific dijet resonance models.

3.2 Data

The data are stored officially in CMS. Each collision, called event, is recoded in files. These files are stored at official area with specific names. The data are named to make users easily figure out what each data is for. In this analysis, HT data is used. This data has events which passes "HT" triggers. Trigger will be discussed in later section. There are different types of data. In big picture, we distinguish them as "RAW" and "RECO". The "RAW" data has detector information and the "RECO" data includes reconstructed physics objects by using various reconstruction algorithm. This analysis uses "AOD" data which is subset of

"RECO" data which contains only necessary information for users.

Below shows the data names used in this analysis. Those data are stored in the CMS official store area. The number in front of the dataset name shows run range in the data.

(136033-141949, 4.2.1 patch1) /JetMETTau/Run2010A-Apr21ReReco-v1/AOD
(141950-145761, 4.2.1 patch1) /JetMET/Run2010A-Apr21ReReco-v1/AOD
(145762-147145, 4.2.1 patch1) /Jet/Run2010B-Apr21ReReco-v1/AOD
(147146-149442, 4.2.1 patch1) /MultiJet/Run2010B-Apr21ReReco-v1/AOD
(160404-163869, 4.2.3) /HT/Run2011A-May10ReReco-v1/AOD
(163870-167784, 4.2.3 patch1, patch2, patch3 and patch5) /HT/Run2011A-PromptReco-v4/AOD

Since the detector is not operating in good condition all time. They make good run and luminosity section(LS) list. This list is called JSON.

(136033-149442) https://cms-service-dqm.web.cern.ch/cms-service-dqm/CAF/certification/Collisions10/7TeV/Reprocessing/Cert_136033-149442_7TeV_Apr21ReReco_Collisions10_JSON.txt
(160404-163869) https://cms-service-dqm.web.cern.ch/cms-service-dqm/CAF/certification/Collisions11/7TeV/Reprocessing/Cert_160404-163869_7TeV_May10ReReco_Collisions11_JSON.txt
(163870-167784) https://cms-service-dqm.web.cern.ch/cms-service-dqm/CAF/certification/Collisions11/7TeV/Prompt/Cert_160404-167784_7TeV_PromptReco_Collisions11_JSON.txt

By using the official luminosity calculation, the luminosity from above dataset and JSON file for Wide Jets is estimated to be 1.01/fb with a systematic uncertainty of 6%. The calculation method is explained in "https://twiki.cern.ch/twiki/bin/ viewauth/CMS/LumiCalc".

We required that good primary vertex of the each event is located within 24 cm in z direction from center of the CMS detector and a number of degree of the freedom is less than 4. Also we keep jets with corrected p_T greater than 30 GeV.

3.3 MC Samples

In this experiments, we reviewed the simulation which is used to compare to data.

3.3.1 QCD

The QCD scattering is simulated as background. For this purpose, the QCD PYTHIA (version 6.425) MC is used. Since the cross section of simulation is decreased as the momentum of hard scattered parton in the simulation is increased, these simulations are prepared for 20 different transverse momenta (p_T) range of hard scattered partons. The following simulations are made by QCD Pythia MC.

/QCD_Pt-XXtoYY_TuneZ2_7TeV_pythia6/Summer11-PU_S3_START42_V11-v2/ AODSIM
/QCD_Pt-XX_TuneZ2_7TeV_pythia6/Summer11-PU_S3_START42_V11-v2/ AODSIM

where the XX and YY represent p_T hat boundaries. Since each simulation has different cross section and number of events, they are weighted before compare to data.

3.3.2 Resonances

For resonance shapes we use the PYTHIA (version 6.425) MC for excited quarks (Qstar) and Randall Sundrum Gravitons (RSGraviton) as discussed in next section. The following simulation is used in this analysis:

/RESONANCEToJJ_M-XX_TuneD6T_7TeV_pythia6/
Summer11-PU_S4_START42_V11-v1/AODSIM

where RESONANCE represent "Qstar" or "RSGraviton", XX is 700, 1200, 2000 and 3500 for those masses in GeV.

3.4 Jet Reconstruction

How jets are reconstructed is discussed in this section. The anti-k_T algorithm is used to reconstruct jets with radius of jets, $R = \sqrt{(\Delta\eta)^2 + (\Delta\phi)^2} = 0.5$ and 0.7 officially. Calorimeter jets and PF jets use 0.7 and wide jets use 0.5 as a radius of jets. Calorimeter jets and PF jets use a radius of jet of 0.7 so jets can collect energies with large area. Since this analysis focuses on dijet search, the big radius of jet is useful. Increasing a size of jet allows collecting more energies but also more noise. However, the energies from noise which are collected by jets with a radius of jet of 0.7 are much smaller than the energy from partons because this analysis uses very high energetic jets. Of course there are jets with a noise which has high energy, but the methods to distinguish and remove noise are already studied and explained in data quality section.

As already mentioned, there are three different types of jets we are using: calorimeter jet, PF jet, and wide jet. For the final result, wide jets are used. Calorimeter and PF jets are used for cross check. Calorimeter jets use energies which are deposited in calorimeter as inputs when reconstruct jets. PF jets use stable particles which are reconstructed by combining information from all available sub-detectors. PF categorizes all particles into the five types: muons, electrons, photons, charged and neutral hadrons. The reconstructed jet has also kinematic variables such as energy, E, momentum $\vec{p}$ and transverse momentum, p_T. E is defined as the scalar sum of the energies of the inputs, $\vec{p}$ is the corresponding vector sum of the momentum of the inputs and p_T is the component of $\vec{p}$ in the transverse plane.

3.4.1 Jet Correction

The jet correction is modification of energies of jets. Since the response of the particle is not linear nor uniform, CMS provides jet correction which is used as a tool to make reasonable recovery to original energy. This correction is made with two steps. The correction is measured using MC simulation, then calibrated with real data (Residual correction). When jet correction is measured using MC simulation, generated jet is used. Generated jet is the jet which is reconstructed from stable generated particles before detector simulation. The corrections are decided so the p_T of corrected jet has equal p_T of generated jet. A residual data-driven relative (L2) correction derived from dijet balance, using the same sample, is applied to the data to correct for differences between data and MC: the method and correction is described for a smaller sample. [27, 28]

CMS has 7 steps of correction but dijet search used first three steps. They are "L1 Pile up Correction", "L2 Relative Jet Correction" and "L3 Absolute Jet Correction".

3.4.2 Wide Jet

This analysis uses wide jets since wide jets can collect the final state radiations while wide jets reject noises effectively. We combine PF jets with $p_T > 10$ GeV within $\Delta R < 1.1$ to obtain wide jets as shown in Fig.3.1. The $p_T > 10$ is introduced to reject noise, and the $\Delta R < 1.1$ is best choice for a single search for quark-quark, quark-gluon, gluon-gluon resonances. The detail study of wide jet algorithm is described in elsewhere [29]. This analysis uses wide jets for the search and PF jets and calo jets as a check, and all figures show wide jets unless otherwise noted.

3.4.3 Pseudorapidity Cut

Our main background is QCD t-channel scattering which has similar θ^* distribution as Rutherford scattering has at small angle. θ^* is the center of mass scattering angle as shown

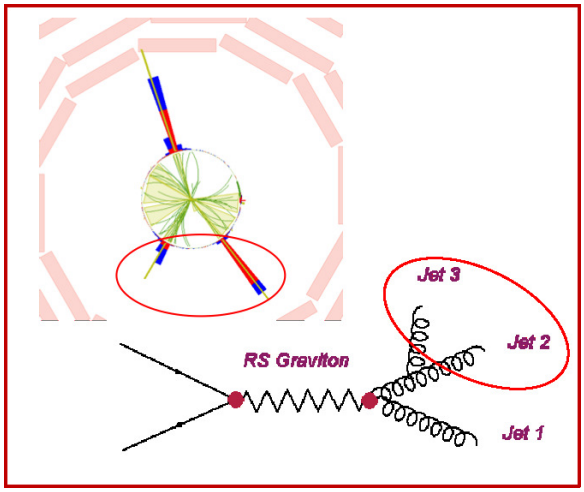

Figure 3.1: Wide jets are made by combining PF jets

in Fig. 3.2. For QCD t-channel scattering, $cos\theta^*$ has a value near 1, that is $|\Delta\eta|$ should have reasonably big number as the left plot of Fig. 3.3 shows while the resonance (Excited quark) have different (η_1, η_2) distribution, where η_1 is pseudorapidity of highest p_T jet and η_2 is pseudorapidity of highest p_T jet .

$$\frac{d\hat{\sigma}}{dcos\theta*} = \frac{1}{(1-cos\theta^*)^2} \tag{3.1}$$

$$cos\theta^* = tanh(\eta^*) = tanh(\frac{\Delta\eta}{2}) \tag{3.2}$$

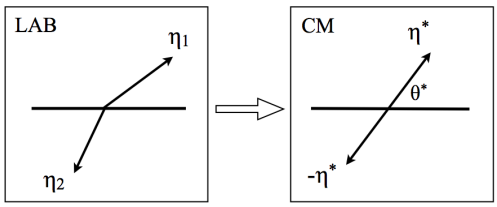

Figure 3.2: Two partons system in Lab (left) and CM frame (right)

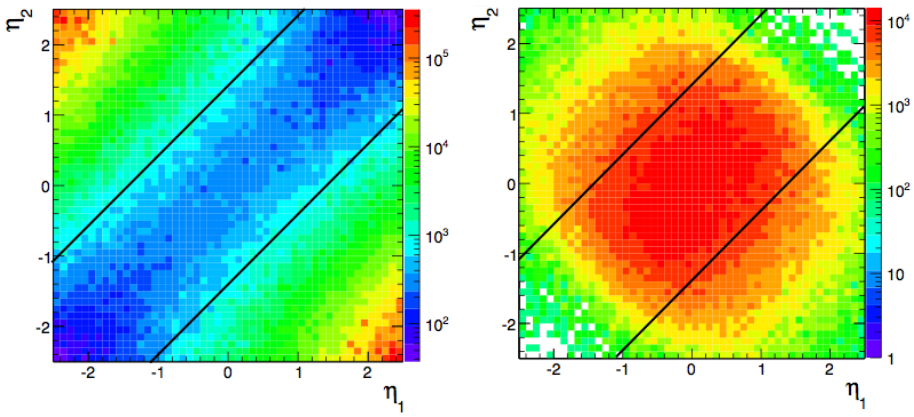

Figure 3.3: (η_1, η_2) distribution of two leading jets for PTYHIA QCD (left) and for excited quark at mass of 1.2 TeV (right). The region between two solid lines shows $|\Delta\eta| < 1.3$ kinematic cut.

Since the signal and the background have different $\eta_1 - \eta_2$ distribution, we studied significance for different η cut and $\Delta\eta$ cut by using $S/\sqrt{B}$, where S is signal and B is background as Fig.3.4 shows. The background defined as the LOQCD cross section for $0.9 \times M_{Res} < M_{jj} < 1.1 \times M_{Res}$. Fig.3.4 clearly shows the η cuts, $|\eta| < 2.5$ and $|\Delta\eta| < 1.3$, maximize the sensitivity for isotropic decays of dijet resonances, like excited quark, in the presence of QCD background. [31] ATLAS uses same cut. [30]

This selection serves several purposes:

- It suppresses QCD contribution significantly more than dijet resonances.
- It defines a fiducial region for our measurement predominantly in the Barrel.
- It provides a faster trigger turn-on curve for the jet trigger which uses E_T, allowing us to start the analysis at lower mass.

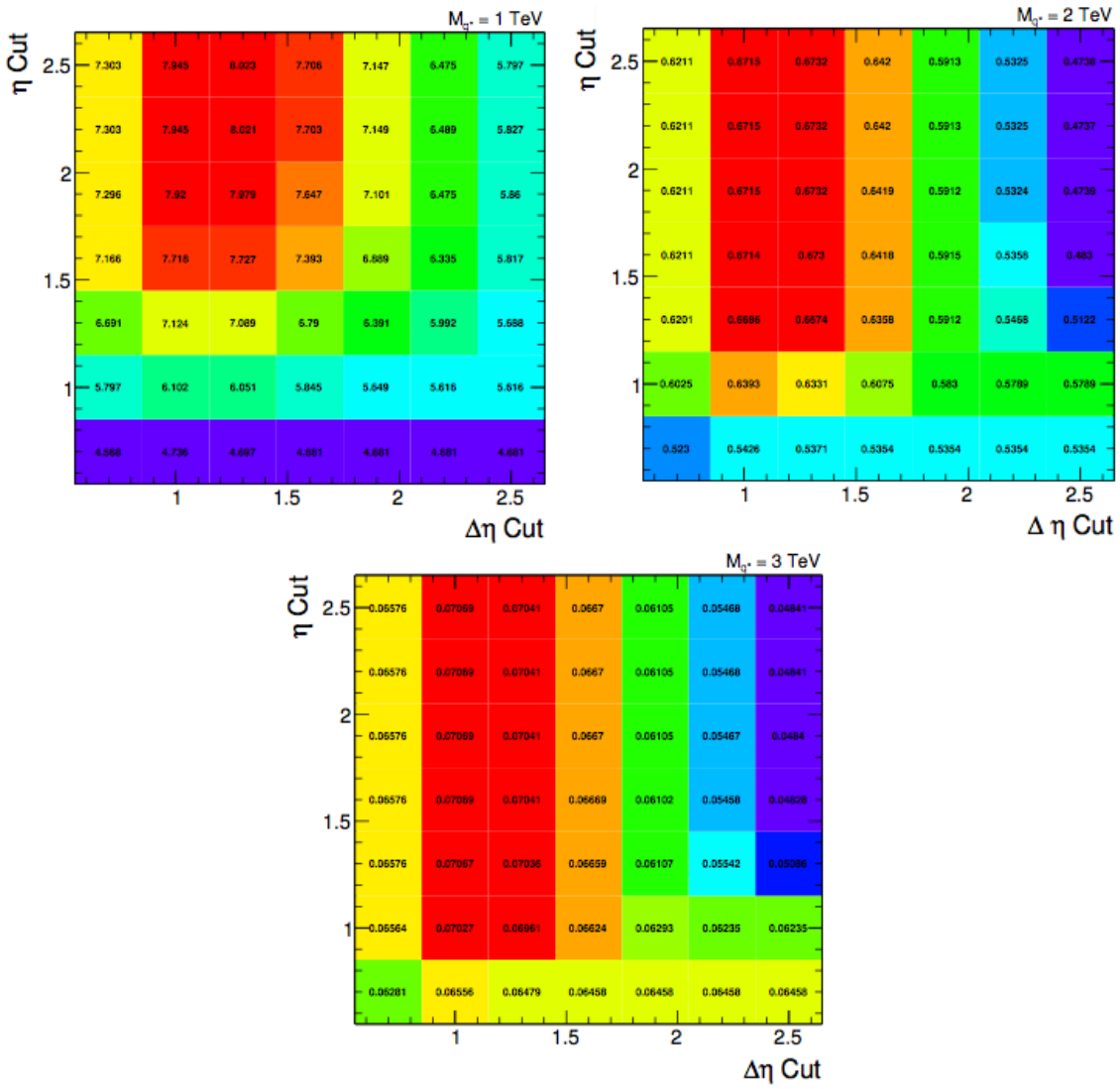

Figure 3.4: $Signal/\sqrt{Background}$ distribution of different η and $\Delta\eta$ cut for excited quark with mass of 1,2, and 3TeV

3.4.4 Data Quality

When we reconstruct jets, not all of them are physics object. Unphysical objects can be reconstructed as jets. Those are noise which needed to be rejected. Even though there is several algorithms implemented to reject those noise at detector level, some of them make jets. The "Jet ID" is introduced to reject those noise. Since two different type of jet

algorithms are used, there are two different type of "Jet ID". One is the "Calo Jet ID" and the other is "PF Jet ID".

We require that both leading Calo jets satisfy the “loose jet ID” criterion defined below:

- jet electromagnetic fraction (EMF) > 0.01 if jet $|\eta| < 2.6$
- number of rechits carrying 90% of the jet energy (n90hits) > 1
- fraction of energy contributed by the hottest HPD (fHPD) < 0.98

We used PF leading jets passing “tight jet ID” criterion defined below:

- Neutral Hadron Fraction < 0.90
- Neutral Electromagnetic Fraction < 0.90
- Number of Constituents > 1
- Charged Hadron Fraction > 0 if jet $|\eta| < 2.4$,
- Charged Electromagnetic Fraction < 0.99 if jet $|\eta| < 2.4$,
- Charged Hardron Multiplicity > 0 if jet $|\eta| < 2.4$,

These cuts are used to make a ROOT file containing histograms of dijet mass and other quantities (histograms_data_HT_1p010fbm1.root) which is saved, along with the processed root tree (ProcessedTree_Combined_HT.root) on cmslpc.fnal.gov at

`/pnfs/cms/WAX/11/store/user/lpcjj/DijetMass/2011Jul01_1p010fbm1/`

3.5 Dijet Mass Spectrum

The dijet system is composed of the two jets with the highest p_T (leading jets) in an event. The dijet mass is given by $m = \sqrt{(E_1 + E_2)^2 - (\vec{p}_1 + \vec{p}_2)^2}$.

3.5.1 Trigger

We select events that passed HLT paths listed in Table 3.1 and perform a jet p_T preselection of $p_T > 40$ GeV (corrected) for calo and PF jets. From the processed trees we perform the final analysis.

We use the unprescaled jet trigger for this analysis. The highest threshold used for the unprescaled trigger is 550GeV for HT trigger. We therefore find the fully efficient cut in dijet mass for the 550 GeV HT trigger and that is fully efficient for all lower threshold triggers as well. We begin our analysis at that fully efficient dijet mass value.

The trigger efficiency for the HLT path HLT_HT550_v4, HLT_HT550_v5, HLT_HT550_v6, HLT_HT550_v7 measured from a sample acquired with a prescaled trigger with a lower p_T threshold (HLT_HT500_v4, HLT_HT500_v5, HLT_HT500_v6, HLT_HT500_v7), was greater than 99.5% for dijet mass above 838 GeV for wide jets, 788 GeV for PF jets and 740 GeV for calo jets as shown in Fig. 3.5. We start the dijet mass spectrum from 838 GeV for wide jets, 788 GeV for PF jets, 740 GeV for calo jets which are the first low edges of the predefined mass bins above the 99.5% efficient point for wide, PF and calo jets, making the first dijet mass bin $838 < m < 890$ GeV, $788 < m < 838$ GeV, $740 < m < 788$ GeV. This dijet mass bin has a measured trigger efficiency of $99.91 \pm 0.01\%$ over the entire bin for wide jets, $99.87 \pm 0.01\%$ for PF jets and $99.98 \pm 0.01\%$ for calo jets.

The number of events vs. dijet mass are shown in Fig. 3.6. The trigger turn-over of the HLT_Jet550_v4, HLT_Jet550_v5, HLT_Jet550_v6, HLT_Jet550_v7 trigger can be seen in the mass spectrum along with the 99.5% efficiency point at a mass of 838 GeV for wide jets, 788GeV for PF jets and 740 GeV for calo jets.

For the MC events, no trigger requirements are applied because the dijet mass cut is shown to be 100% efficient in Fig. 3.5, but the rest of the event and jet selection criteria are identical.

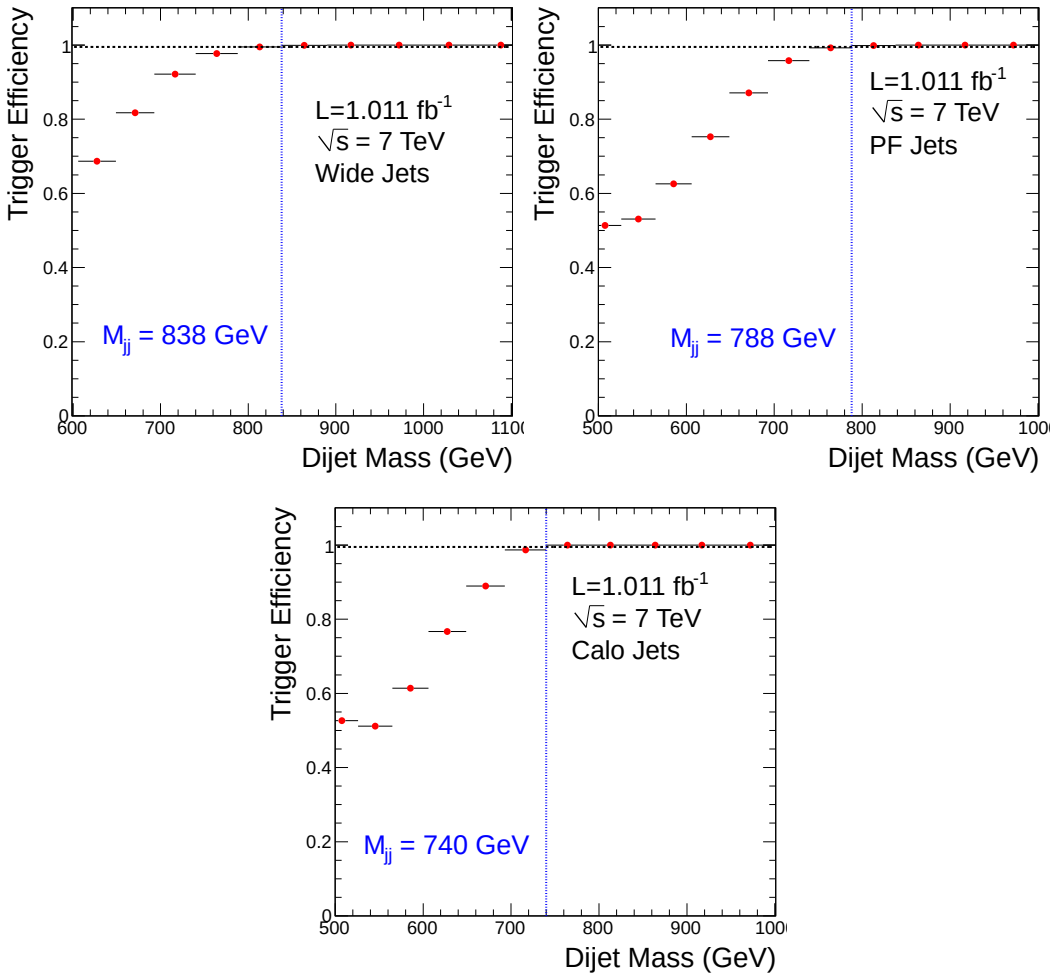

Figure 3.5: HLT_HT550 trigger efficiency as a function of dijet mass for $|\eta| < 2.5$ and $|\Delta\eta| < 1.3$ is measured from the data for wide jets (top left) and PF jets (top right) and efficiency of HT550 trigger for calo Jets (bottom).

Table 3.1: L1 and High Level HT Triggers

Trigger Path	L1 seeds	Trigger Path	L1 seeds
L1_HTT50	none	HLT_HT300_v2	L1_HTT100
L1_HTT75	none	HLT_HT300_v3	L1_HTT100
L1_HTT100	none	HLT_HT300_v4	L1_HTT100
HLT_HT100U	L1_HTT50	HLT_HT300_v5	L1_HTT100
HLT_HT100U_v3	L1_HTT50	HLT_HT300_v6	L1_HTT100
HLT_HT120U	L1_HTT50	HLT_HT300_v7	L1_HTT100
HLT_HT130U_v3	L1_HTT50	HLT_HT300_v8	L1_HTT100
HLT_HT140U	L1_HTT50	HLT_HT350_v2	L1_HTT100
HLT_HT150U_v3	L1_HTT50	HLT_HT350_v3	L1_HTT100
HLT_HT160U_v1	L1_HTT50	HLT_HT350_v4	L1_HTT100
HLT_HT160U_v3	L1_HTT50	HLT_HT350_v5	L1_HTT100
HLT_HT200U_v1	L1_HTT50	HLT_HT350_v6	L1_HTT100
HLT_HT200U_v3	L1_HTT50	HLT_HT350_v7	L1_HTT100
HLT_HT150_v2	L1_HTT50	HLT_HT360_v2	L1_HTT100
HLT_HT150_v3	L1_HTT50	HLT_HT400_v3	L1_HTT100
HLT_HT150_v4	L1_HTT50	HLT_HT400_v4	L1_HTT100
HLT_HT150_v5	L1_HTT50	HLT_HT400_v5	L1_HTT100
HLT_HT150_v6	L1_HTT50	HLT_HT400_v6	L1_HTT100
HLT_HT150_v7	L1_HTT50	HLT_HT400_v7	L1_HTT100
HLT_HT160_v2	L1_HTT50	HLT_HT450_v3	L1_HTT100
HLT_HT200_v2	L1_HTT75	HLT_HT450_v4	L1_HTT100
HLT_HT200_v3	L1_HTT75	HLT_HT450_v5	L1_HTT100
HLT_HT200_v4	L1_HTT75	HLT_HT450_v6	L1_HTT100
HLT_HT200_v5	L1_HTT75	HLT_HT450_v7	L1_HTT100
HLT_HT200_v6	L1_HTT75	HLT_HT500_v3	L1_HTT100
HLT_HT200_v7	L1_HTT75	HLT_HT500_v4	L1_HTT100
HLT_HT240_v2	L1_HTT100	HLT_HT500_v5	L1_HTT100
HLT_HT250_v2	L1_HTT100	HLT_HT500_v6	L1_HTT100
HLT_HT250_v3	L1_HTT100	HLT_HT500_v7	L1_HTT100
HLT_HT250_v4	L1_HTT100	HLT_HT550_v4	L1_HTT100
HLT_HT250_v5	L1_HTT100	HLT_HT550_v5	L1_HTT100
HLT_HT250_v6	L1_HTT100	HLT_HT550_v6	L1_HTT100
HLT_HT250_v7	L1_HTT100	HLT_HT550_v7	L1_HTT100
HLT_HT260_v2	L1_HTT100	HLT_HT2000_v1	L1_HTT100

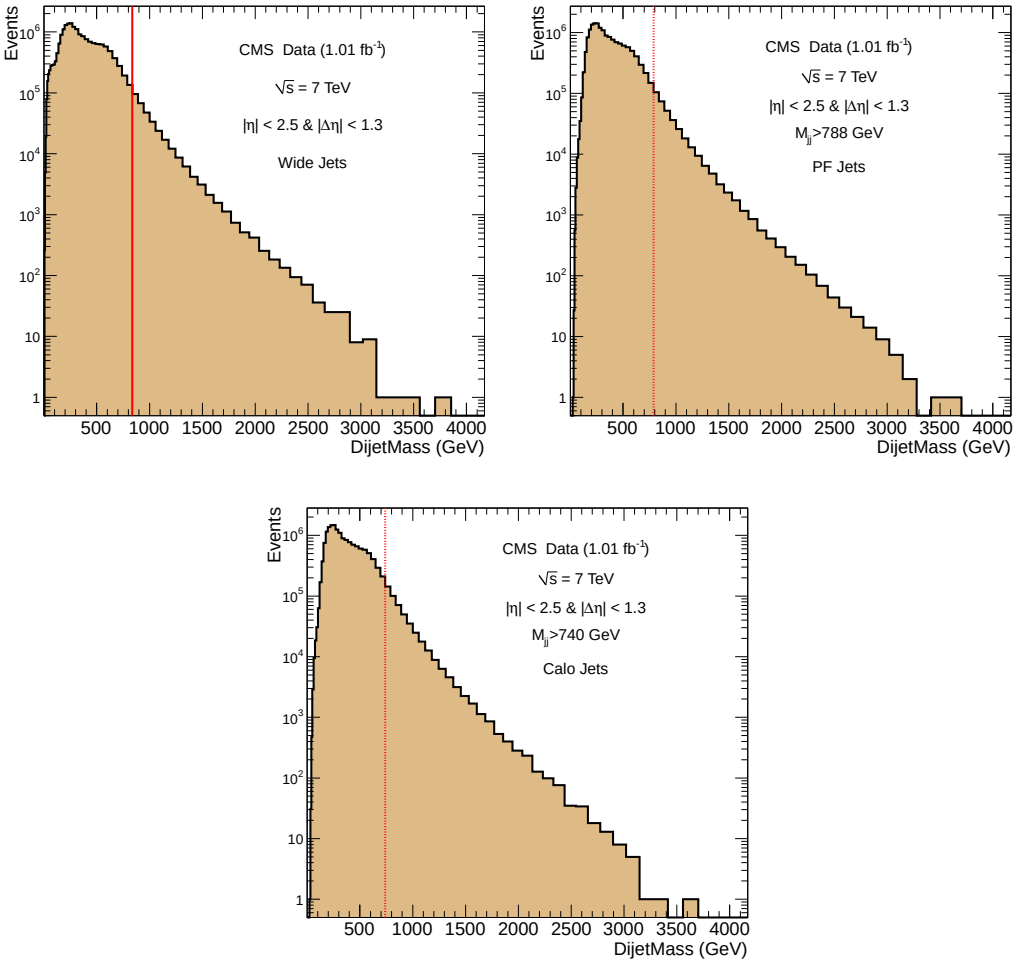

Figure 3.6: Number of events vs. dijet mass in GeV (histogram) requiring all cuts except the final dijet mass cut for trigger efficiency at $m = 838$, $m = 788$, $m = 740$ GeV (vertical line). - Wide Jet(top left), PF Jet(top right), Calo Jet(bottom)

.

3.5.2 Dijet Data Quality

The number of events in the analysis after the basic cuts are shown for each cut in table 3.2

Table 3.2: Cuts and Events for Wide Jet (top), PF Jet (middle), Calo Jet (Bottom)

Events after vertex cut	7656553
Events after dijet η cuts: $\|\Delta\eta\| < 1.3$ and $\|\eta\| < 2.5$	2503501
Events after dijet mass cut: $m > 838$ GeV	320103
Events after jet id cut	319282
Events after vertex cut	8196047
Events after dijet η cuts: $\|\Delta\eta\| < 1.3$ and $\|\eta\| < 2.5$	2074521
Events after dijet mass cut: $m > 788$ GeV	348053
Events after jet id cut	346573
Events after vertex cut	8196047
Events after dijet η cuts: $\|\Delta\eta\| < 1.3$ and $\|\eta\| < 2.5$	2070995
Events after dijet mass cut: $m > 740$ GeV	476366
Events after jet id cut	474872

The fraction of events rejected by jet ID criteria is very small, because the requirement that the two leading jets have a dijet mass $m > 838$ GeV (wide jets), $m > 788$ GeV (PF jets), and $m > 740$ GeV (calo jets). Also $|\eta| < 2.5$ and $|\Delta\eta| < 1.3$ enhance the jet purity. 699 events are rejected by wide jet ID, 1480 events by PF Jet ID, and 1494 events by calo jets ID.

After all cuts, we present some basic distributions indicating jet and event quality in following figures. In Fig. 3.7, we show the distributions of the variables of loose jet ID for calo jets after all other cuts. The upper left plot shows the Jet EMF, the fraction of jet energy in the ECAL. If the Jet EMF plot has a peak near either zero or one, it would indicate a problem from the HCAL or ECAL. Loose calo jet ID requires jet EMF> 0.01 and we find that the cut rejects no real jets in dijet events as discussed above. The upper right plot shows Jet fHPD, the fraction of jet energy in the hottest HCAL HPD. If the Jet HPD plot has a peak near one, it would indicate a problem from HPD noise. Loose calo jet ID requires jet fHPD< 0.98. The lower left plot shows Jet n90hits, the number of energy

ordered HCAL and ECAL RecHits containing 90% of the jet energy. The Jet n90hits plot does not have a peak near one which would indicate hot cells in the calorimeter for example from Ecal spikes. Loose calo jet ID requires jet n90hits > 1. The lower right plot shows Jet n90hits in log scale. Data and MC have similar shapes and show smoothly varying distributions for jet EMF, fHPD, and n90hits characteristic of real jets.

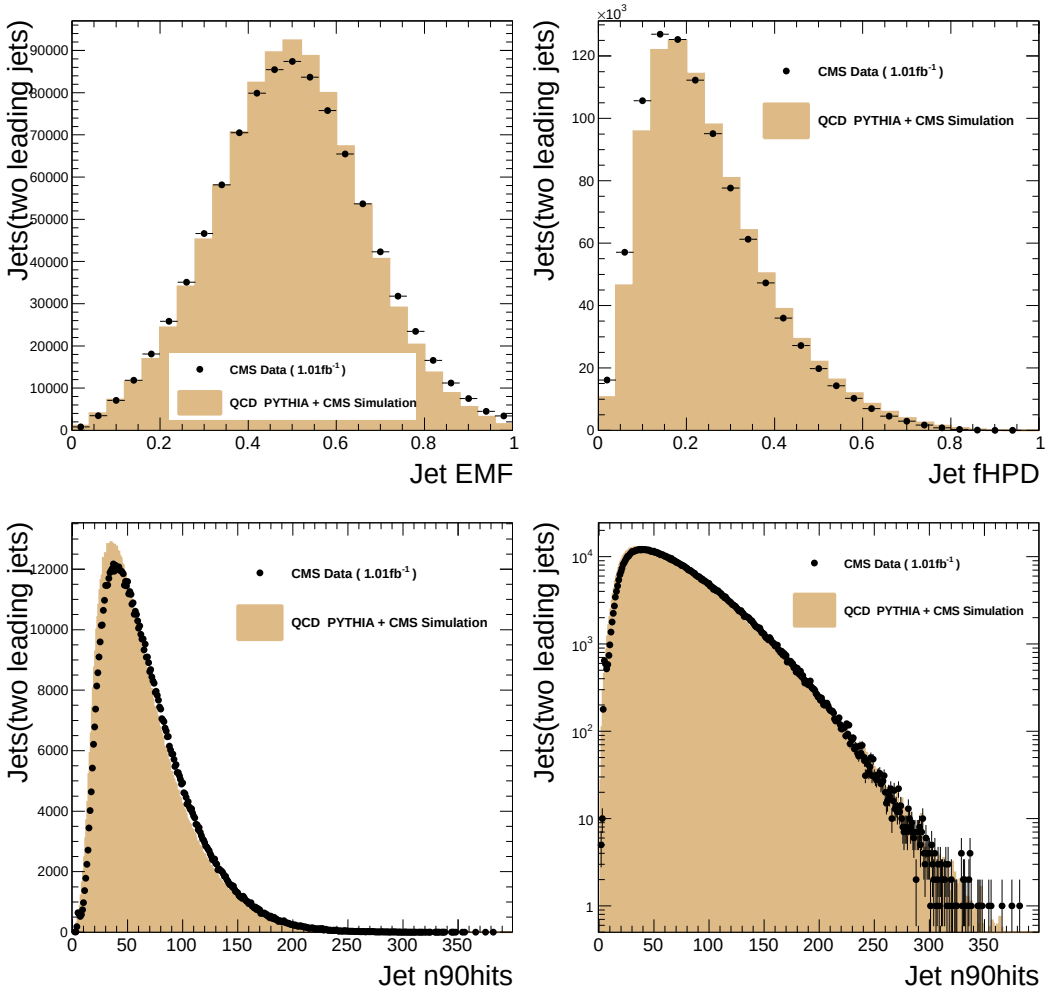

Figure 3.7: Jet ID Distributions for calo jets. The EM energy fraction of the two leading jets (upper left), the fHPD for the two leading jets (upper right), the n90hits for the two leading jets (lower left) and the same in log scale (lower right).

Fig. 3.8, and 3.9 show the distribution of the variables of tight jet ID for PF and wide jets after all other cuts. Since wide jet is made from PF jets, it also uses PF jet id to reject noise. Upper left plot shows distribution charged hadron fraction in jets. Tight PF

jet ID requires charged hadron fraction of jet bigger than 0 when $|\eta| < 2.4$. Upper right plot shows the distribution of neutral hadron fraction in jets. Tight PF jet ID requires that neutral hadron fraction of jets less than 0.9. Lower left plot shows distribution of electron fraction in jets. Tight PF jet ID requires that charged electromagnetic fraction less than 0.99 when $|\eta| < 2.4$. Lower right plot shows distribution of photon fraction in jets. Tight PF jet ID requires neutral electromagnetic fraction less than 0.9. All of these plots do not show any significant discrepancy between data and simulation but distribution of electron fraction in jets. The difference can be found around 1. All these jets are electrons.

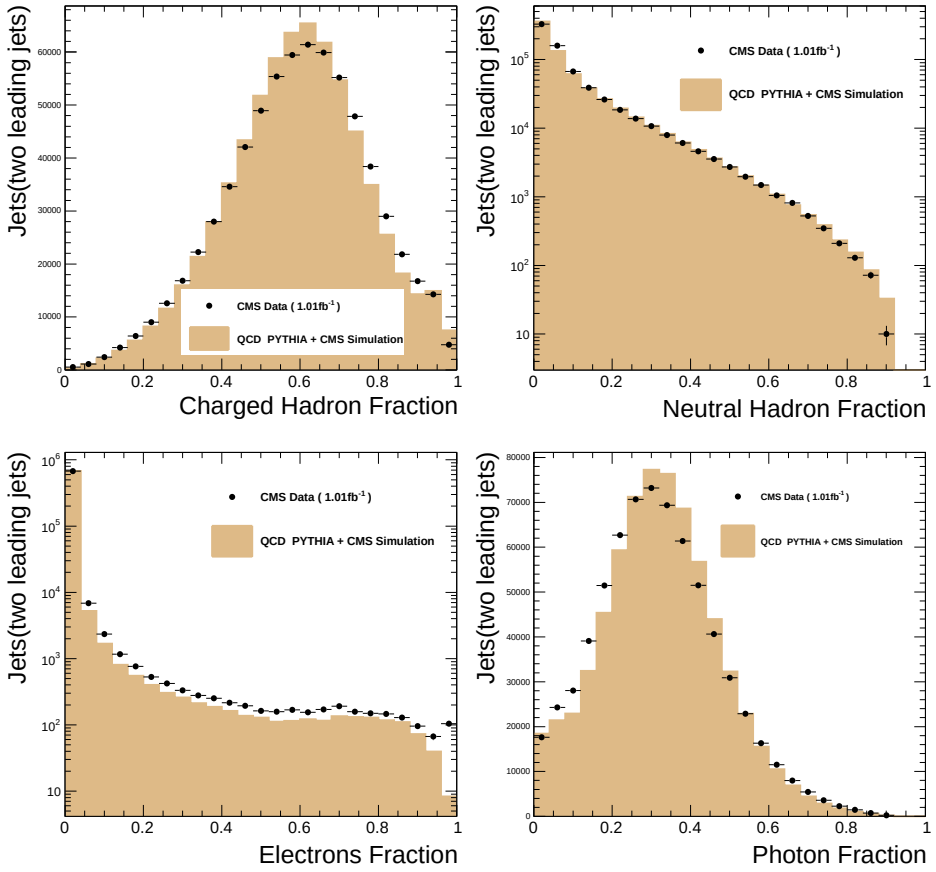

Figure 3.8: Jet ID Distributions for PF jets. The Charged Hadron fraction distribution (upper left), the Neutral Hadron Fraction distribution (upper right), the electrons fraction distribution in log scale(lower left) and the Photon fraction distribution(lower right).

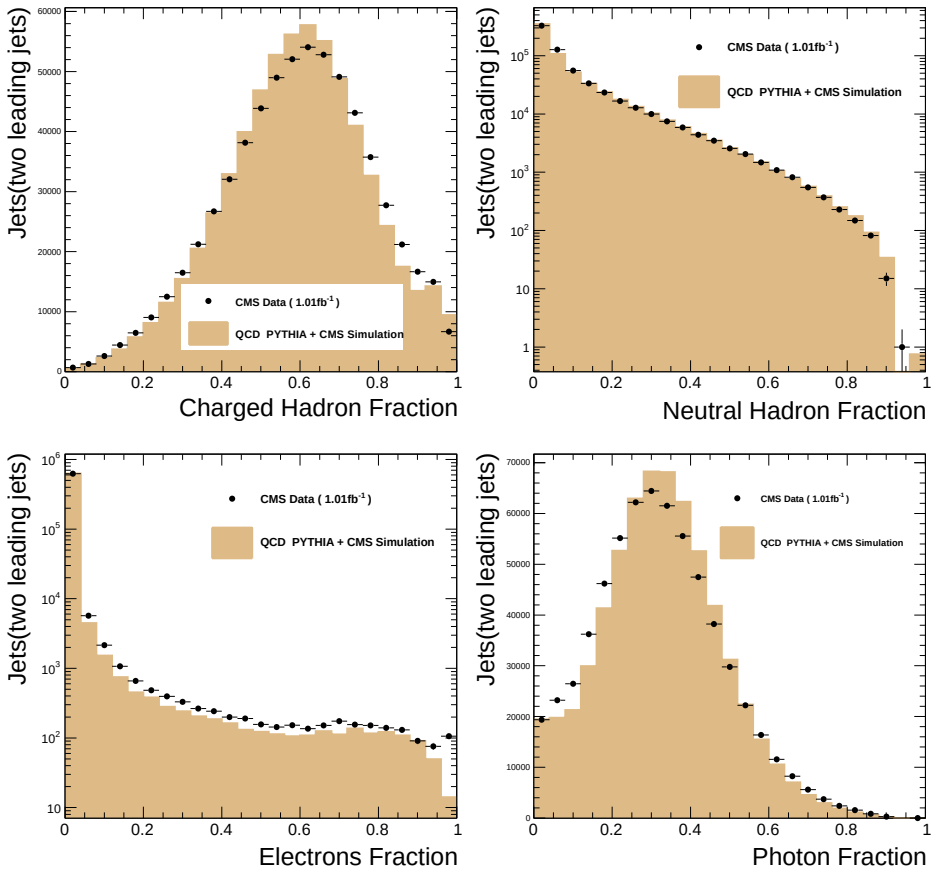

Figure 3.9: Jet ID Distributions for wide jets. The Charged Hadron fraction distribution (upper left), the Neutral Hadron Fraction distribution (upper right), the electrons fraction distribution in log scale(lower left) and the Photon fraction distribution(lower right).

These jet ID variables give us confidence that the jets in this analysis do not originate from backgrounds.

In Fig. 3.10, we show the number of good tracks associated with either of the two leading jets. Our leading jets generally have many associated tracks. Very few of the leading jets in both sinulation and data have no associated tracks at the calorimeter face, and there are virtually no leading jets without associated tracks at the vertex. The track multiplicity distributions do not have a peak at zero tracks, which would indicate calorimeter backgrounds. The track multiplicity distribution gives us additional confidence that the

calorimeter jets in this analysis come from pp collisions. Note that data has significantly more pileup than the MC which affects the track multiplicity distribution.

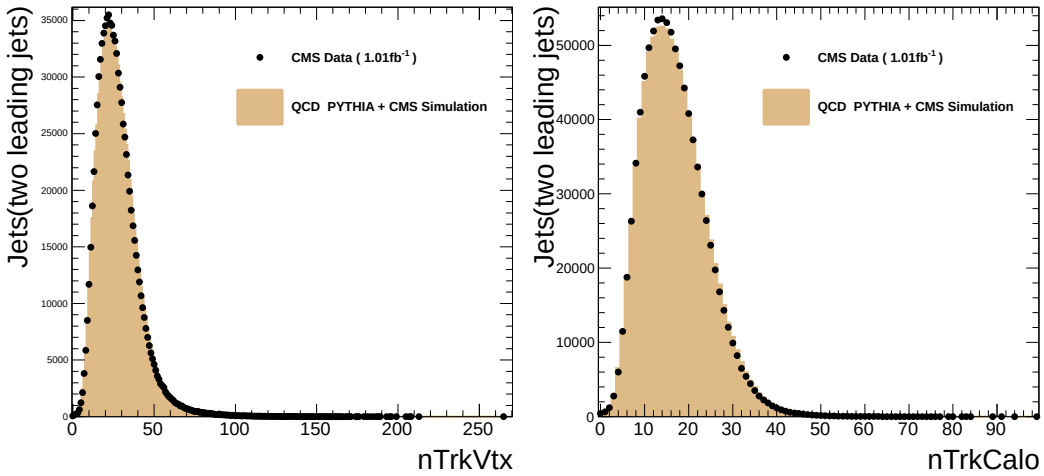

Figure 3.10: left) The multiplicity of tracks associated to two leading jets at the vertex right) The multiplicity of tracks associated to two leading jets at the calo face

Fig. 3.11, 3.12, and 3.13 show some event balance distributions. The upper plots show missing E_T divided by total E_T in linear scale and log scale. The dijet events have low MET/ΣE_T, the ratio of the magnitude of the vector and scalar sums of the energies of Calo-Towers for calo jets and stable reconstructed particles for PF and wide jets. The MET/ΣE_T distribution shows that the event energy is well balanced in the transverse plane. Large background from calorimeter noise, beam halo, or cosmic rays will typically produced large values of MET/ΣE_T, which we do not observe in this data. The two lower plots in Fig. 3.11, 3.12, and 3.13 show the ϕ difference of two leading jets in linear scale and log scale. The two leading jets are predominantly back-to-back in ϕ as expected for dijets with a tail to small values of $\Delta\phi$ produced by radiation and multi-jet events. Data and simulation have similar shapes and show smoothly varying distributions for MET/ΣE_T and $\Delta\phi$ characteristic of dijet events. These distributions give us confidence that we are observing events with a dijet topology, not unphysical backgrounds.

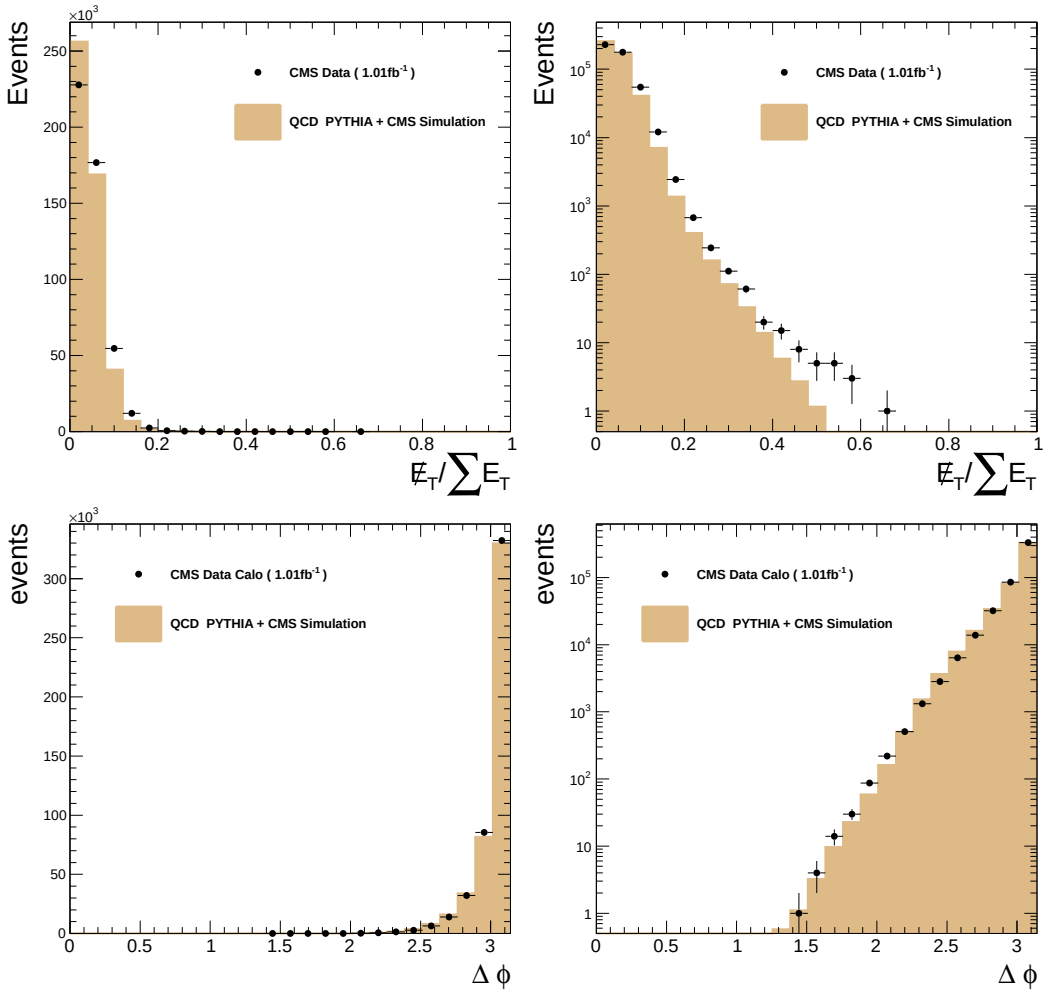

Figure 3.11: Event balance distributions for calo jet. Missing calorimeter E_T divided by total calorimeter E_T (upper left) and the same in log scale (upper right). The ϕ difference of the two leading jets (lower left) and the same in log scale (lower right).

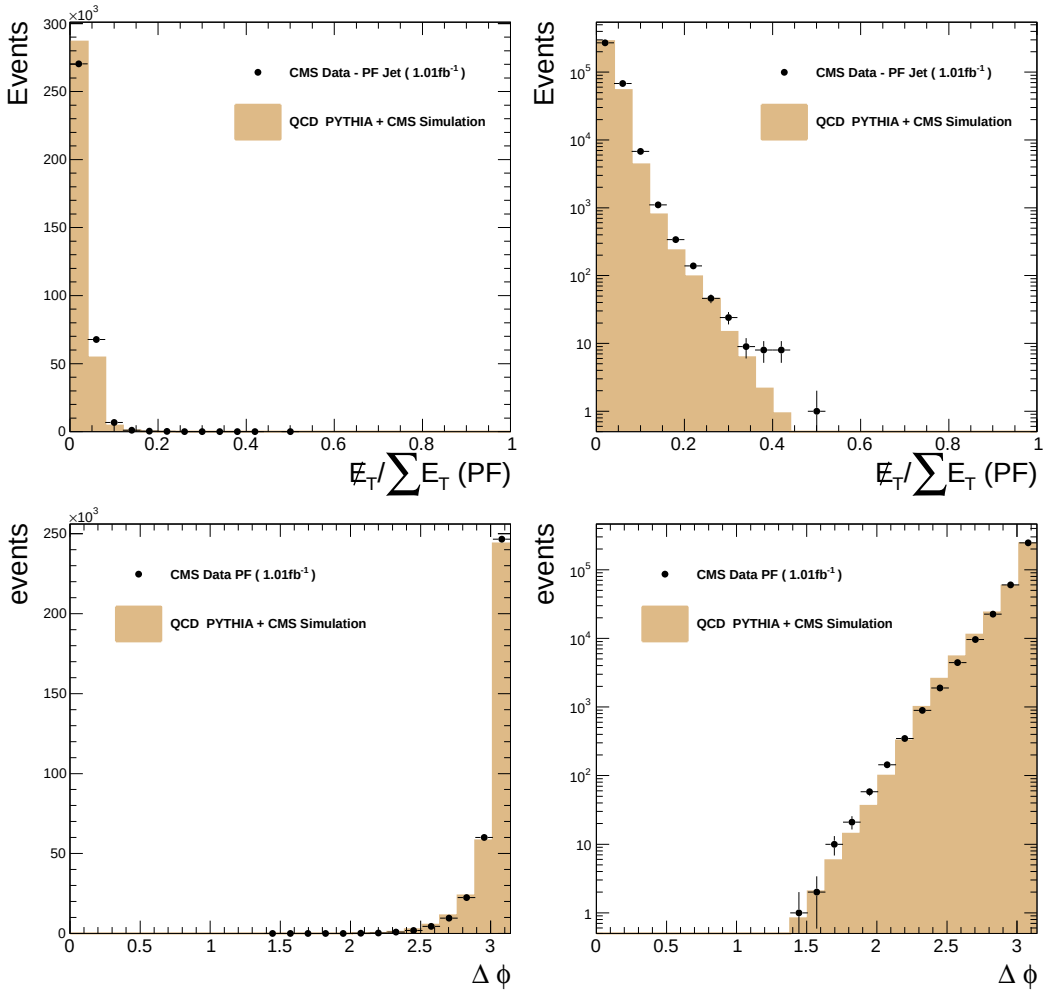

Figure 3.12: Event balance distributions for PF Jets. Missing calorimeter E_T divided by total calorimeter E_T (upper left) and the same in log scale (upper right). The ϕ difference of the two leading jets (lower left) and the same in log scale (lower right).

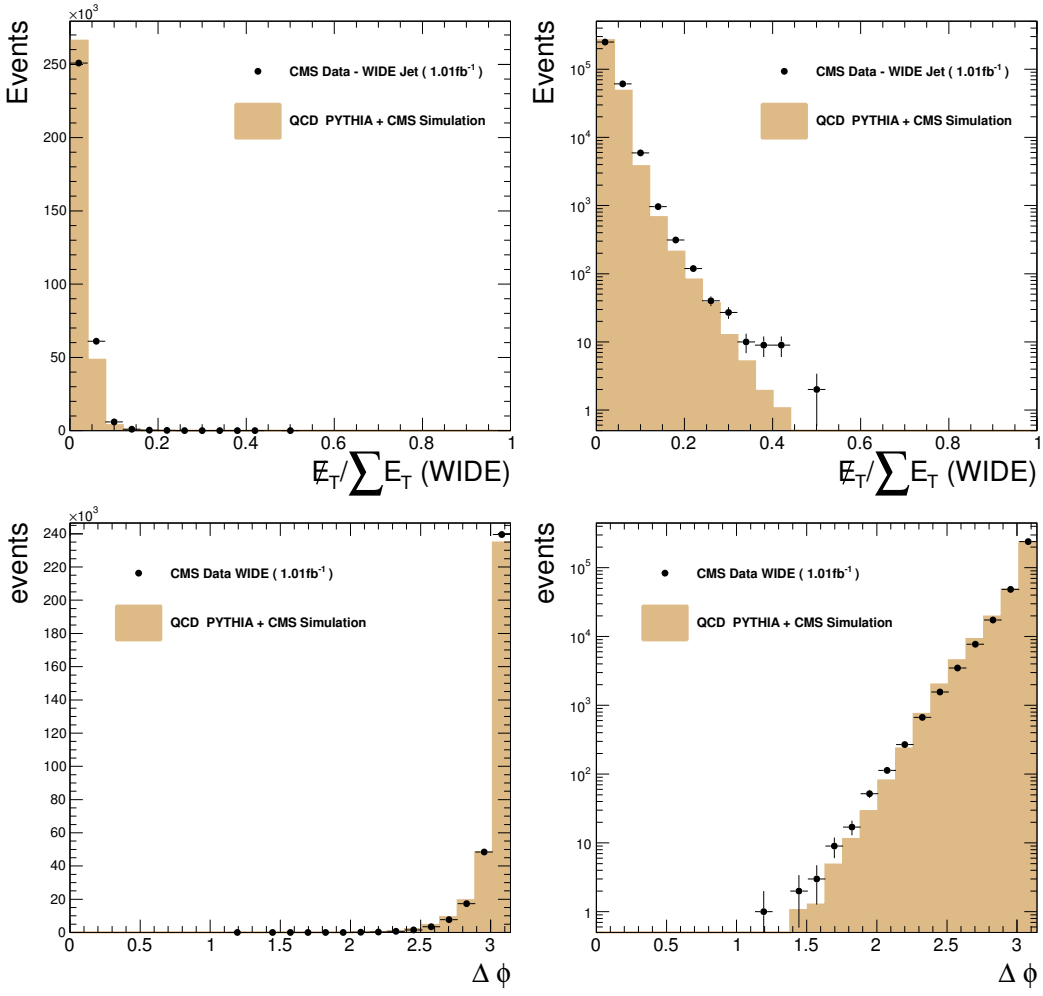

Figure 3.13: Event balance distributions for wide Jets. Missing calorimeter E_T divided by total calorimeter E_T (upper left) and the same in log scale (upper right). The ϕ difference of the two leading jets (lower left) and the same in log scale (lower right).

Fig. 3.14, 3.15, and 3.16 show some distributions of basic jet kinematic variables. Upper two plots show the corrected p_T distribution in linear and log scale for two leading jets. The p_T distribution falls steeply with increasing p_T, and turns over at low p_T due to the dijet mass cut $m > 740$ GeV (Calo), $m > 788$ GeV (PF), and $m > 838$ GeV (wide) . The jet p_T distributions for data and simulation are in good agreement considering uncertainties in the JES, and the modelling of the p_T distribution in PYTHIA. Middle left plot shows the η distribution for two leading jets. The η distribution of the two leading jets is in reasonable agreement with the shape predicted by simulation and there are no regions with significant rate deviations that could arise due to significant mis-understanding of jet response after all corrections. Middle right plot shows the distribution of $\Delta\eta$ between two leading jets. The $\Delta\eta$ distribution demonstrates the characteristic forward peaks from Rutherford-like QCD scattering at fixed invariant mass, and the very slight deviations in shape between data, and simulation are expected from NLO effects on the angular distribution. Lower left plot shows the ϕ distribution of two leading jets. The ϕ distribution of the two leading jets is flat with an RMS of only 1.2% for calo and PF jets and 0.9% for wide jets. Lower right plot shows the η -ϕ distribution of two leading jets. The η -ϕ distribution of two leading jets is reasonably uniform. These distributions show that the jets in this data sample have the kinematics expected for dijets from QCD.

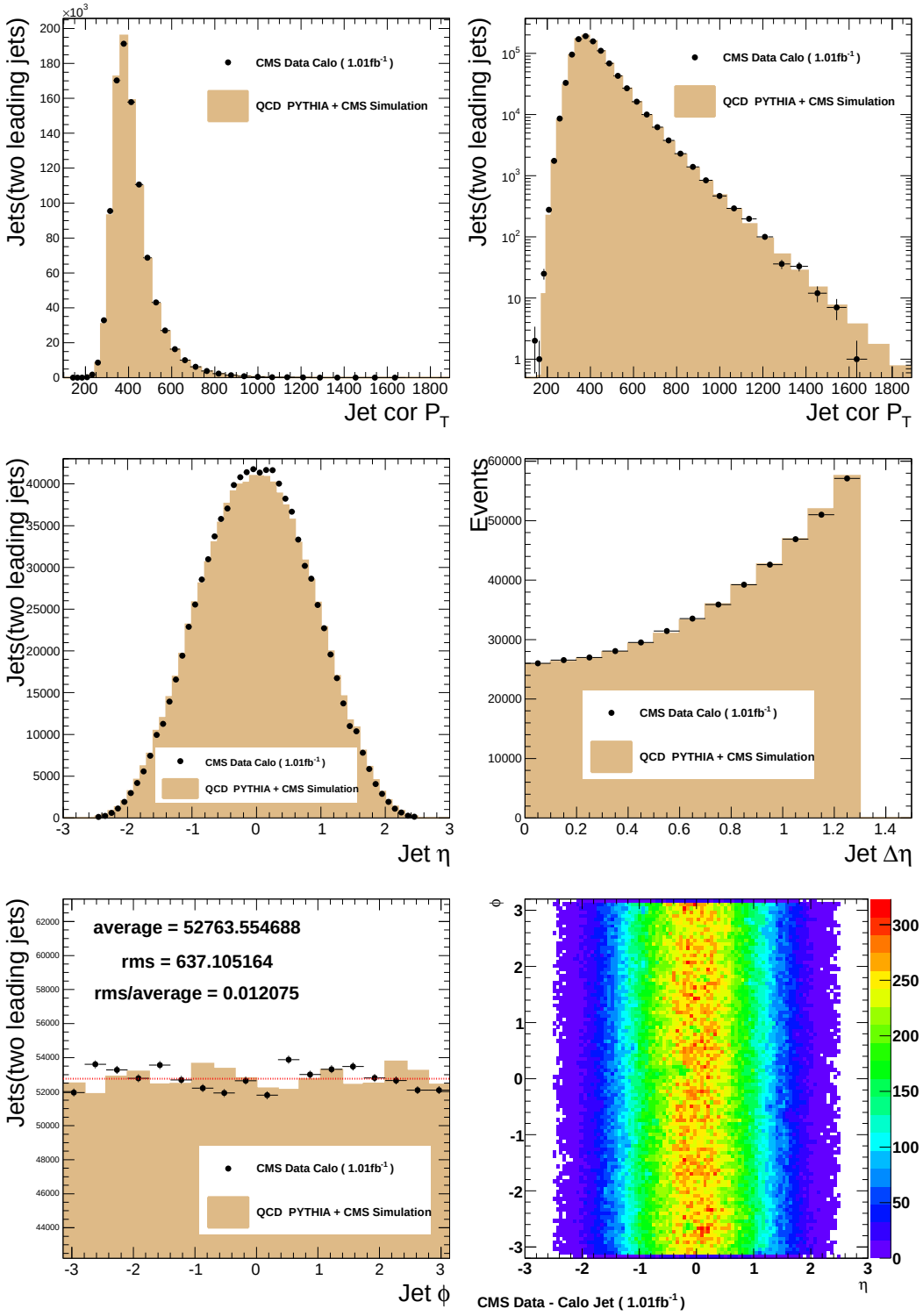

Figure 3.14: Jet kinematics distributions for calo jets. The corrected P_T of the two leading jets (upper left) and the same in log scale (upper right). The η distribution for the two leading jets (middle left). The ϕ distribution for the two leading jets. (middle right) ϕ vs. η (lower left) for the two leading jets. The $\Delta\eta$ distribution (lower right)

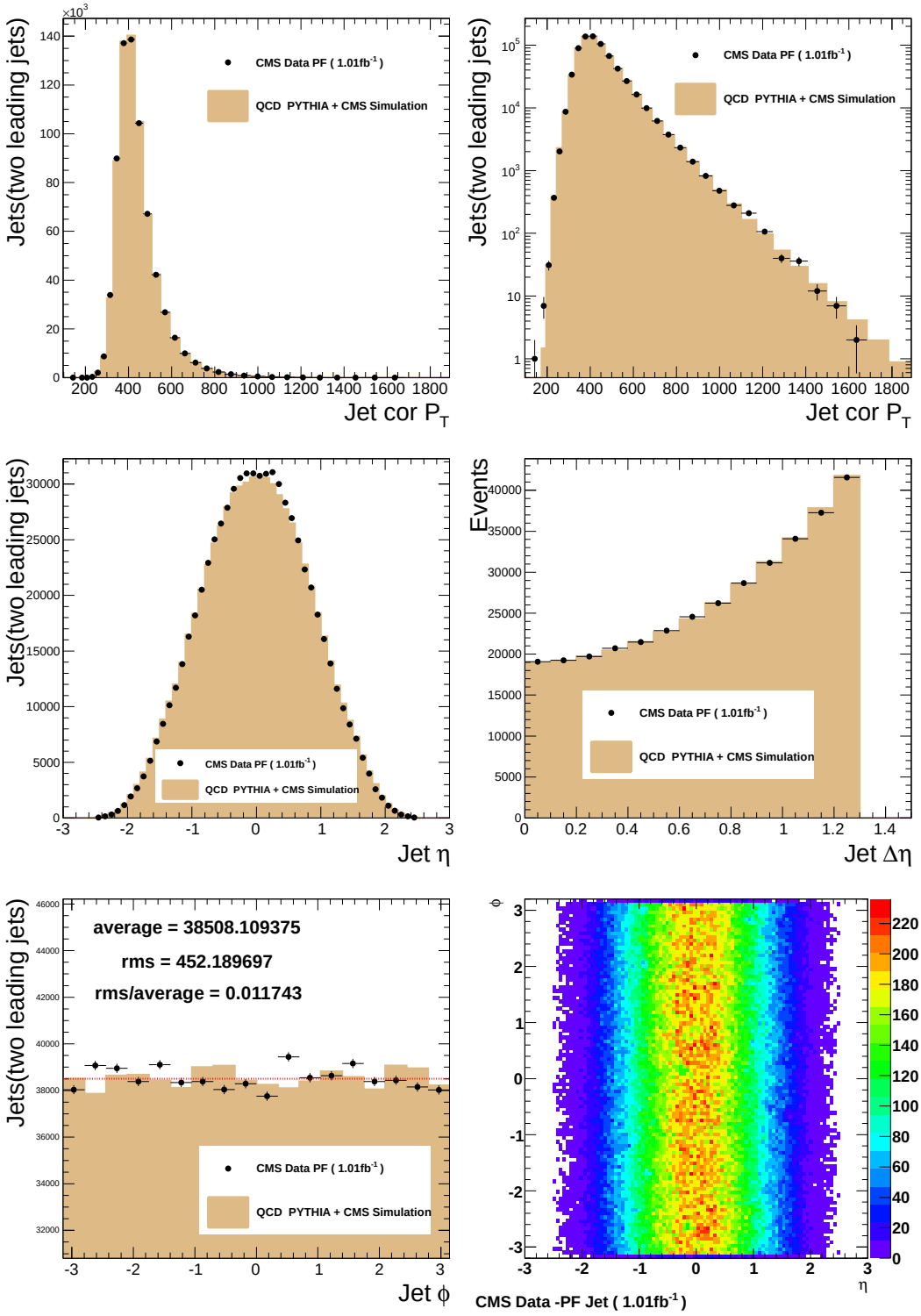

Figure 3.15: Jet kinematics distributions for pf jets. The corrected P_T of the two leading jets (upper left) and the same in log scale (upper right). The η distribution for the two leading jets (middle left). The ϕ distribution for the two leading jets. (middle right) ϕ vs. η (lower left) for the two leading jets. The $\Delta\eta$ distribution (lower right)

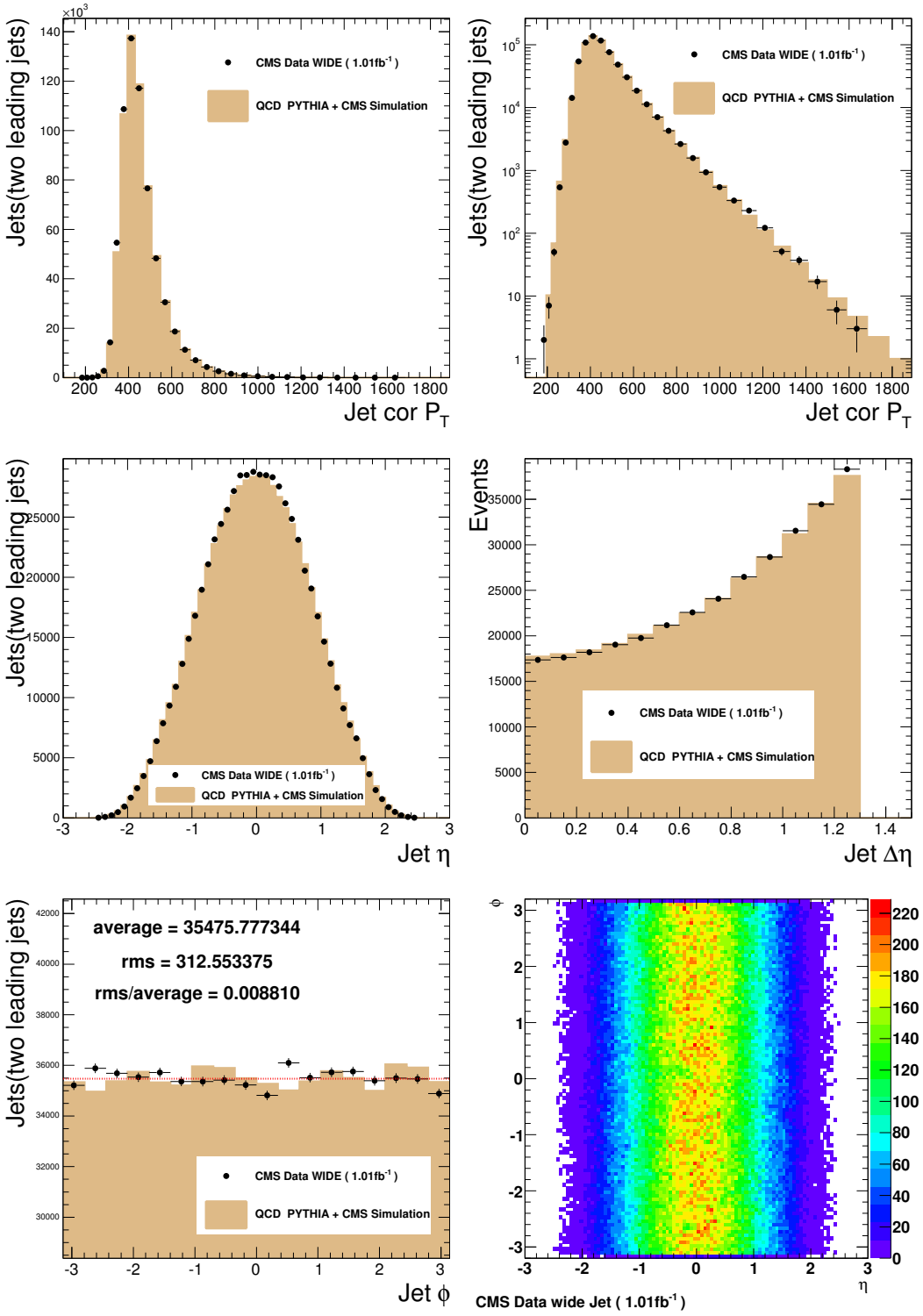

Figure 3.16: Jet kinematics distributions for wide jets. The corrected P_T of the two leading jets (upper left) and the same in log scale (upper right). The η distribution for the two leading jets (middle left). The ϕ distribution for the two leading jets. (middle right) ϕ vs. η (lower left) for the two leading jets. The $\Delta\eta$ distribution (lower right)

3.5.3 Calo, PF, wide Jet comparison

Fig 3.17 shows the dijet mass spectrum from wide Jets (black points), PF Jets (red boxes), and Calo Jets (blue Xs). The overall spectrum shows no big discrepancies between three algorithms. However, it can be easily noticed that the dijet mass distribution of wide jet is shifted to higher mass region. It is because wide jets combine nearby jets into two leadiing jets.

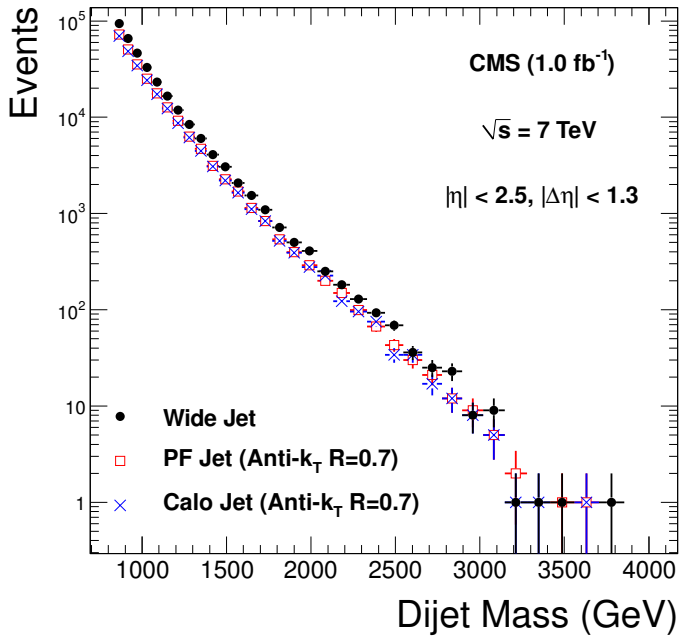

Figure 3.17: The dijet mass spectrum from wide Jets black points) is compared to the dijet mass sepectrum from PF Jets (red boxes) and Calo Jets (blue Xs)

In Fig 3.18, PF dijet mass is compared to calo dijet mass event by event. The ratio of corrected dijet mass from PF jets to corrected dijet mass from calo jets as a function of corrected dijet mass from calo jets event by event for ak5 is in upper left plot and for ak7 is in upper right plot. Lower left plot shows the ratio distribution for events which has calo dijet mass greater than 2.332 TeV for ak5, and lower right plot shows it for ak7. The difference beween PF and calo dijet mass is less than 0.5%. Since the JEC uncertainty is bigger(2.2%), PF and Calo dijet mass is in reasonable agreement.

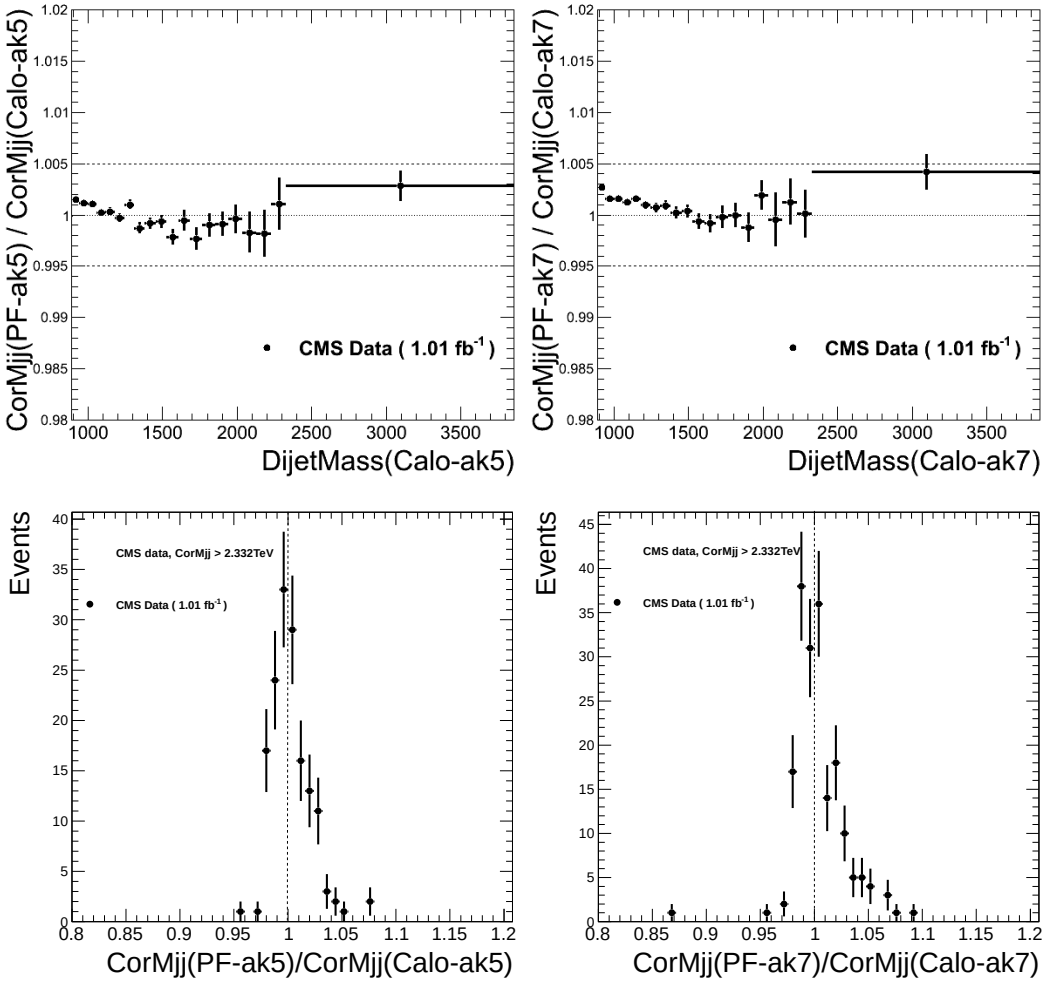

Figure 3.18: The ratio of corrected dijet mass from PF jets to corrected dijet mass from calo jets vs corrected dijet mass from calo jets event by event for ak5. (upper left) The ratio distribution for events which has calo dijet mass greater than 2.332 TeV for ak5. (upper right) The ratio of corrected dijet mass from PF jets to corrected dijet mass from calo jets vs corrected dijet mass from calo jets event by event for ak7. (bottom left) The ratio distribution for events which has calo dijet mass greater than 2.332 TeV for ak7. (bottom right)

3.5.4 Spectrum and QCD

The measured dijet mass spectrum is shown in Fig. 3.19. In Fig. 3.19, points represent data and histogram represents QCD MC simulation. Also the yellow band in Fig. 3.19 shows the systematic uncertainty in the spectrum due to JES. The mass spectrum is defined by

$$\frac{d\sigma}{dm} = \frac{1}{\int Ldt}\frac{N_i}{\Delta m_i} \tag{3.3}$$

where m is the dijet mass; N_i is the number of events in the i-th dijet mass bin; Δm_i is the width of the i-th dijet mass bin; and the integrated luminosity is $\int Ldt$. This data is also tabulated in Appendix B. The bin width is approximately the dijet mass resolution, and gradually increases as a function of mass. The data is compared to a QCD prediction from the PYTHIA MC and the full CMS simulation. The normalzation of the QCD prediction has been multiplied by a factor of 1.33 for wide jets to match the data. Also shown in Fig. 3.19 is the sensitivity of the QCD + CMS simulation to the systematic uncertainty in the JES [32]. The vertical error bars on the data are Poisson uncertainties, the horizontal bars are the bin widths. Bins with zero events are indicated by a Poisson vertical error bar extending up to 1.8 events.

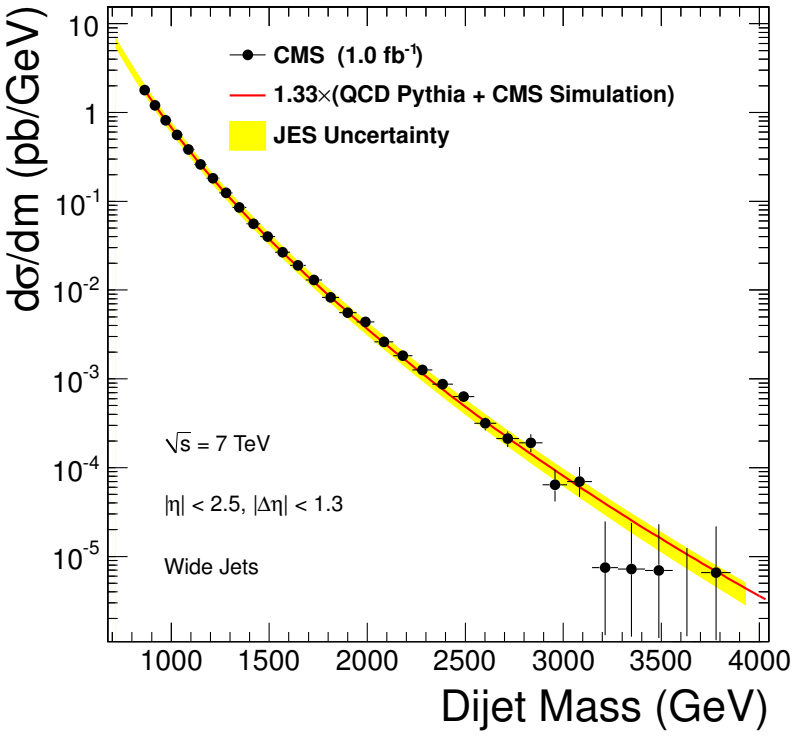

Figure 3.19: The dijet mass spectrum data (points) is compared to a QCD MC prediction (histogram).

In Fig. 3.20, we show the ratio of the data to the PYTHIA prediction which demonstrates at a fine scale the level of agreement between data and PYTHIA. Again the QCD prediction has been multiplied by a factor of 1.33 to normalize it to the data and the yellow band shows the systematic uncertainty in the spectrum due to jet energy. Fig. 3.20 shows that the PYTHIA QCD MC prediction is in good agreement with the data.

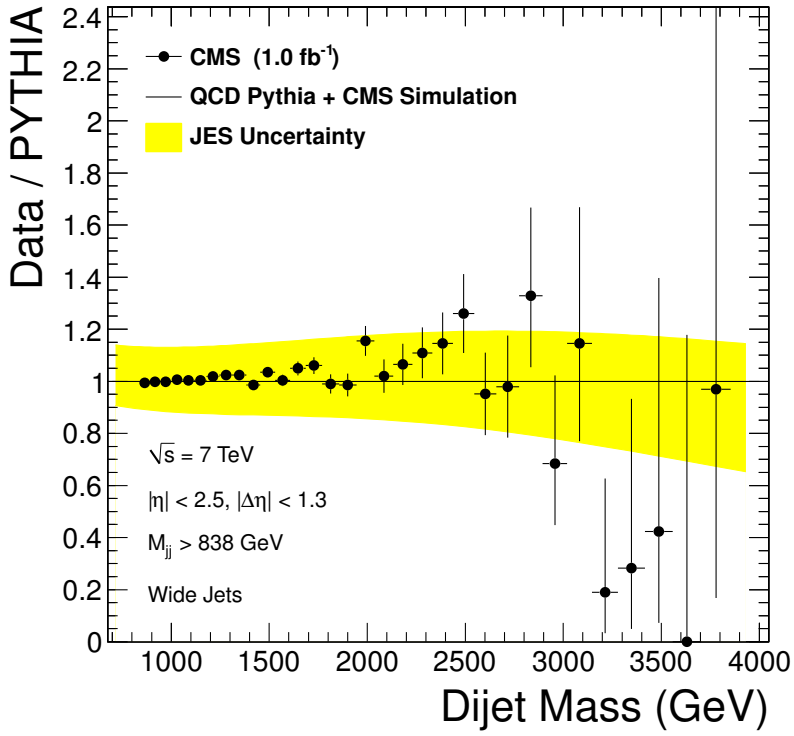

Figure 3.20: Ratio of the dijet mass spectrum divided by the QCD Pythia prediction for wide jets.

3.6 Highest Mass Dijet Events.

Event displays of the ten highest mass dijet events are shown in Appendix C. They all look like good events, with collimated calorimeter energy deposits and associated tracks. Table C.1 in the Appendix lists the basic properties of the leading jets for these events. The highest dijet mass observed is at 3.8 TeV as already mentioned.

3.7 Dijet Mass Spectrum and Fit

Fig. 3.21 shows the dijet mass spectrum from Fig. 3.19 compared to a fit. Here we model the background to a dijet resonance coming from SM dijet production using a simple parameterization. Our first test for whether there is a bump or other local effect in the data is to simply see if we can get a good fit to a smooth parameterization. Fig. 3.21 also shows the parameterization fitted to the data. We get a χ^2 of 27.51 for 28 degrees of freedom for

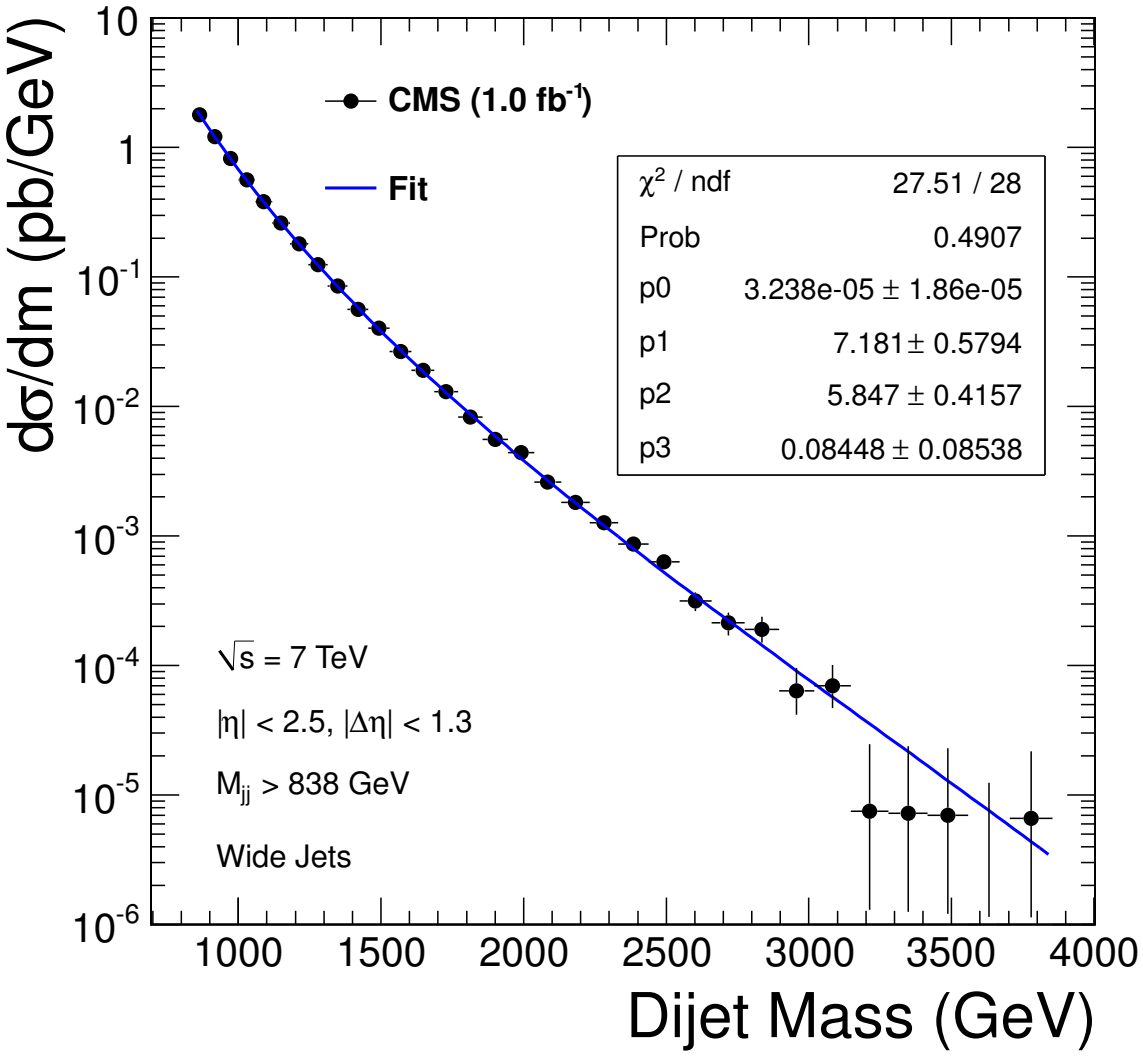

Figure 3.21: The dijet mass distribution (points) compared to a smooth background fit wide jets (solid curve).

the fit to the dijet mass distribution of wide jets. They are 26.57/28 for PF jets and 30.12/29 for calo jets.

$$\frac{d\sigma}{dm} = \frac{P_0(1-m/\sqrt{s})^{P_1}}{(m/\sqrt{s})^{P_2+P_3 ln(m/\sqrt{s})}} \tag{3.4}$$

Left plot of Fig 3.22 shows the fractional differences between data and the fit function, (data-fit)/fit, which shows no significant evidence of a peaks above the background fit. In the fractional difference plot the error bars are in units of the fit in the bin. Right plot of Fig 3.22 show the pulls, defined as *(Data-Fit)/Error*, which are consistent with statistical fluctuations and are scattered around zero. In the pulls plot, the error bars are always exactly 1 because they are in units of the error in the bin.

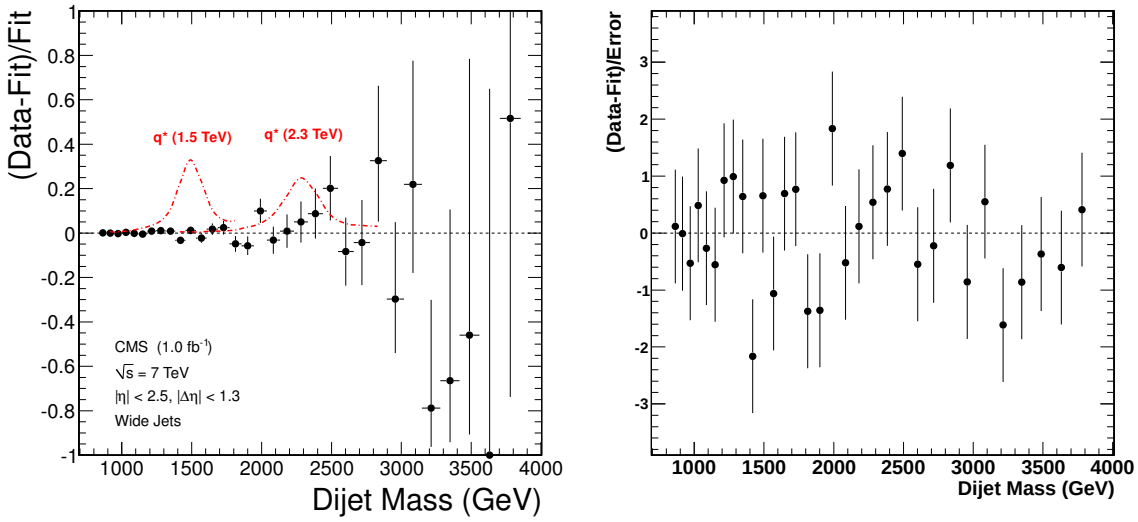

Figure 3.22: Left) The fractional difference between the dijet mass distribution (points) and a smooth background fit as a function of dijet mass for wide jets. Right) The pulls distribution (Data-Fit)/Error as a function of dijet mass.

3.7.1 Fit to Dijet Mass Spectrum with Various Parameterizations

In Fig. 3.23, we show the dijet mass distribution, $d\sigma/dm$, fit with three different parameterizations: our default 4 parameter fit and two alternate fits.

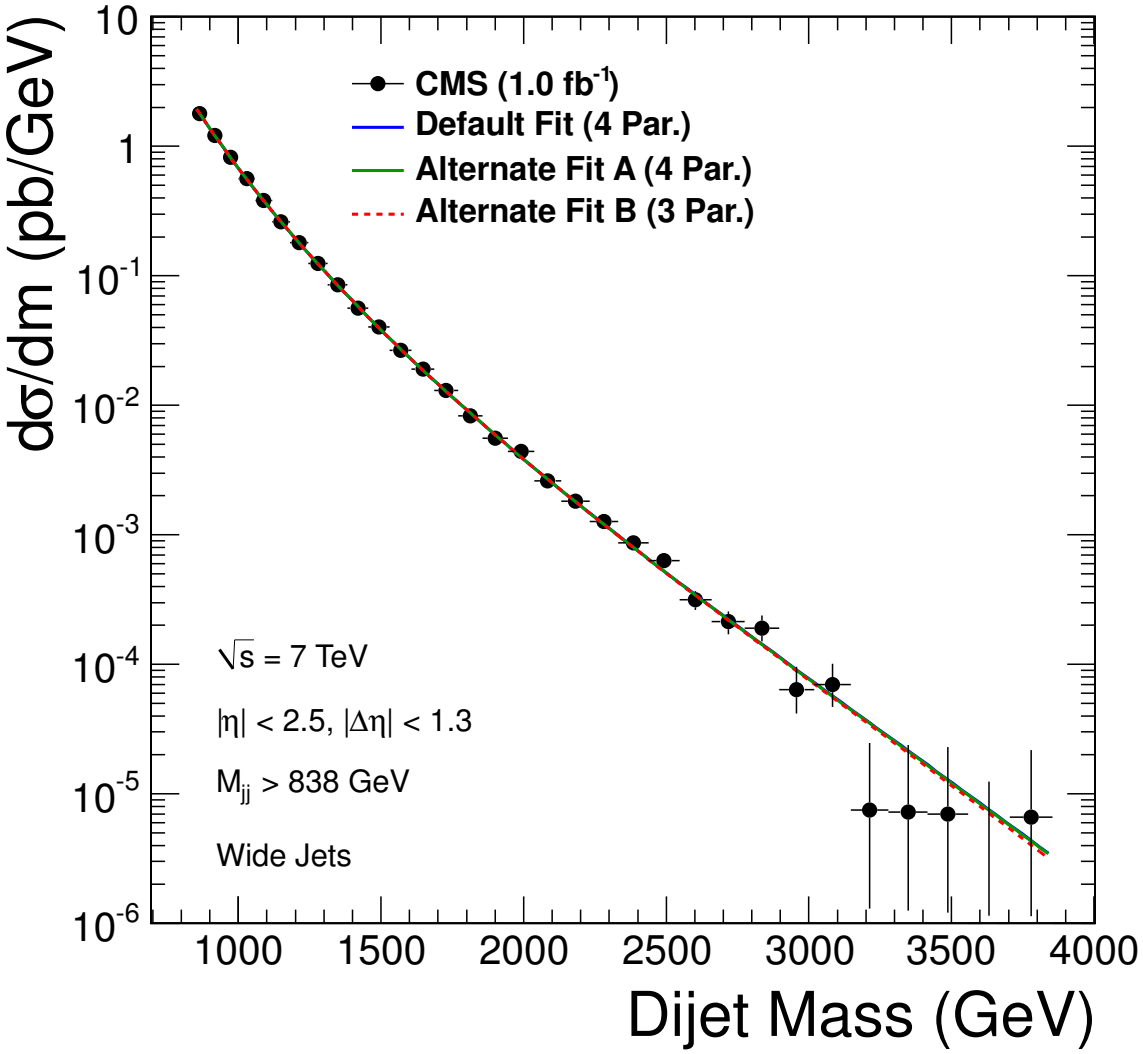

Figure 3.23: The dijet mass data (points) is compared to fits for wide jets(curves) using our default fit function and three alternate fit functions.

The parameterizations are listed in equation 3.5.

$$\begin{aligned}
\frac{d\sigma}{dm} &= \frac{P_0 \cdot (1 - m/\sqrt{s})^{p_1}}{(m/\sqrt{s})^{p_2 + p_3 ln(m/\sqrt{s})}} \text{ (Default Fitwith 4 parameters)} \\
&= \frac{P_0 \cdot \left(1 - m/\sqrt{s} + P_3 \cdot (m/\sqrt{s})^2\right)^{P_1}}{m^{P_2}} \text{ (Alternate Fit A with 4 parameters)} \\
&= \frac{P_0 \cdot (1 - m/\sqrt{s})^{P_1}}{m^{P_2}} \text{ (Alternate Fit B with 3 parameters).}
\end{aligned} \tag{3.5}$$

The default four-parameter function was used by CMS in the published paper based on 3 pb^{-1} and 1 fb^{-1}, CDF in run II [33] , and is used by ATLAS [30]. It gives a good fit with $\chi^2/DF = 27.51/28$ for wide jets $26.57/28$ for PF jets and $30.12/29$ for calo jets. We have also explored two alternate parameterizations. All parameterizations have a power law in them, because we cannot get a good fit with only 3 or 4 parameters without a power law.

Alternated fit B is a three-parameter fit that was used by CDF in run IA [34] and has the simplest QCD motivation, although all the parameterizations are motivated in a similar fashion. It was used in much earlier versions of this CMS analysis with significantly less luminosity. It has a term in the numerator motivated by the parton distribution fall off with fractional momentum, the same term as in the numerator of our default fit. It includes a power law fall off with mass in the denominator, motivated by the QCD matrix element. It also fits the data well.

Alternate fit A is a four-parameter function that was used by CDF in run IB. [35] It similar to alternate fit B, except it has an additional term in the numerator to give flexibility beyond the 3-parameter fit. It also fits the data well.

Figure 3.24 shows the fractional differences between data and the fit function, (data-fit)/fit, and the pulls, (data-fit)/error, for all three fits.

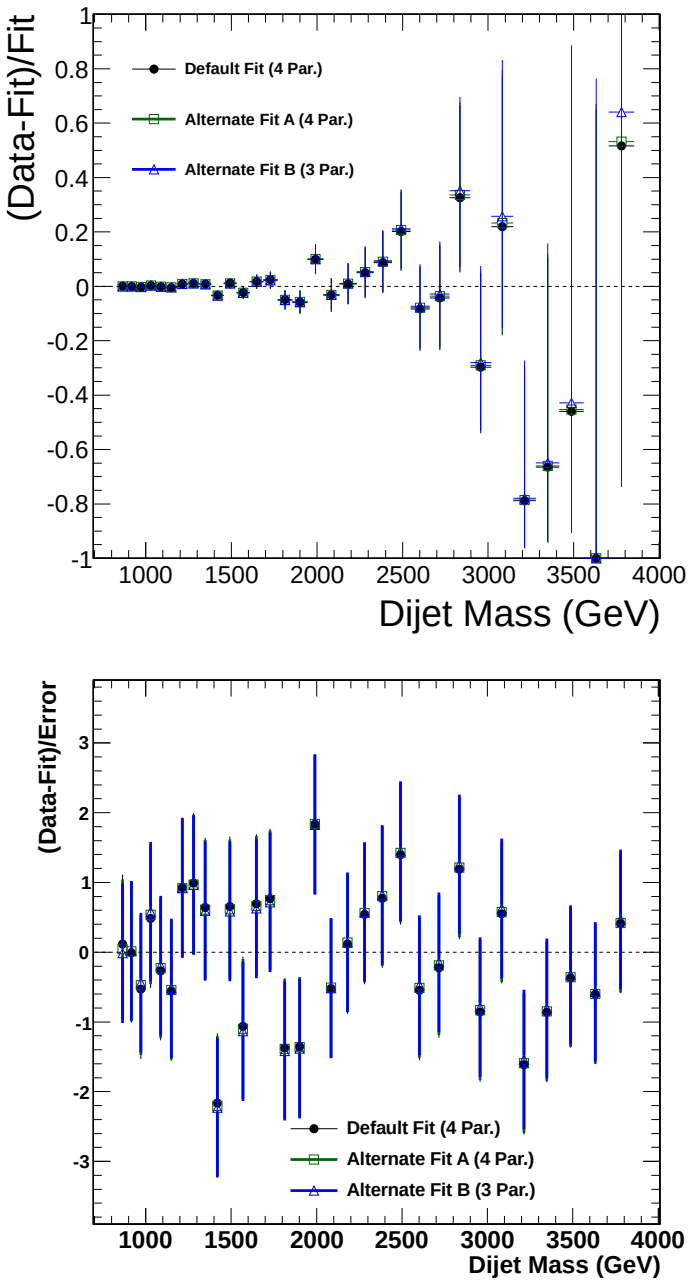

Figure 3.24: Top) Fractional difference (points) between the dijet mass distribution data and four fits as a function of dijet mass for wide jets. Bottom) Pulls for the data (points) compared to four fits as a function of dijet mass.

Chapter 4

Search for Dijet Resonance

4.1 The Signal: Dijet Resonance Shape

Since this analysis search for general narrow dijet resonances not a specific model of dijet resonance production, only a model of the resonance line shape is required. If the natural width of resonance is narrow enough compared to the CMS dijet mass resolution, the natural width does not affect the resonance shape. So this analysis only focuses on resonances which has narrow natural width compared to the CMS dijet mass resolution. There are three types of parton pairs in the resonance decay. They are qq, qg, or gg. We obtain generic shapes for these three types of parton pairs from the processes of $qg \to q* \to qg$, $q\bar{q} \to G \to q\bar{q}$, and $gg \to G \to gg$. These are produced using PYTHIA MC + CMS Summer11 simulation at five different masses of 0.5, 0.7, 1.2, 2,0 and 3.5 TeV. In Fig. 4.1, we present four of these five resonance shapes. Fig. 4.1 present 0.7, 1.2, 2.0 and 3.5 TeV resonance shapes. We use resonances with the mass from 1.0 TeV to 4.1 TeV in this analysis.

Fig. 4.1 shows the shapes from wide jets. Here are three effects

- The tail to low mass of the dijet mass distribution become longer as the number of gluon is increased (gg has longest tail and qq has the shortest)
- The peak position of the resonance decreases as the number of gluons is increased (the gg resonance dijet mass distribution peaks are at lower mass than the qq dijet mass distribution)

- The effective width of the resonance increases as the number of gluons is increased: the gg resonance dijet mass distribution is wider than the qq dijet mass distribution

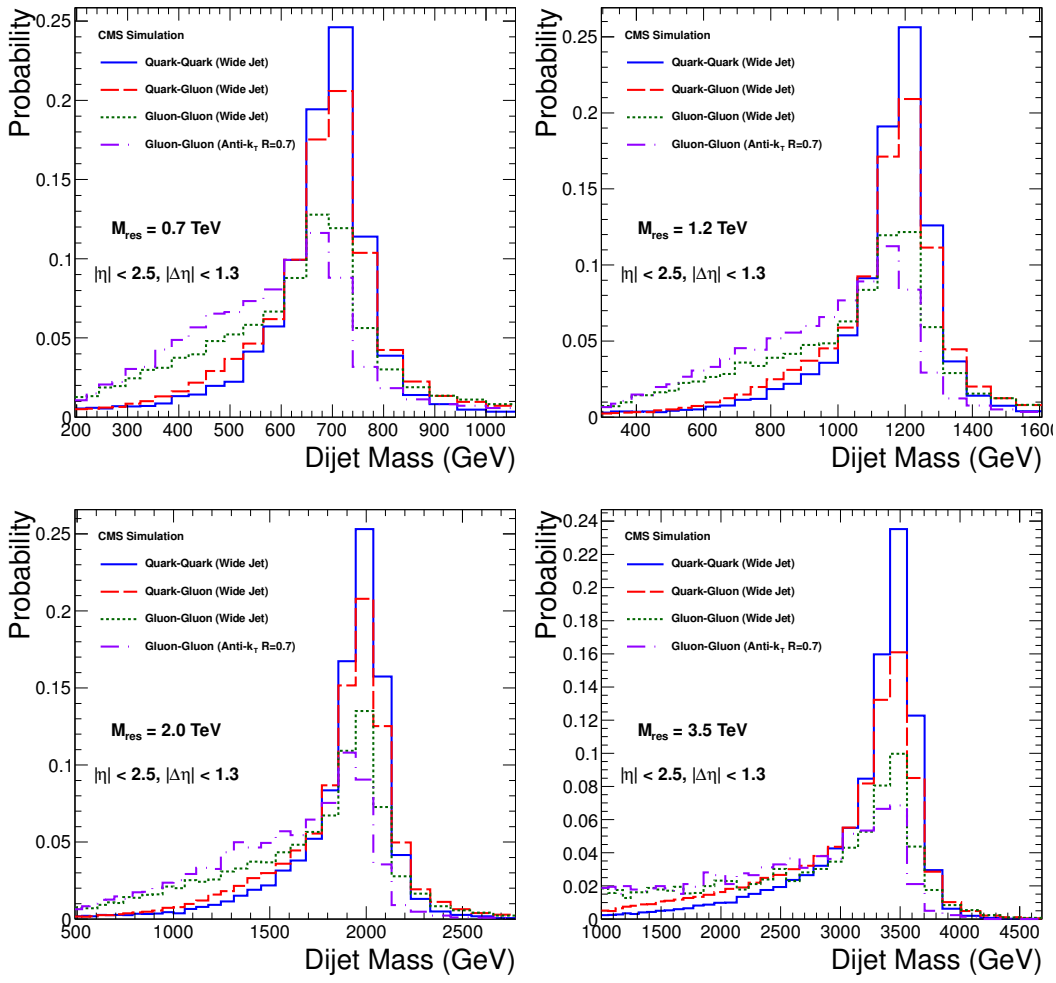

Figure 4.1: Dijet mass distribution for $q\bar{q}$ (qq), qg and gg resonances at 0.7, 1.2, 2 and 3.5 TeV resonance mass.

As we see here, these differences are related with number of gluons in the resonances. This analysis uses three generic types of resonances because of different dijet resonance shapes between resonances decaying to qq, qg, and gg . The investigation of source of these differences is studied to understand the signal shapes better.

4.1.1 Effect of initial state radiation

Initial state radiation is the radiation from quarks or gluons in proton before collision. We made PYTHIA MC + CMSSW simulation without the initial state radiation to check its effect. The shape study uses $\sqrt{s} = 10TeV$ not $7TeV$. However, the basic concept of this section is same for both center of mass energy. Turning off initial state radiation is unphysical and MC dependent, but we can demonstrate roughly the effect of the radiation. If initial state radiation fall into the area of leading jets and merged into them, this increase the energy of leading jets and dijet mass. This makes high mass tail in dijet mass distribution.

Fig.4.2, 4.3, and 4.4 show the x distributions (dijet mass divided by resonance mass) for 0.7, 2.0 and 5.0 TeV resonances both with and without initial state radiation. In those figures, the resonance shapes without initial state radiation have a shorter high mass tail than the resonance shapes with initial state radiation. This effect is bigger with the resonances which have more gluons in their final state because gluons radiate more initial state radiation than quarks. The effect is found at both the generated jet level and the corrected calo jet level. This effect is caused by the initial state radiations merged in the leading jets since they fall into the region where leading jets are reconstructed. Also it can be easily noticed that the effect is bigger when the resonance mass is smaller. The effect is smallest with 0.7 TeV and biggest with 5.0 TeV. This is because the radiation is more frequent at lower parton energies, both because the strong coupling is larger there, and because partons at lower fractional momentum of the proton are created primarily through initial state radiation. Fig.4.2, 4.3, and 4.4 show that the main effect of the initial state radiation is increasing the high mass tail in the dijet mass distribution of the resonance and the effect is larger for the resonance which has more gluon in their final state and higher mass. However, this initial state radiation is not as large an effect as final state radiation which explained in the next section.

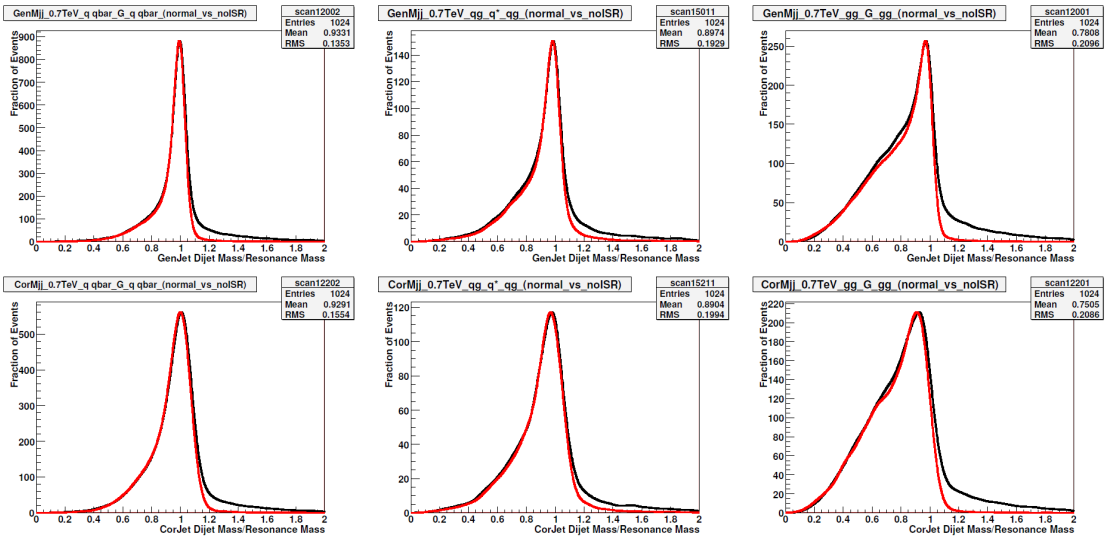

Figure 4.2: Initial state radiation effect for 0.7 *TeV* dijet resonances. x distribution is dijet mass distribution divided by input resonance mass. The left plots are for $q\bar{q} \to G \to q\bar{q}$. The middle plots are for $qg \to q* \to qg$. The right plots are for $gg \to G \to gg$. The red is for the simulation which does not have initial state radiation. The black is for the dataset which include initial state radiation. Top plots are for generated jets. The bottom plots are for corrected calo jets.

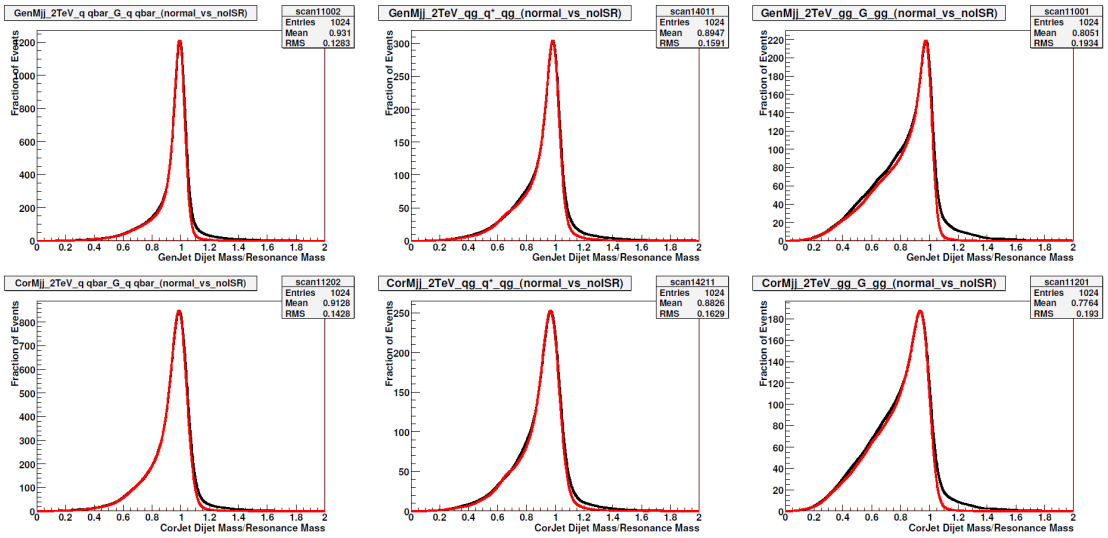

Figure 4.3: Initial state radiation effect for 2.0 *TeV* dijet resonances. x distribution is dijet mass distribution divided by input resonance mass. The left plots are for $q\bar{q} \to G \to q\bar{q}$. The middle plots are for $qg \to q* \to qg$. The right plots are for $gg \to G \to gg$. The red is for the simulation which does not have initial state radiation. The black is for the dataset which include initial state radiation. Top plots are for generated jets. The bottom plots are for corrected calo jets.

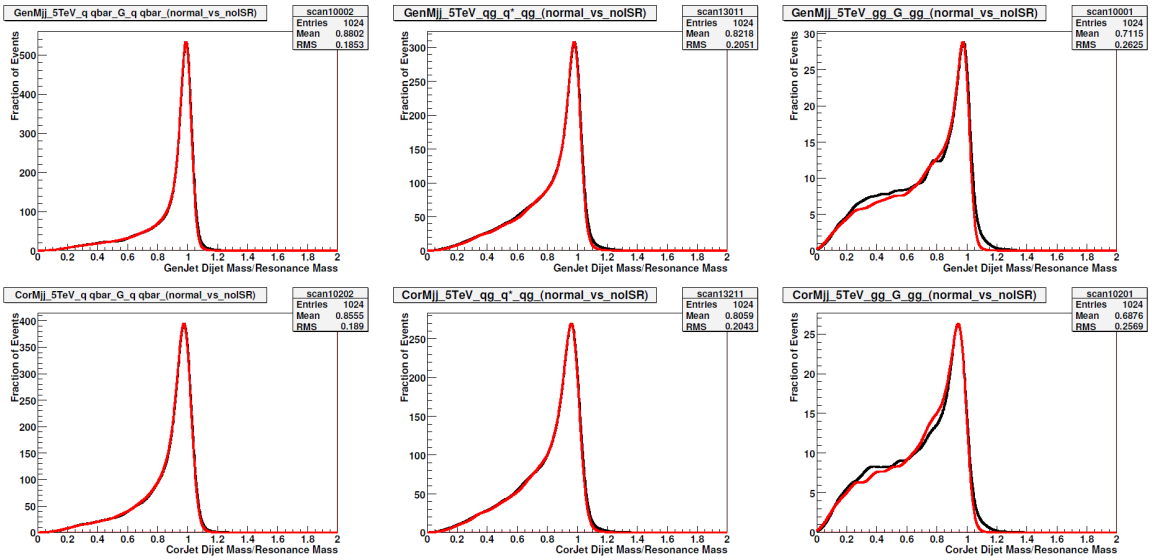

Figure 4.4: Initial state radiation effect for 5.0 *TeV* dijet resonances. x distribution is dijet mass distribution divided by input resonance mass. The left plots are for $q\bar{q} \to G \to q\bar{q}$. The middle plots are for $qg \to q* \to qg$. The right plots are for $gg \to G \to gg$. The red is for the simulation which does not have initial state radiation. The black is for the dataset which include initial state radiation. Top plots are for generated jets. The bottom plots are for corrected calo jets.

4.1.2 Effect of final state radiation

Final state radiation in dijet resonances is the radiation from quarks and gluons after resonance decays, in other words after collisions. If final state radiation falls outside of area of leading jets, this decreases energy of leading jets and dijet mass. The final state radiation affects in two ways in dijet mass distribution. The first is low mass tail and the second is shift of peak position of the dijet mass distribution. The low mass tail is coming from the final state radiation which lost outside the jet cone. Since the final state radiations are not merged into the leading jets, it decreases the energy of leading jets and dijet mass. This increase low dijet mass tail. The shift of the peak position of the dijet mass distribution is little more complicated. Gluons radiate more than quarks so there are more stable particles resulting from hadronization in the parton shower of gluons than quarks. Fig. 4.5 shows the number of final stable particles which used when reconstruct generated jets for 2.0 TeV

resonance. Here we can see that the number of particles in the generated jet is decreased when the final state radiation is turned off(Parton shower is either eliminated or reduced.) as expected. In same manner, leading jets from resonance which have more gluons have more stable particles. This means that each stable particles from gluons have lesser p_T than particles from quarks. Since particles with less momentum have less response and poor resolution in the CMS calorimeter, peak position of dijet mass distribution shifts to lower mass region and the width of the dijet resonance become wider when they have more gluon. We call this the jet fragmentation response effect.

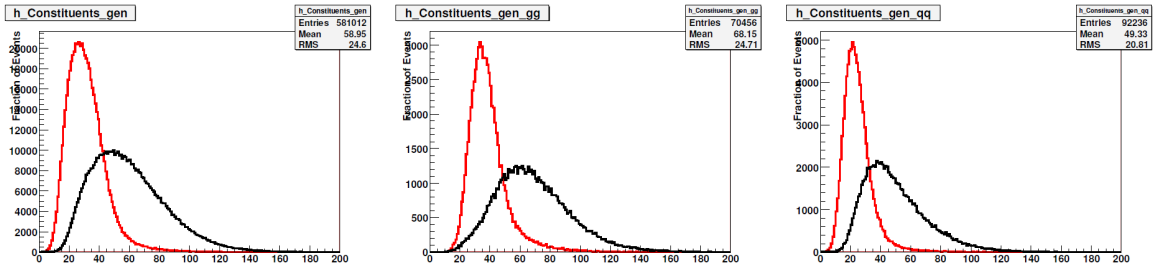

Figure 4.5: Number of particles for GenJets with and without final state radiation. The left plot is for $qg, q\bar{q} \to G \to qg, q\bar{q}$. The middle plot is for $gg \to G \to qg, gg$. The right plot is for $qg, q\bar{q} \to G \to qg, q\bar{q}$. The input resonance mass is 2 TeV.

The simulations without the final state radiation were also prepared to study above effects. Again, turning off the final state radiation is not physical, and MC dependent. However, we turned off the final state radiation to show the effects of the final state radiation. Fig. 4.6 shows the x distribution for 2.0 TeV resonances both with and without final state radiation. From these figures, we can see the effects of the final state radiation. First, the low mass tail of dijet mass distributions is longer with resonances which have the final state radiation compared to resonances which do not have the final state radiation. This happens to both generated jet level and corrected calo jet level. This is because the final state radiation falls outside of the jet area when leading jets are reconstructed and lost. Second, the peak positions of dijet mass distributions of resonances with the final state radiation are at lower mass region than the resonances without the final state radiation. However,

this happens only on corrected calo jet level, because this is the jet fragmentation response effect which occurred with calorimeter response effect. Third, width of the dijet mass distribution of resonance is wider at corrected calo jet level compared to generated jet level. This is again due to the jet fragmentation response effect. Finally,when the final state of resonance has more gluons above effects are increased. This is because that gluons radiate more than quarks.

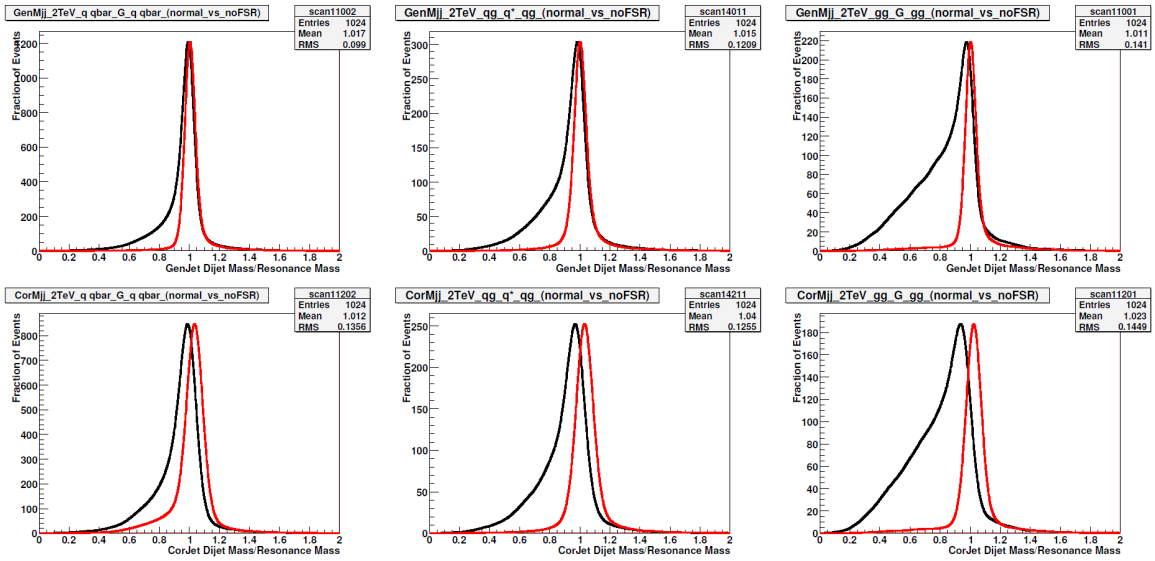

Figure 4.6: Final state radiation effect for 2.0 *TeV* dijet resonances. x distribution is dijet mass distribution divided by input resonance mass. The left plots are for $q\bar{q} \to G \to q\bar{q}$. The middle plots are for $gg \to G \to gg$. The right plots are for $qg \to q* \to qg$. The red is for the simulation which does not have the final state radiation. The black is for the simulation which include the final state radiation. Top plots are for generated jets. The bottom plots are for corrected calo jets.

4.2 The Signal in Anaysis

Fig. 4.7 shows the simulated signal of excited quarks for AK5 calo jets. As we mentioned, resonance shape with resonance mass of $M = 0.5$,0.7, 1.2, 2.0, and 3.5 TeV are made with PYTHIA MC + CMS detector simulation. Simulating all the mass point we are interesting is ideal but it takes time and requires huge computing power and big size of storage which is

not available. So the intermediate masses are obtained by the interpolation technique. First, we defined a new parameter as $x = \frac{M_{jj}}{M_{Res}}$ where M_{jj} is dijet mass and M_{Res} is resonance mass. Now we have x distribution for $M = 0.5$,0.7, 1.2, 2.0 and 3.5 TeV. Then by using following equation we generate the x distribution of any resonance mass between given resonance mass:

$$Prob_M(x) = Prob_{M1}(x) + [Prob_{M2}(x) - Prob_{M1}(x)] \cdot \frac{M - M1}{M2 - M1} \tag{4.1}$$

where M is the resonance mass we are interesting to know; $M1$ and $M2$ are given resonance mass ($M1 < M2$). This is interpolation method. If one wants resonance shape outside given mass for example outside 3.5 TeV, one just need to use $M1 = 2.0$ TeV, $M2 = 3.5$ TeV. This is the extrapolation method and used in this analysis. We use the resonance shapes from both method when we calculate the cross section upper limit at any resonance mass points.

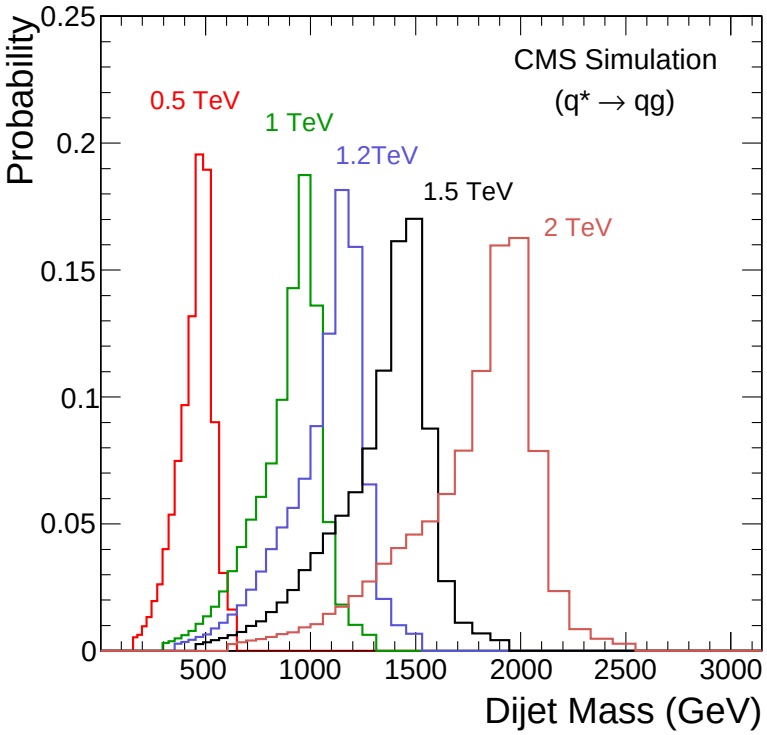

Figure 4.7: qg resonance shapes at various resonance mass coming from excited quark simulation at resonance masses in TeV of 0.5 (red), 0.7 (green), 1.2 (blue), 2.0 (red), and 3.5 (not shown) and interpolation at the example mass of 1.5 TeV (black).

Fig. 4.8 shows the differential cross section of observed dijet mass data as a function of dijet mass with background fit. Fig. 4.8 also shows differential cross section of excited quark and string resonance signal shapes as a function of dijet mass. The string resonance shape in these plot is modeled from excited quark resonance shape since string resonances decay predominantly to a quark and a gluon. The expected string resonance cross section is large as shown in Fig. 4.8. They are even greater than measured data. In Fig. 4.9, the ratio between the data and the fit is presented. Fig. 4.9 also shows how they look if signals for both excited quarks and string resonances exist.

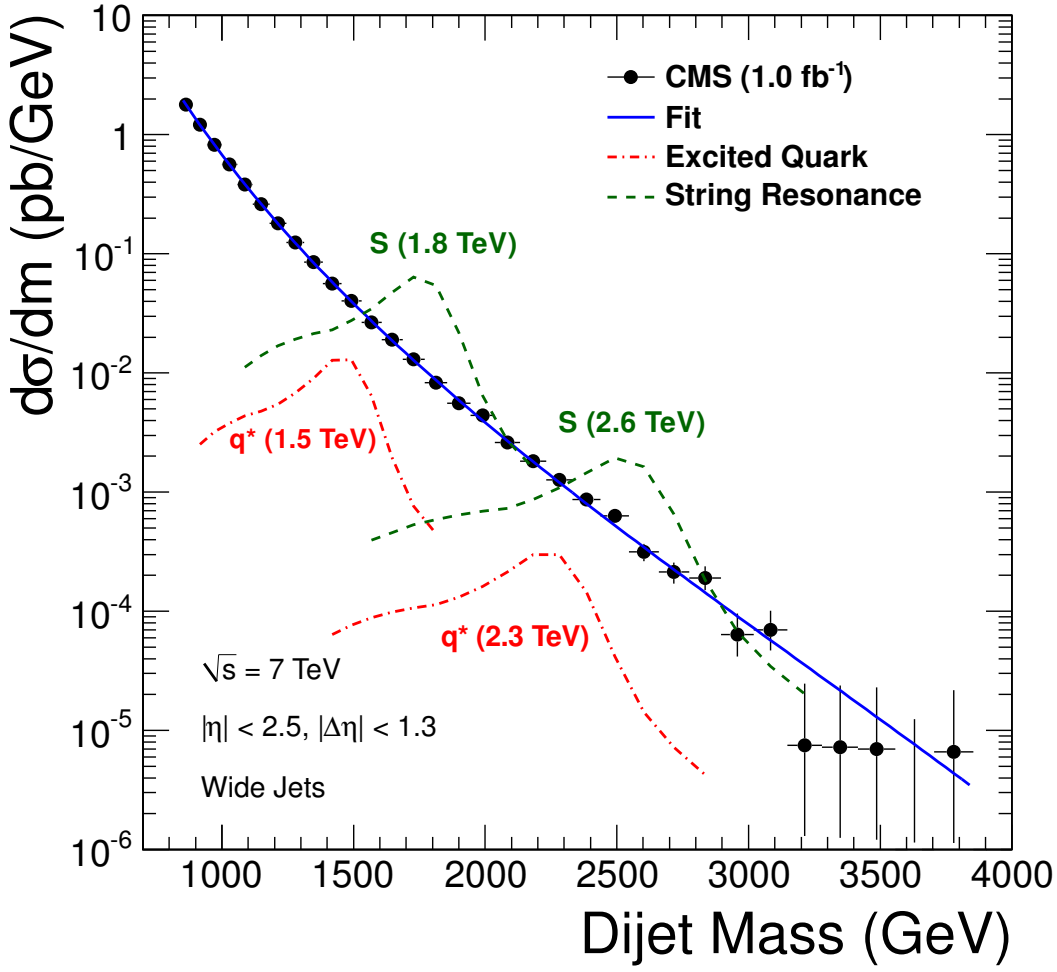

Figure 4.8: The dijet mass distribution for wide jets (points) compared to a smooth background fit (blue solid curve) and to a simulation of excited quarks (red dot-dashed curves) and string resonances (green dashed curves) in CMS detector.

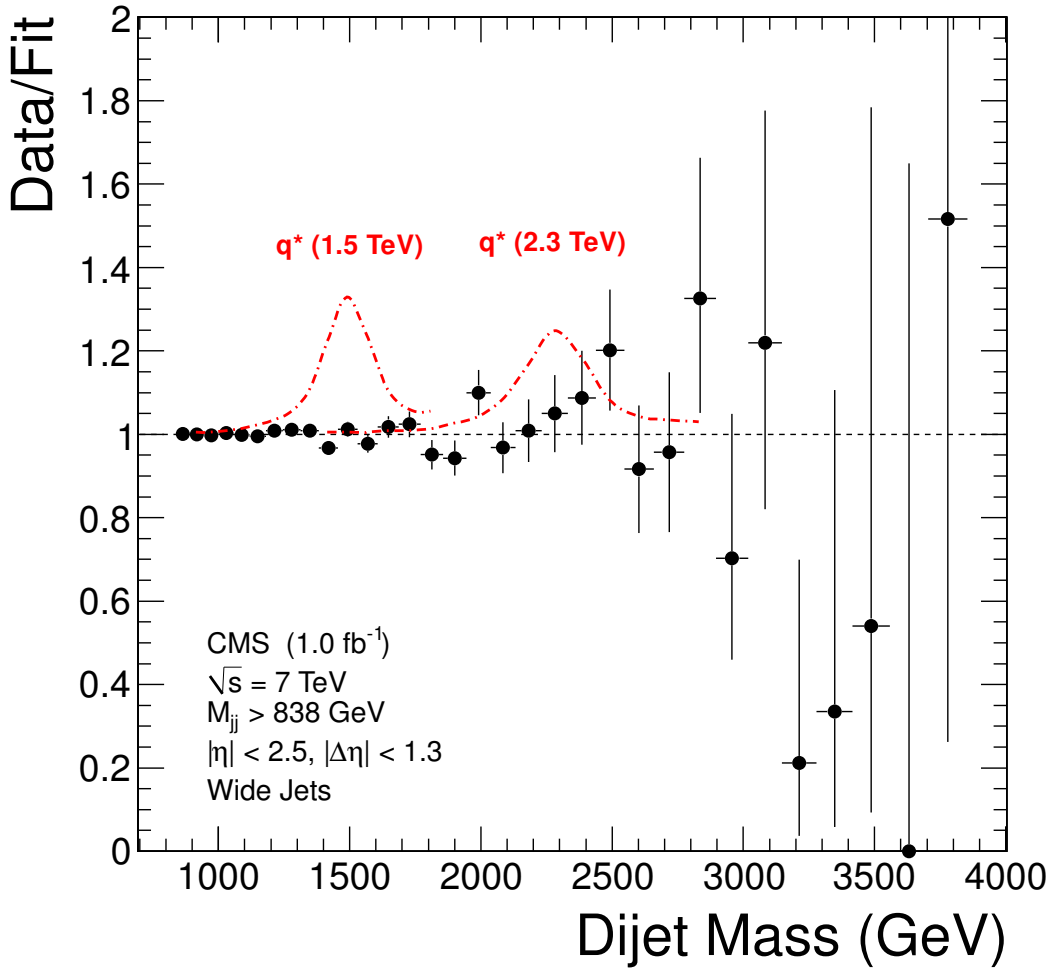

Figure 4.9: The ratio between the dijet mass distribution (points) and a smooth background fit (dashed line) for wide jets is compared to the CMS detector simulation of excited quark signals (dashed red curve).

4.3 Setting Cross Section Upper Limits

Since we do not have strong evidence of existence of new particles, we set upper limits on dijet resonance cross section. We used Bayesian formalism with uniform prior to set the cross section upper limit. The binned likelihood, L, as a function of a constant α can be written as:

$$L = \prod_i \frac{\mu_i^{n_i} e^{-\mu_i}}{n_i!} \tag{4.2}$$

where

$$\mu_i = \alpha N_i(S) + N_i(B); \tag{4.3}$$

n_i is the measured number of events in the i^{th} dijet mass bin; $N_i(S)$ is the number of events from the signal in the i^{th} dijet mass bin; α is a constant to scaling the signal amplitude; and $N_i(B)$ is the number of expected events from background in the i^{th} dijet mass bin. We consider that the QCD background is fixed by the best QCD fit to the data points and the fit gives the expected number of background event in the i^{th} dijet mass bin, $N_i(B)$. The number of signal events in the i^{th} dijet mass bin, $N_i(S)$, comes from resonance shapes given by PYTHIA MC + CMS detector simulation and an interpolation technique. We choose signal mass range to be from $0.3 \cdot M_{Res}$ to $1.3 \cdot M_{Res}$. This mass range covers almost all of the resonance line shape. We set this limitation, because resonance line shape mass below $0.3 \cdot M_{Res}$ is negligible compared to QCD background and greater than $1.3 \cdot M_{Res}$ is model dependent and not so reliable for narrow resonances. We assume a flat prior in α, which is the same as a flat prior in the resonance cross section. With this assumption the likelihood normalized to unity is equivalent to a posterior probability density and can be used to set limits. We calculate the posterior probability density as a function of signal cross section for resonances with mass from 1.0 TeV to 4.1 TeV in 0.1 TeV step. The 95% CL upper limit, σ_{95}, is calculated from the posterior probability density P_{POST} as follows:

$$\frac{\int_0^{\sigma_{95}} P_{POST}(\sigma) d\sigma}{\int_0^{\infty} P_{POST}(\sigma) d\sigma} = 0.95 \tag{4.4}$$

4.4 Limit Setting with Roostat

Roostat [37] is an official statistical tool at CMS. Roostat is built on top of RooFit. [38] We use Roostat to set 95% CL upper limit based on a Bayesian method. First, we fit the data after we fill a histogram with dijet mass values from trigger cut to 5 TeV with bin size 1 GeV. We fit up to 5 TeV so the fit can be used to calculate 95% CL uppper limit up to 4.1 TeV. Once we get the background fit, we follow the process that we described in previous section. Fig. 4.10 shows 95% CL cross section upper limit of dijet resonance times branching ratio (*BR*) times kinematic acceptance (*A*) as a function of dijet mass which are calculated with above method for 32 different mass points in *pb*. Fig. 4.10 includes only statistical uncertainties. 95% CL upper limits are calculated for three different types of resonances which decay to quark-quark, quark-gluon and gluon-gluon. The structure of the plot is reflection of upward and downward fluctuations of the observed data. The limits are also tabulated numerically in table 4.1.

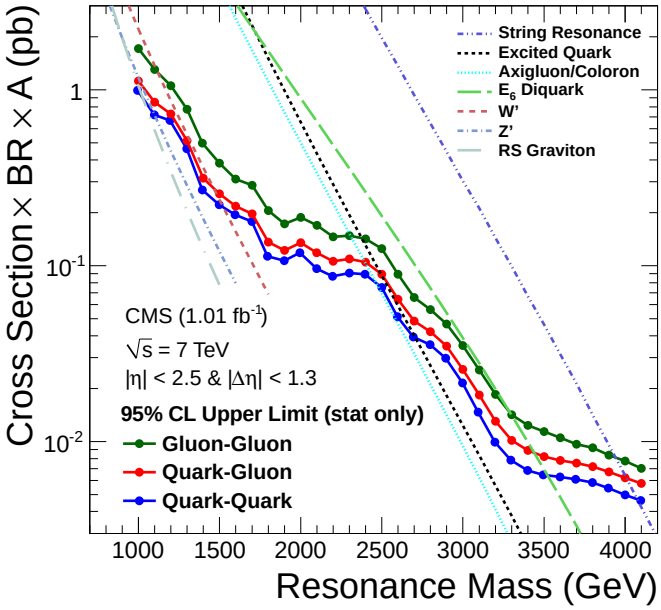

Figure 4.10: Dijet resonance sensitivity with statistical errors only for wide jets. The 95% CL upper limit on cross section is compared to the cross section for various resonance models. This sensitivity does not contain estimates of the systematic uncertainties.

Table 4.1: As a function of resonance mass, we list our 95% CL upper limit on cross section times branching ratio for narrow resonances originating from quark-quark, quark-gluon, and gluon-gluon pairs of partons including statistical errors only for wide jets.

Mass	95% CL $\sigma \cdot B$ (pb) Stat. Err. Only		
(TeV)	quark-quark	quark-gluon	gluon-gluon
1.0	0.98117	1.12380	1.71707
1.1	0.71763	0.85015	1.30642
1.2	0.66727	0.72977	1.05537
1.3	0.46010	0.51269	0.77611
1.4	0.26575	0.31458	0.49823
1.5	0.22164	0.25654	0.38314
1.6	0.19445	0.21768	0.31132
1.7	0.17629	0.19703	0.28691
1.8	0.11266	0.13608	0.20560
1.9	0.10556	0.12224	0.17301
2.0	0.11733	0.13513	0.18825
2.1	0.09512	0.11829	0.16983
2.2	0.08687	0.10578	0.14615
2.3	0.09074	0.10945	0.14813
2.4	0.08861	0.10462	0.14225
2.5	0.07426	0.08945	0.12509
2.6	0.05097	0.06451	0.08956
2.7	0.03893	0.04842	0.06593
2.8	0.03540	0.04219	0.05619
2.9	0.02945	0.03485	0.04653
3.0	0.02126	0.02569	0.03514
3.1	0.01452	0.01840	0.02553
3.2	0.00987	0.01305	0.01857
3.3	0.00774	0.01016	0.01421
3.4	0.00686	0.00892	0.01235
3.5	0.00644	0.00820	0.01139
3.6	0.00623	0.00782	0.01049
3.7	0.00605	0.00753	0.00966
3.8	0.00581	0.00721	0.00923
3.9	0.00540	0.00672	0.00836
4.0	0.00494	0.00621	0.00776
4.1	0.00461	0.00578	0.00704

Chapter 5

Systematic Uncertainties on the Search

There are four sources of systematic uncertainties and they are following:

- JES
- JER
- Background Parametrization
- Luminosity

5.1 Jet Energy Scale

The uncertainty on the JES is the uncertainty which comes from the difference between simulation and data on the JES. If the simulated JES has high response, then the position of simulated resonance will be placed at the higher mass region than it should be placed. The JES uncertainty is only on the simulated signal but the background, since the background is coming from only fit of data in our process. So this uncertainty is the uncertainty about position of simulated resonance signal. 2011 official CMS JES uncertainty is studied and provided with Jet energy correction. We selecte leading jets and calculate JES uncertainty as function of dijet maass. Fig. 5.1 shows the JES uncertainty as a function of dijet mass. This plot shows the JES uncertainty is almost flat at 2.2%.

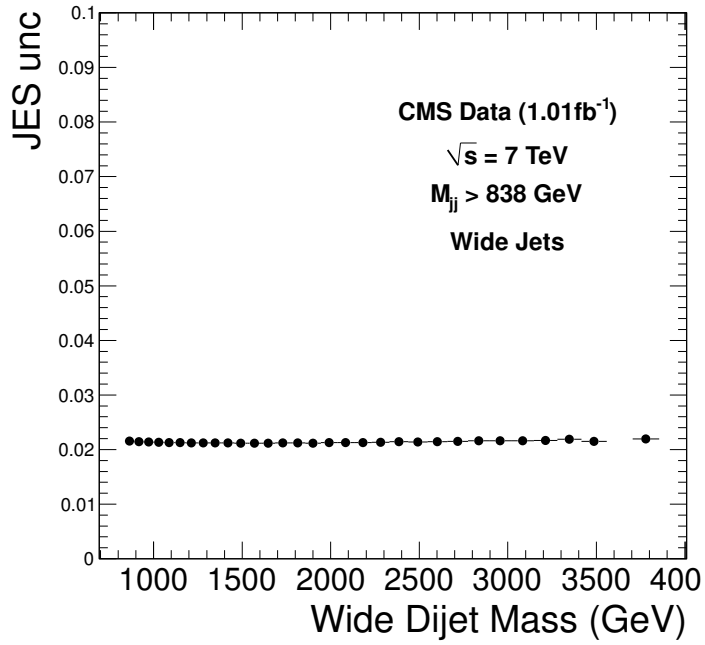

Figure 5.1: JES uncertainty as a function of dijet mass for wide jet.

5.2 Jet Energy Resolution

The uncertainty on the JER is the uncertainty which also comes from the difference between simulation and data on the jet energy resonlution. If the simulated JER is bigger than the JER from data, the width of the simulated resonance is broader than real resonance. The JER uncertainty is only on simulated signal like JES uncertainty. The uncertainty on JER at high dijet mass is $\pm 10\%$. [39] The tails of the resolution function are in good agreement between data and MC. This same dijet asymmetry method with a varying cut on the 3rd jet p_T constrains the differences in radiation between the data and MC, and thereby restricts differences in MC modeling of the resonance shape due to radiation to be small.

5.3 Background Parameterization

For the background parameterization, we vary the fit parameter by 1σ. We vary the three parameters in the fit simultaneously considering their correlation. The parameters are fully

correlated, or fully anti-correlated, so we move them all by 1σ simultaneously with the appropriate sign.

5.4 Luminosity

The uncertainty on the integrated luminosity is 6%.

5.5 Incorporating Systematics in The Limits

The above systematic uncertainties are included in the upper limit calculation as nuisance parameters with fully bayesian method as discussed in the Appendix E. In summary, we integrate over the uncertainties, and nuisance parameters with uniform prior and find find 95% CL upper limit including systematic uncertainties. The likelihood as function of cross section plot can be found in the Appendix F. Fig. 5.2 shows the 95% CL upper limit on cross section times branching ratio times acceptance as a function of dijet mass for statistical uncertainties only and including systematic uncertainties for three resonance types and fractional change in the limit with a break down of the contribution of each systematic for qg resonances only. There are several things we need to talk here. First, the effect of systematic is small. Second, JES uncertainty is dominant systematic uncertainty. Third, JES uncertainty sometimes lower the upper limit. This improving upper limit with JES uncertainty is happened at the resonance mass which is correspond to upward fluctuations for the data above the fit. This is due to the JES uncertainty which moves the resonance signal where there is less indication of a signal in the data. Fourth, the background systematic is the dominant systematic at some resonance mass. Table 5.1 shows that the 95% CL upper limit on cross section times branching ratio times acceptance including systematic uncertainties for resonance with mass from 1.0 TeV to 4.1 TeV in step of 0.1 TeV for three types of resonances.

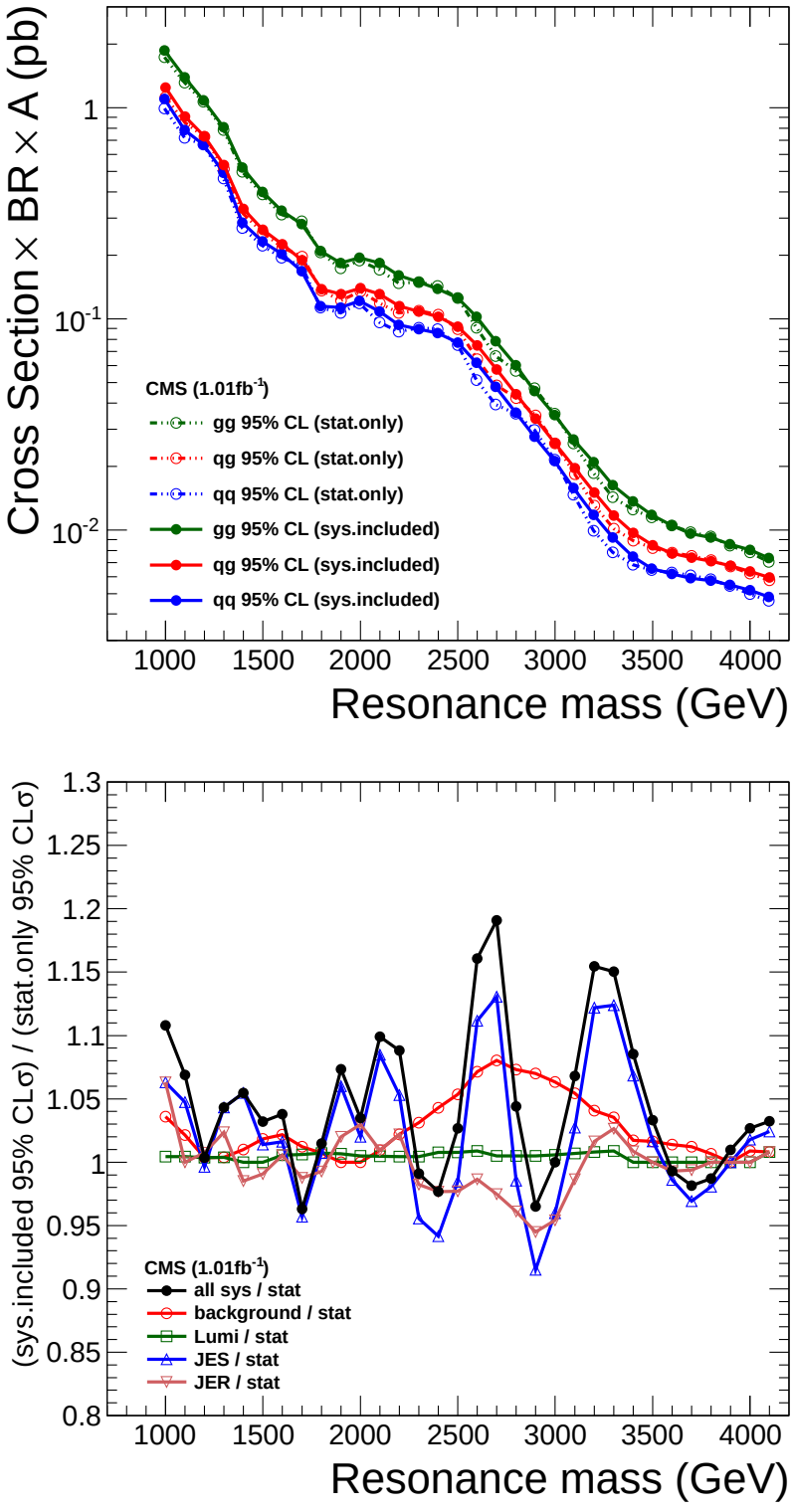

Figure 5.2: Top) Limits on qg resonances with and without all systematic uncertainties for wide jets. Bottom) Fractional change in the limit after including systematics.

Table 5.1: As a function of resonance mass we list our 95% CL upper limit on cross section times branching ratio for narrow resonances originating from quark-quark, quark-gluon and gluon-gluon pairs of partons, including all systematic errors for wide jets.

Mass	95% CL $\sigma \cdot B$ (pb) Stat. Err. Only		
(TeV)	quark-quark	quark-gluon	gluon-gluon
1.0	1.09798	1.24529	1.85078
1.1	0.77656	0.90878	1.37366
1.2	0.66212	0.73244	1.07897
1.3	0.48566	0.53490	0.80296
1.4	0.28418	0.33180	0.51830
1.5	0.23093	0.26478	0.39515
1.6	0.20144	0.22591	0.32564
1.7	0.16784	0.18973	0.28033
1.8	0.11464	0.13806	0.20666
1.9	0.11287	0.13121	0.18334
2.0	0.12136	0.13984	0.19315
2.1	0.10792	0.13001	0.18302
2.2	0.09337	0.11510	0.15953
2.3	0.08928	0.10847	0.14763
2.4	0.08536	0.10217	0.13774
2.5	0.07666	0.09185	0.12474
2.6	0.06192	0.07487	0.10108
2.7	0.04696	0.05766	0.07810
2.8	0.03560	0.04404	0.06010
2.9	0.02736	0.03363	0.04548
3.0	0.02097	0.02569	0.03484
3.1	0.01577	0.01965	0.02678
3.2	0.01178	0.01507	0.02090
3.3	0.00908	0.01169	0.01628
3.4	0.00747	0.00968	0.01364
3.5	0.00651	0.00847	0.01173
3.6	0.00612	0.00776	0.01049
3.7	0.00592	0.00739	0.00957
3.8	0.00571	0.00712	0.00913
3.9	0.00547	0.00678	0.00843
4.0	0.00516	0.00638	0.00799
4.1	0.00480	0.00597	0.00732

Chapter 6

Results

6.1 Results on Dijet Resonance

Wide jets are expected to have the most sensitivity since they collect the final state radiations, and we use wide jets for our result. PF and calo results were used as a check. Since we do not see any evidence of new physics, we set 95% CL limits. The 95% CL limits are set on the cross section times branching ratio for decay to dijets times acceptance for the eta cuts used in this analysis: $|\Delta\eta| < 1.3$ and $|\eta| < 2.5$ for three different parton pairs qq, qg and gg which have different resonance shapes. Since the results of cross section upper limits are generic, they can be used to set mass limits on any model, by comparing the upper limit to the model's cross section with the relevant parton pairs. Here we compared them to 8 models: String, Excited Quarks, Axigluons, Colorons, E_6 diquarks, W', Z', and RS Gravitons. The calculations use CTEQ6L1: parton distributions from CTEQ6L and lowest order values of the strong coupling constant α_S. We can exclude resonance mass points for models with predicted cross sections greater than our 95% CL upper limit on the cross section for the appropriate parton pairs. For string resonances and excited quarks we use our limits on qg resonances to get the mass limits, and for axigluons, colorons and E_6 diquarks, we use our limits on qq resonances to get the mass limits. The ratio between the model cross section and 95% CL upper limit on the cross sections are shown in Fig. 6.1 for the eight models. We exclude resonance masses for which this ratio is greater than 1. These mass limits are presented in Table 6.1.

Table 6.1: 95% CL excluded mass intervals in TeV on dijet resonance models from this analysis with 1.0 fb^{-1}

Model Excluded Regions (TeV)	Excluded mass region
String	1.0 – 4.00
Excited Quark	1.0 – 2.49
E_6 Diquark	1.0 – 3.52
Axigluon/Coloron	1.0 – 2.47
W' Bosons	1.0 – 1.51

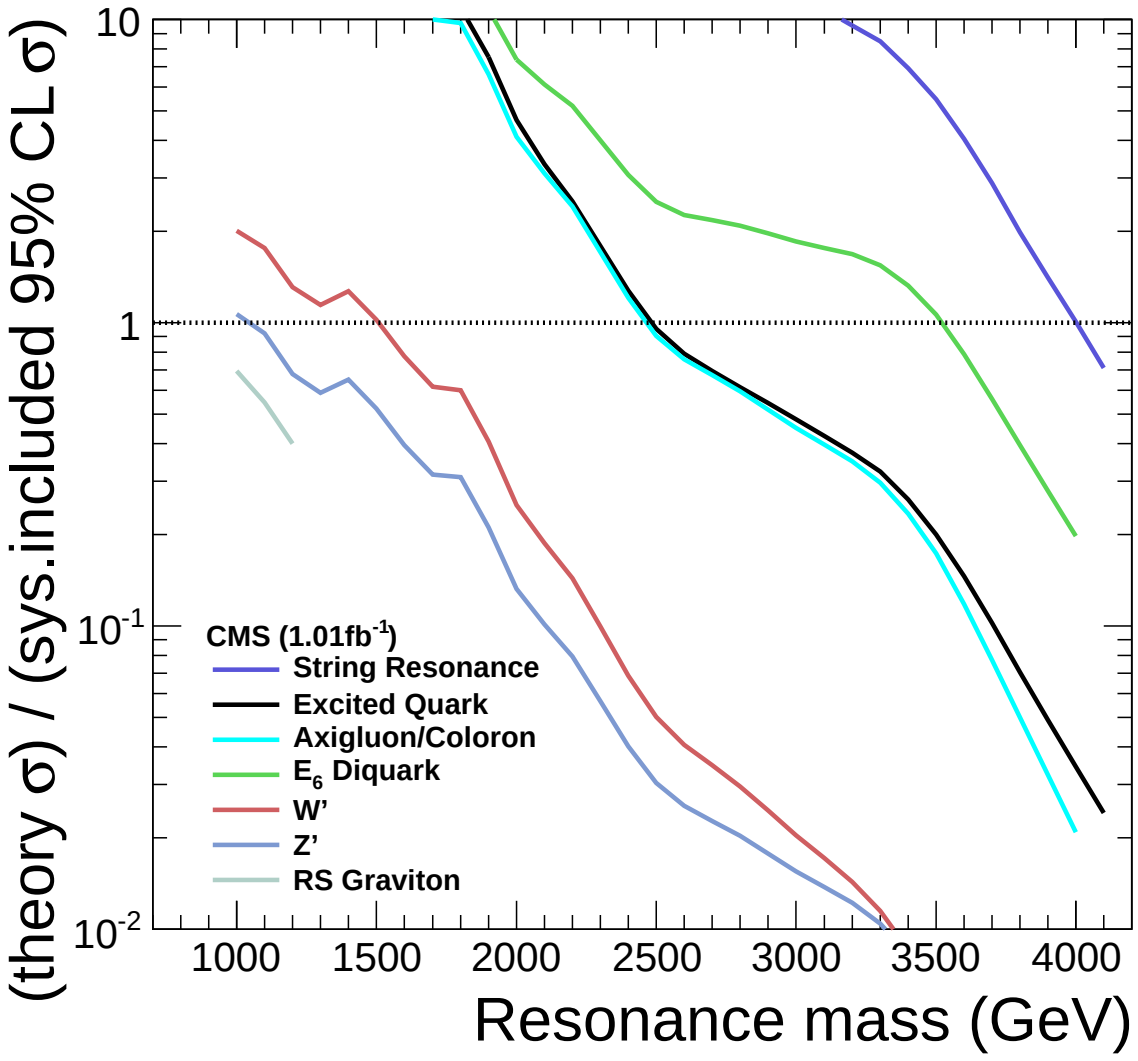

Figure 6.1: The model cross section divided by the 95% CL exclusion upper limits of wide jet result on the cross section for the appropriate parton pairs.

6.2 Expected Limits

Since the result from observed data has structure which reflects the upper and lower fluctuation, we also present the expected limit plot. Expected limit plot shows how the 95% CL upper limit would be without the fluctuation in the data. Fig. 6.2 shows observed 95% CL upper limits on $\sigma\times$ branching ratio $\times$ kinematic acceptance for quark-gluon (left plot) and quark-quark (right plot) dijet resonances (points) compared to the expected limits (dot-dashed) and their expected statistical variation at the 1σ and 2σ levels (shaded bands). In Fig. 6.2 observed 95% CL upper limits are compared to the theoretical predictions for string resonances, excited quarks, axigluons, colorons, E_6 diquarks, W' bosons, Z' bosons and Randal-Sundrum gravitons. We expect excluding mass at 95% CL below 3.90 TeV for string resonances, 2.68 TeV for excited quarks, 2.66 TeV for axigluons and colorons, 3.28 TeV for E_6 diquarks, and 1.40 TeV for W' bosons.

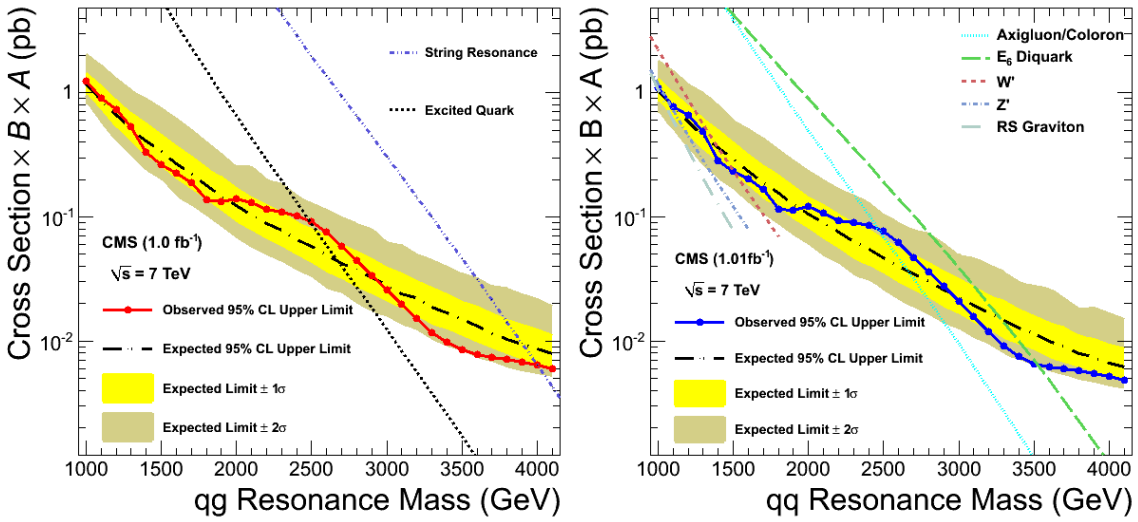

Figure 6.2: Left) Expected limits on qg resonances with all systematic uncertainties for wide jets. Right) Expected limits on qq resonances with all systematic uncertainties for wide jets

Because expected limits does not depend on the fluctuation of the data, we used the expected limit to figure out what is going to be the excluded mass range for the data which

would be taken next year. After 2012 the LHC will have a technical stop for one year, and 15 fb^{-1} of data is expected to be collected before the technical stop. Fig. 6.3 shows the expected limit. With 15 fb^{-1} of data, we expect excluding mass at 95% CL below 3.20 TeV for excited quarks, 3.18 TeV for axigluons and colorons, 3.83 TeV for E_6 diquarks, 2.04 TeV for W' bosons, and 1.74 TeV for Z' bosons.

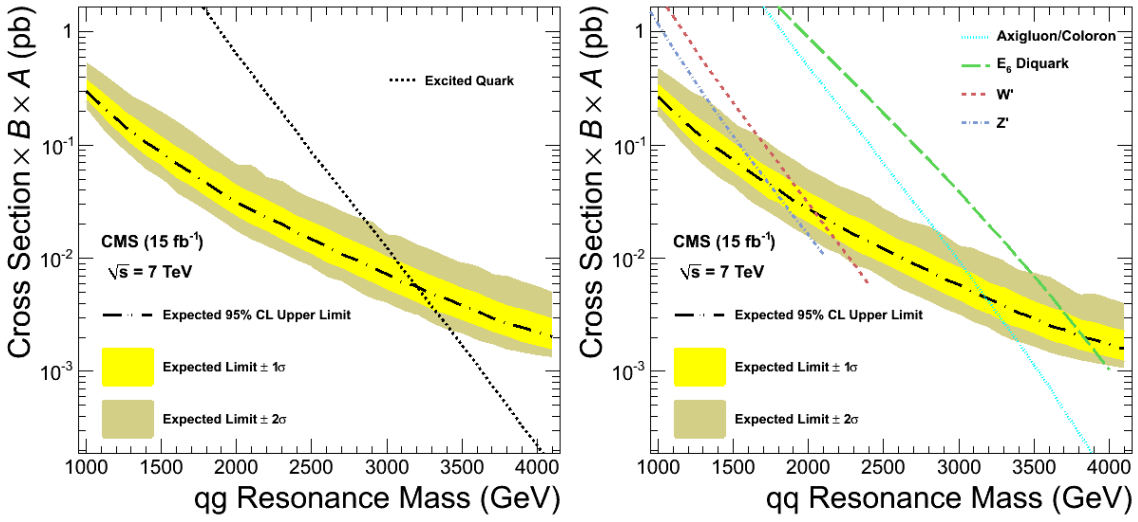

Figure 6.3: Left) Expected limits on qg resonances with all systematic uncertainties for 15 fb^{-1}. Right) Expected limits on qq resonances with all systematic uncertainties for 15 fb^{-1}.

Chapter 7

Conclusions

Simply, this analysis is finding bump on dijet mass spectrum. It measures dijet mass spectrum and compare it to PYTHIA QCD MC simulation result. Then fit the data to check if there is any sign of bump which represents new particle predicted by new physics. If there is no evidence of new particle then we calculate upper limit for several mass points and excludes the mass range for the dijet resonance models. This analysis used 1 fb^{-1} of the CMS data to measure the dijet mass spectrum with the following eta cuts on the two leading jets: $|\Delta\eta| < 1.3$ and $|\eta| < 2.5$. The highest dijet mass is 3.835 TeV. The shape of the measured dijet mass spectrum is in good agreement with a QCD prediction from PYTHIA and the full simulation of the CMS detector. The dijet mass data are well fit by a simple parameterization. There is no significant evidence for new particle production in the data. We set 95% CL upper limits on the cross section for a dijet resonance for three different resonance types: qq, qg, and gg. These types can be used for any narrow resonance decaying to dijet. We compared cross section upper limits with the expected cross sections from several such existing models. Including systematic uncertainties, we exclude at the 95% CL the following models of new particles: string resonances in the mass range $1.0 < M(S) < 4.00$ TeV, excited quarks in the mass range $1.0 < M(q*) < 2.49$ TeV, axigluons and colorons in the mass range $1.0 < M(A) < 2.47$ TeV, E_6 diquarks in the mass range $1.0 < M(D) < 3.52$ TeV, and W' bosons in the mass range $1.0 < M(W') < 1.51$ TeV. Expected excluding mass limit at the 95% CL with data collected next year before the technical stop for an year are below 3.20 TeV for excited quarks, 3.18 TeV for axigluons and colorons, 3.83 TeV for E_6

diquarks, 2.04 TeV for W' bosons, and 1.74 TeV for Z' bosons. This analysis has been published in Phys. Lett. B [40].

Bibliography

[1] R. K. Ellis, W. J. Stirling, B. R. Webber, *QCD and Collider Physics* (Cambridge University Press, 1996)

[2] P.H.Frampton and S.L.Glashow, Phys. Lett. B 190, 157 (1987)

[3] G. Katssilieris, O. Korakianitis, S.D.P. Vlassopulos, Phys. Lett. B 288, 221 (1992)

[4] R.S. Chivukula, A.G. Cohen, and E.H. Simmons, Phys. Lett. B 380, 92 (1996)

[5] Elizarbeth H. Simmons, Phys. Rev. D 55, 3 (1997)

[6] Michael B. Green, and John H. Schwarz, Phys. Lett. B 149, 117 (1984)

[7] JoAnne L. HEWETT, and Thomas G. Rzzo, Physics Report Vol. 183, 193 (1989)

[8] P. Cakir, and R.Mehdiyev, Phys. Rev. D 60, 034004 (1999)

[9] E. Eichten, I. Hinchliffe, K. Lane, C. Quigg, Rev. Mod. Phys. 56, 579 (1984)

[10] Lisa Randll, and Raman Sundrum, Phys. Rev. Lett. 83, 3370 (1999)

[11] Kazim Gumus, Nural Akchurin, Selda Esen and Robert Harris, CMS-AN-2006/070

[12] J. Bijnens, P. Eerola, M. Maul, A. Mansson, T. Sjostrand, Phys. Lett. B 503, 341 (2001)

[13] Luis A. Anchordoqui, Haim Goldberg, Dieter Lust, Satoshi Nawata, Stephan Stieberger, and Tomasz R. Taylor, Phys. Rev. Lett. 101, 241803 (2008)

[14] Schuyler Cullen, Maxim Perelstein and Micheal E. Peskin, Phys. Rev. D. 62, 055012 (2000)

[15] Gabriele Veneziano, Nuovo Climento A. 57, 190 (1968)

[16] *http://lhc-machine-outreach.web.cern.ch/lhc-machine-outreach/lhc_in_pictures.htm*

[17] Br§ning, Oliver Sim, Collier, Paul, Lebrun, P, Myers, Stephen, Ostojic, Ranko, Poole, John, Proudlock, Paul, *LHC Design Report*, (CERN, 2004)

[18] The CMS Collaboration *The CMS experiment at the CERN LHC*, Journal of Instrumentation, 3, S08004 (2008)

[19] *http://uscms.fnal.gov/uscms/picturearchive/picturearchive.html*

[20] CMS Collaboration, *The Tracker Project Technical Design Report* CERN/LHCC 1998-006 (1998)

[21] S. Argiro, *Proceedings of the topical workshop on electronics for particle physics TWEPP-07*, (CERN, 2007) p. 105

[22] CMS Collaboration, *The Hadron Calorimeter Project: Technical Design Report* (CERN, 1998)

[23] CMS Collaboration, *The CMS Muon Project: Technical Design Report* (CERN, 1997)

[24] CMS Collaboration, *The Magnet Project: Technical Design Report* (CERN, 1997)

[25] CMS Collaboration, *Level-1 Trigger: Technical Design Report* (CERN, 2008)

[26] CMS Collaboration, *CMS trigger and data-acquisition project: Technical Design Report* (CERN, 2002)

[27] The CMS Collaboration, *Jet Performance in pp Collisions at* $\sqrt{s}$ *= 7 TeV* CMS PAS JME-10-003

[28] Konstantinos Kousouris, *Measurement of the Relative Jet Energy Scale in CMS with pp Collisions at* $\sqrt{s}$ *= 7 TeV* CMS-AN-2010/139

[29] The CMS Collaboration, *Search for Heavy Particles Decaying to Hadronic Final States With Fat Jet Reconstructionl* CMS-AN-2011/242

[30] The ATLAS Collaboration, Phys. Rev. Lett. 105, 161801 (2010)

[31] Robert Harris, *Cuts for Dijet Resonance Search*, Presentation at the July 29, 2010 Exotica Multijets Meeting

[32] The CMS Collaboration, *Determination of the Jet Energy Scale in CMS with pp Collisions at* $\sqrt{s}$ *= 7 TeV* CMS PAS JME-10-010

[33] CDF Collaboration, Phys. Rev. D 79, 112002 (2009)

[34] CDF Collaboration, Phys. Rev. Lett. 74 3538 (1995)

[35] CDF Collaboration, Phys. Rev. D55 5263 (1997)

[36] T.Sjostrand, S.Mrenna, P.Skands, J. High Energy Phys. 05, 026 (2006)

[37] L. Moneta, K. Belasco, K. Cranmer, S. Kreiss, A. Lazzaro, D. Piparo, G. Schott, W. Verkerke, M. Wolf, in *The RooStats project*, proceedings of the 13th International Workshop on Advanced Computing and Analysis Techniques in Physics Research, Jaipur, India, 2010, edited by L.Moneta (unpublished)

[38] W. Verkerke, D. Kirkby, in *The RooFit toolkit for data modeling*, proceedings of the 2003 Computing in High Energy and Nuclear Physics, La Jolla, California, 2003, edited by W. Verkerke (unpublished)

[39] The CMS Collaboration, *Jet Resolution Determination at* $\sqrt{s}$ *= 7 TeV* CMS PAS JME-10-014

[40] CMS Collaboration, Phys. Lett. B, 704, 123 (2011)

[41] B. Cousins, *Lognormal and Gamma distribution instead of truncated Gaussian for pdf of positive nuisance parameter.* CMS Twiki Statistics Questions and Answers (http://www.physics.ucla.edu/ cousins/stats/cousins_lognormal_prior.pdf)

[42] The CMS Collaboration, Phys. Rev. Lett. 105, 211801(2010)

Appendix A

The matrix elements for String

$$
\begin{aligned}
\mathscr{M}(g_a^{\pm} g_b^{\pm} \to g_c^{\pm} g_d^{\pm}) &= g^2 \frac{s^2}{stu}[2sV(t,u)\mathbf{P_{27}}_{cd}^{ab} + 3(tV(s,u) - uV(s,t))\mathbf{P_{8_A}}_{cd}^{ab} \\
&\quad + \frac{5}{3}(tV(s,u) + uV(s,t) - \frac{4}{5}sV(t,u))\mathbf{P_{8_S}}_{cd}^{ab} \\
&\quad + \frac{16}{3}(tV(s,u) + uV(s,t) - \frac{1}{8}sV(t,u))\mathbf{P_1}_{cd}^{ab}] \qquad \text{(A.1)} \\
\mathscr{M}(g_a^{\pm} g_b^{\mp} \to g_c^{\pm} g_d^{\mp}) &= g^2 \frac{u^2}{stu}[2sV(t,u)\mathbf{P_{27}}_{cd}^{ab} + 3(tV(s,u) - uV(s,t))\mathbf{P_{8_A}}_{cd}^{ab} \\
&\quad + \frac{5}{3}(tV(s,u) + uV(s,t) - \frac{4}{5}sV(t,u))\mathbf{P_{8_S}}_{cd}^{ab} \\
&\quad + \frac{16}{3}(tV(s,u) + uV(s,t) - \frac{1}{8}sV(t,u))\mathbf{P_1}_{cd}^{ab}] \qquad \text{(A.2)} \\
\mathscr{M}(g_a^{\mp} g_b^{\pm} \to g_c^{\mp} g_d^{\pm}) &= g^2 \frac{t^2}{stu}[2sV(t,u)\mathbf{P_{27}}_{cd}^{ab} + 3(tV(s,u) - uV(s,t))\mathbf{P_{8_A}}_{cd}^{ab} \\
&\quad + \frac{5}{3}(tV(s,u) + uV(s,t) - \frac{4}{5}sV(t,u))\mathbf{P_{8_S}}_{cd}^{ab} \\
&\quad + \frac{16}{3}(tV(s,u) + uV(s,t) - \frac{1}{8}sV(t,u))\mathbf{P_1}_{cd}^{ab}] \qquad \text{(A.3)} \\
\mathscr{M}(g_a^{\pm} g_b^{\mp} \to \bar{q}_{\bar{i}}^{\mp} q_j^{\pm}) &= g^2 \frac{u}{s}[(\sqrt{\frac{u}{t}}V(s,t) + \sqrt{\frac{t}{u}}V(s,u))(\sqrt{\frac{5}{6}}\mathbf{P_{8_S}}_{\bar{i}j}^{ab} + \sqrt{\frac{8}{3}}\mathbf{P_1}^{ab}{}_{\bar{i}j}) \\
&\quad + (\sqrt{\frac{u}{t}}V(s,t) - \sqrt{\frac{t}{u}}V(s,u))\sqrt{\frac{3}{2}}\mathbf{P_{8_A}}_{\bar{i}j}^{ab}] \qquad \text{(A.4)} \\
\mathscr{M}(g_a^{\pm} g_b^{\mp} \to \bar{q}_{\bar{i}}^{\pm} q_j^{\mp}) &= g^2 \frac{t}{s}[(\sqrt{\frac{u}{t}}V(s,t) + \sqrt{\frac{t}{u}}V(s,u))(\sqrt{\frac{5}{6}}\mathbf{P_{8_S}}_{\bar{i}j}^{ab} + \sqrt{\frac{8}{3}}\mathbf{P_1}_{\bar{i}j}^{ab}) \\
&\quad + (\sqrt{\frac{u}{t}}V(s,t) - \sqrt{\frac{t}{u}}V(s,u))\sqrt{\frac{3}{2}}\mathbf{P_{8_A}}_{\bar{i}j}^{ab}] \qquad \text{(A.5)} \\
\mathscr{M}(q_i^{\pm} g_a^{\pm} \to q_j^{\pm} g_b^{\pm}) &= g^2 \frac{s}{t}[\sqrt{-\frac{u}{s}}V(s,t)(\mathbf{P_{15}}_{bj}^{ai} - \mathbf{P_{\bar{6}}}_{bj}^{ai})
\end{aligned}
$$

$$-\frac{1}{3}(\sqrt{-\frac{u}{s}}V(s,t)+8\sqrt{-\frac{s}{u}}V(t,u))\mathbf{P_3}^{ai}_{bj}] \quad \text{(A.6)}$$

$$\mathscr{M}(q_i^{\pm}g_a^{\mp}\to q_j^{\pm}g_b^{\mp}) = g^2\frac{u}{t}[\sqrt{-\frac{u}{s}}V(s,t)(\mathbf{P_{15}}^{ai}_{bj}-\mathbf{P_{\bar{6}}}^{ai}_{bj})$$
$$-\frac{1}{3}(\sqrt{-\frac{u}{s}}V(s,t)+8\sqrt{-\frac{s}{u}}V(t,u))\mathbf{P_3}^{ai}_{bj}] \quad \text{(A.7)}$$

$$\mathscr{M}(q_i^{\pm}\bar{q}_{\bar{j}}^{\mp}\to q_k^{\pm}\bar{q}_{\bar{l}}^{\mp}) = g^2[(\frac{u}{s}-\frac{u}{3t})\mathbf{P_8}^{i\bar{j}}_{k\bar{l}}+\frac{8u}{3t}\mathbf{P_1}^{i\bar{j}}_{k\bar{l}}]V(s,t) \quad \text{(A.8)}$$

where the $\mathbf{P}^{\alpha\beta}_{\gamma\delta}$ tensors are projection between irreducible $SU(3)_C$ representations in the initial and final states.

Appendix B

Binning and Data Table

The lower edges of the dijet mass bins, in GeV, are 1, 3, 6, 10, 16, 23, 31, 40, 50, 61, 74, 88, 103, 119, 137, 156, 176, 197, 220, 244, 270, 296, 325, 354, 386, 419, 453, 489, 526, 565, 606, 649, 693, 740, 788, 838, 890, 944, 1000, 1058, 1118, 1181, 1246, 1313, 1383, 1455, 1530, 1607, 1687, 1770, 1856, 1945, 2037, 2132, 2231, 2332, 2438, 2546, 2659, 2775, 2895, 3019, 3147, 3279, 3416, 3558, 3704, 3854, 4010. Table B.1 shows the data observed with this binning above our dijet mass cut for full trigger efficiency.

Table B.1: For each bin of dijet mass data we list the lower bin edge, the bin width, the number of events, the observed differential cross section, and an estimate of the statistical uncertainty from Gaussian statistics for wide jets.

Low Edge (GeV)	Bin Width (GeV)	Evts	$d\sigma/dm$ ($\frac{pb}{GeV}$)	Stat. Err. ($\frac{pb}{GeV}$)
740	48	0	0	0
788	50	0	0	0
838	52	93739	1.78482	0.00582956
890	54	65901	1.20831	0.00470686
944	56	46340	0.819307	0.003806
1000	58	32902	0.561659	0.00309643
1058	60	23185	0.382591	0.00251264
1118	63	16613	0.261088	0.00202564
1181	65	11879	0.180944	0.00166018
1246	67	8422	0.124457	0.00135616
1313	70	6022	0.0851768	0.00109762
1383	72	4076	0.0560506	0.000877937
1455	75	3047	0.0402244	0.000728708
1530	77	2071	0.0266298	0.000585164
1607	80	1536	0.0190099	0.000485047
1687	83	1095	0.0130621	0.000394737
1770	86	718	0.00826618	0.000308491
1856	89	500	0.00556235	0.000248756
1945	92	408	0.00439087	0.000217381
2037	95	250	0.00260552	0.000164788
2132	99	182	0.00182018	0.000134921
2231	101	129	0.00126458	0.00011134
2332	106	93	0.000868672	9.00771e-05
2438	108	69	0.000632563	7.61517e-05
2546	113	36	0.00031543	5.25716e-05
2659	116	25	0.000213383	4.26767e-05
2775	120	23	0.000189769	3.95696e-05
2895	124	8	6.38774e-05	2.25841e-05
3019	128	9	6.96163e-05	2.32054e-05
3147	132	1	7.50075e-06	7.50075e-06
3279	137	1	7.227e-06	7.227e-06
3416	142	1	6.97253e-06	6.97253e-06
3558	146	0	0	0
3704	150	1	6.60066e-06	6.60066e-06
3854	156	0	0	0
4010	161	0	0	0

Appendix C

Event Displays and Table of High Mass Dijet Events

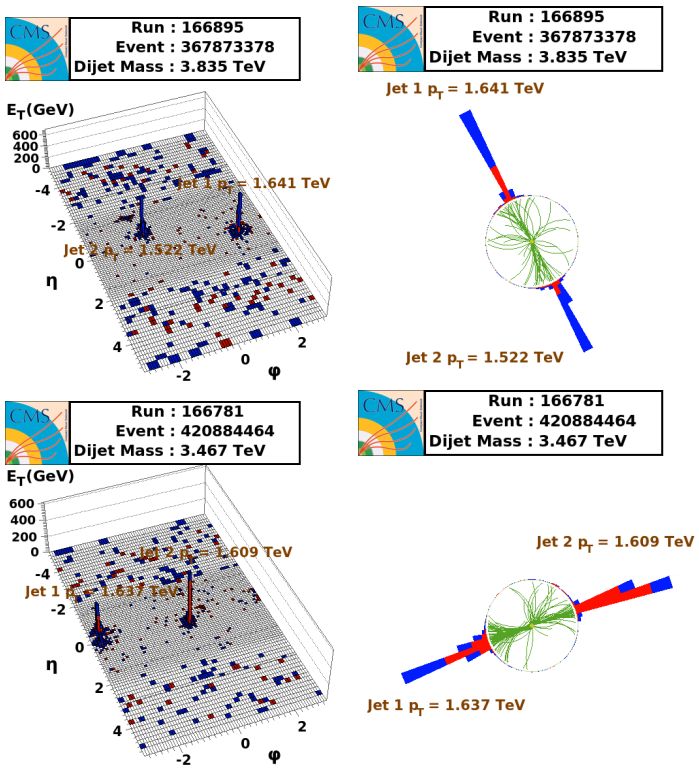

Figure C.1: Lego (left) and $\rho - \phi$ (right) displays of the 1st to 2nd Highest Masss Dijet Events

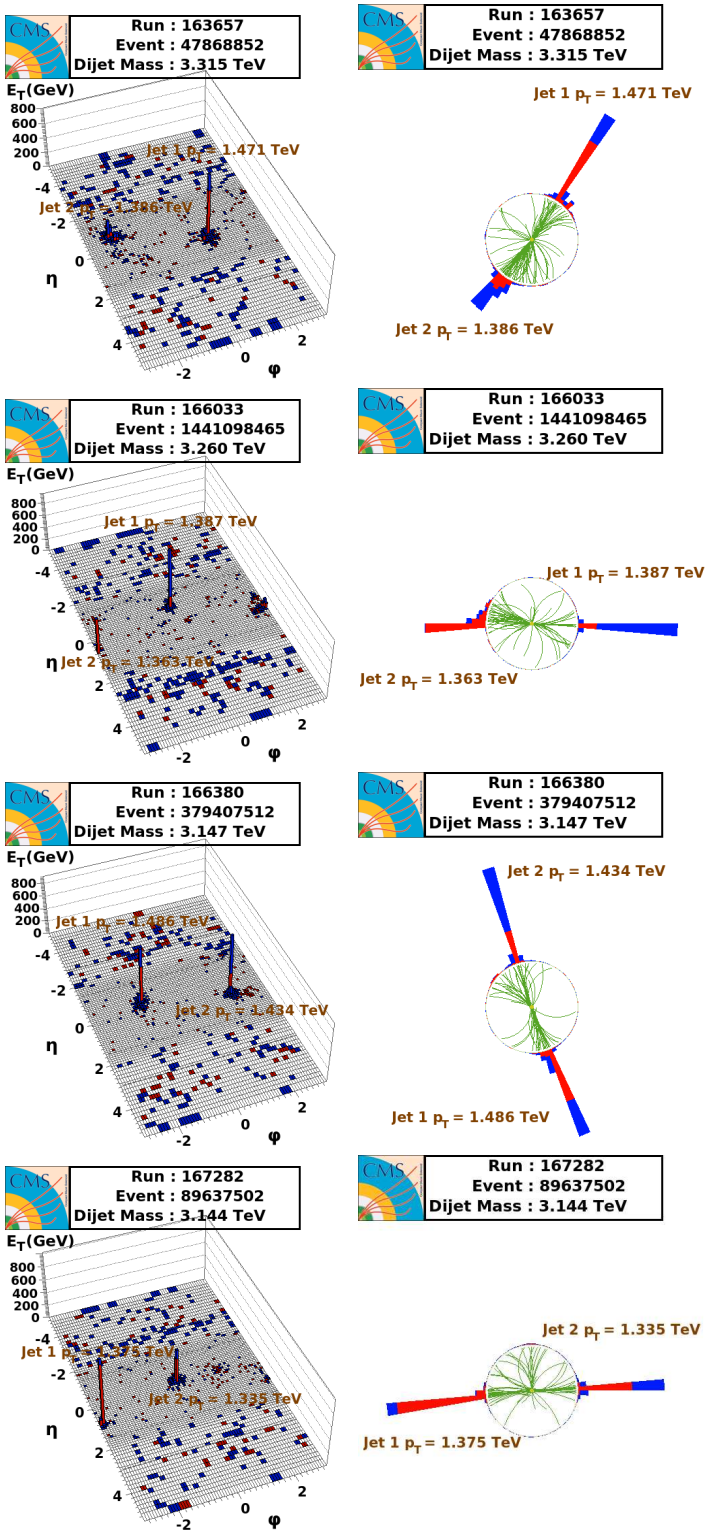

Figure C.2: Lego (left) and $\rho - \phi$ (right) displays of the 3rd to 6th Highest Masss Dijet Events

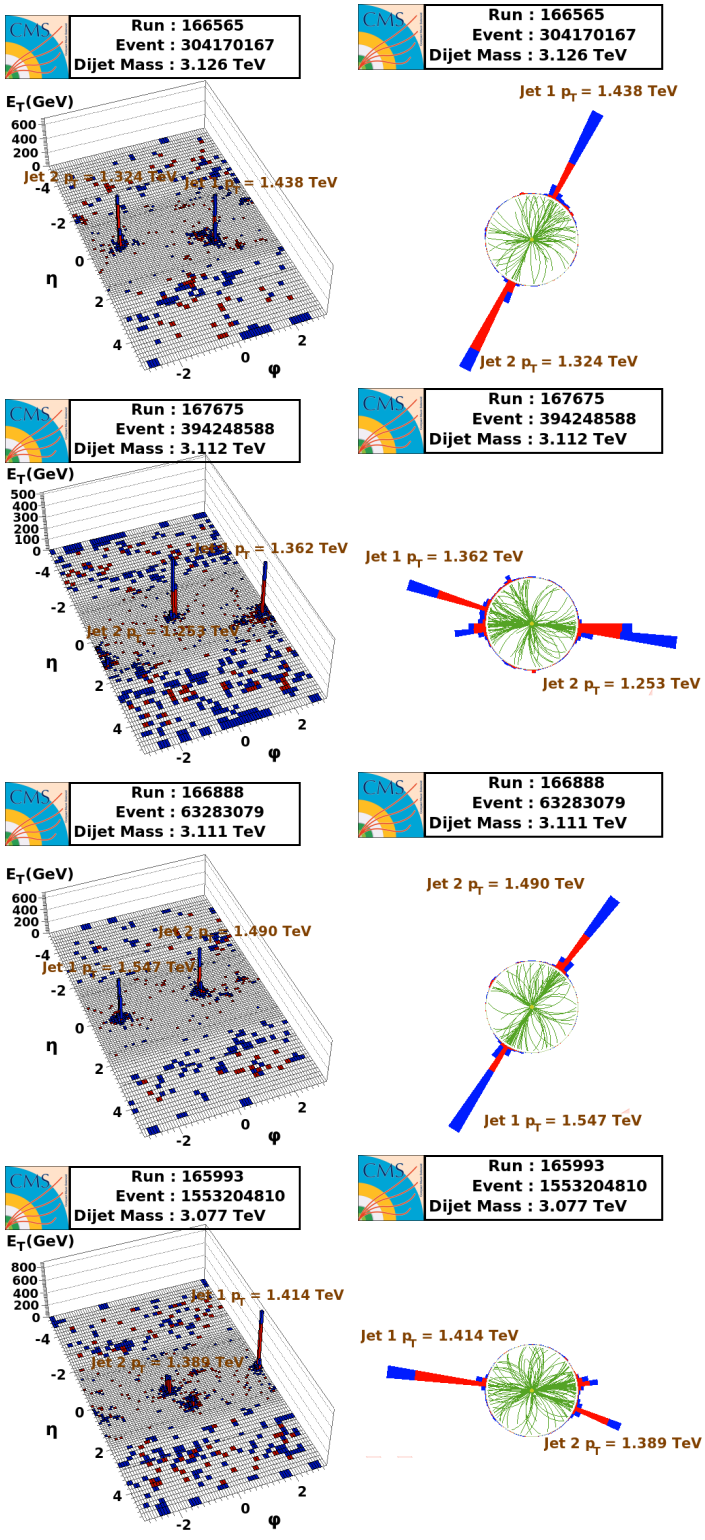

Figure C.3: Lego (left) and $\rho - \phi$ (right) displays of the 7th to 10th Highest Masss Dijet Events

Table C.1: Dijet properties for 10 highest mass events for wide jet (Leading jets corrected p_T, η, ϕ, corrected Dijet Mass, and Missing ET/Sum ET).

Run	*Event*	Dijet Mass (TeV)	*Jet* 1 Cor p_T (TeV)	*Jet* 1 η	*Jet* 1 ϕ	*Jet* 2 Cor p_T (TeV)	*Jet* 2 η	*Jet* 2 ϕ	MET/ΣE_T
166895	367873378	3.835	1.641	0.54	2.05	1.522	-0.71	-1.10	0.04
166781	420884464	3.467	1.637	-0.31	-2.77	1.609	0.26	0.37	0.01
163657	47868852	3.315	1.471	0.35	0.97	1.386	-0.69	-2.23	0.03
166033	1441098465	3.260	1.387	-0.65	-0.05	1.363	0.51	3.08	0.01
166380	379407512	3.147	1.486	-0.49	-1.22	1.434	0.24	1.92	0.00
166565	304170167	3.126	1.438	0.68	1.07	1.324	-0.27	-2.02	0.03
167282	89637502	3.144	1.375	0.82	-3.03	1.335	-0.29	0.04	0.01
167675	394248588	3.112	1.362	0.96	2.93	1.253	-0.13	-0.14	0.02
166888	63283079	3.111	1.547	0.11	-2.14	1.490	-0.21	0.94	0.02
165993	1553204810	3.077	1.414	0.16	3.01	1.389	0.51	-0.16	0.01

Appendix D

Statistical Model

D.1 Introduction

This section is made by Bob Cousins. He made a short informal note about how we need to deal with systematic uncertainties. All the following are from that note.

In this note we attempt to describe the precise mathematical procedure to treat the systematic uncertainties in the search for dijet resonances, within the context of the Bayesian formalism. First we define the parameters that will be used. Then we write the likelihood function in terms of the quantity of interest and the nuisance parameters. Finally we provide the prior pdfs for the latter.

D.2 Definitions

- m: the observed dijet mass.
- M^*: the theoretical resonance mass.
- m_0: the peak position of the resonance shape pdf.
- $m_{l,k}, m_{h,k}$: low and high mass bin boundaries.
- α: the signal strength.
- $\mathscr{L}$: the integrated luminosity nuisance parameter.

- $\mathscr{L}_0$: the best estimate of the integrated luminosity.
- L: the likelihood function.
- L': the marginalized likelihood function (after integrating the nuisance parameters).
- Δ_m: the nuisance parameter related to the JES.
- Δ_σ: the nuisance parameter related to the JER.
- $\mathscr{S}'$: the resonance shape pdf as a function of the observed mass.
- $\mathscr{S}$: the resonance shape pdf as a function of the true mass.
- $\mathscr{B}$: the nuisance parameter $\frac{1}{\mathscr{L}_0}\frac{dN}{dm}$.
- $\mathscr{B}_0$: the best fit of $\frac{1}{\mathscr{L}_0}\frac{dN}{dm}$.
- $N_k(S)$: the number of signal events in the k bin.
- $N_k(B)$: the number of background events in the k bin.
- $f_{\mathscr{L}}$: the fractional uncertainty for the luminosity.
- f_m: the fractional uncertainty for the JES.
- f_σ: the fractional uncertainty for the JER.
- $f_{\mathscr{B}}(m)$: the fractional uncertainty for the background (mass dependent).

D.3 Likelihood Function

We define the binned likelihood function as the product of the Poisson probabilities in each bin, with n_k observed events and μ_k expected events.

$$L(m|a,\vec{\Delta}) = \prod_k \frac{\mu_k(a,\vec{\Delta})^{n_k} e^{-\mu_k(a,\vec{\Delta})}}{n_k!} \tag{D.1}$$

The likelihood function is defined in terms of the variable of interest a which is interpreted as the cross-section of the resonance. In addition, the likelihood function depends on the nuisance parameters $\vec{\Delta} = (\mathscr{L}, \Delta_m, \Delta_\sigma, \mathscr{B})$. The parameters a and $\vec{\Delta}$ enter through the mean number of events μ_k:

$$\mu_k(a, \vec{\Delta}) = N_k(S) + N_k(B) \tag{D.2}$$

where the signal and background number of events are calculated by integrating the corresponding continuous functions across each mass bin:

$$N_k(S) = \mathscr{L} \cdot a \cdot \int_{m_{l,k}}^{m_{h,k}} \mathscr{S}'(m, \Delta_m, \Delta_\sigma)\, dm \tag{D.3}$$

$$N_k(B) = \mathscr{L} \cdot \int_{m_{l,k}}^{m_{h,k}} \mathscr{B}(m)\, dm \tag{D.4}$$

The observed resonance shape is related to the true resonance shape through a mass variable transformation:

$$\mathscr{S}'(m, \Delta_m, \Delta_\sigma) = \mathscr{S}\left(\Delta_m \cdot [\Delta_\sigma \cdot (m - m_0) + m_0]\right) \tag{D.5}$$

The motivation for this transformation is to perform a simultaneous shift in the position and the width of the resonance shape. Although this likelihood function may be refined in the future, we believe that is captures most of the essence of the measurement model, and it is a good starting point for implementing the model in RooStats, exercising the code and getting the first results to compare with our expectations.

D.4 Marginalized Likelihood Function

In order to set limits on the unknown parameter a, the likelihood function needs to be integrated over the nuisance parameters (marginalization). The integration is formally expressed as:

$$L'(m|a) = \int L(m|a; \vec{\delta}) \cdot \pi(\vec{\delta})\, d^4\vec{\delta} \tag{D.6}$$

where $\pi(\vec{\delta})$ is the pdf of the nuisance parameters. We assume that the pdf is factorizable (uncorrelated nuisance parameters) $\pi(\vec{\delta}) = \pi(\Delta_m) \cdot \pi(\Delta_\sigma) \cdot \pi(\mathscr{B}) \cdot \pi(\mathscr{L})$ and is described by a Gaussian distribution, with mean equal to zero and sigma equal to the corresponding uncertainty.

D.4.1 Nuisance Parameters' Prior PDF

The probability densities for the nuisance parameters are at present all defined in terms of a relative uncertainty corresponding to a standard deviation in the case of Gaussian pdf. In the first implementation, a truncated Gaussian pdf can be used, but eventually we should follow the Statistics Committee's recommendation to use lognormal or gamma distribution, defined according to the recipes described in [41].

$$\pi(\mathscr{L}, \mathscr{L}_0, f_{\mathscr{L}}) \sim \exp\left[-\frac{(\mathscr{L}-\mathscr{L}_0)^2}{2\cdot(f_{\mathscr{L}}\cdot\mathscr{L}_0)^2}\right] \tag{D.7}$$

$$\pi(\Delta_m, f_m) \sim \exp\left[-\frac{(\Delta_m-1)^2}{2\cdot f_m^2}\right] \tag{D.8}$$

$$\pi(\Delta_\sigma, f_\sigma) \sim \exp\left[-\frac{(\Delta_\sigma-1)^2}{2\cdot f_\sigma^2}\right] \tag{D.9}$$

$$\pi(\mathscr{B}(m), \mathscr{B}_0(m), f_{\mathscr{B}}(m)) \sim \exp\left[-\frac{(\mathscr{B}(m)-\mathscr{B}_0(m))^2}{2\cdot(f_{\mathscr{B}}(m)\cdot\mathscr{B}_0(m))^2}\right] \tag{D.10}$$

D.5 Limit Setting

The marginalized likelihood function can be combined with the prior pdf to obtain the posterior probability density for the parameter a:

$$p(a|m) = \frac{L'(m|a)\cdot\pi(a)}{\int_0^{+\infty} L'(m|a)\cdot\pi(a)\,da} \tag{D.11}$$

We use a flat prior $\pi(a) = const.$ for the parameter a and the 95% credibility limit a_0 is defined as:

$$\int_0^{a_0} p(a|m)\,da = 0.95 \cdot \int_0^{+\infty} p(a|m)\,da \tag{D.12}$$

Appendix E

Statistics Implementation

This section is made by John Paul Chou. I used the software package he made to deal with systematic implementation. Following is the explanation made by him and I quote them here.

The method of statistical inference has been substantially updated since the previous publication of this analysis [42]. In this version, we implement a fully Bayesian treatment of both statistical and systematic uncertainties. Previously, computational and technical difficulties prevented the use of a rigorously Bayesian formalism; instead, a less formal—but still conservative—treatment was adopted. Herein we summarize our methodology, and point out the few places where we diverge from Appendix. D, which inspired our technique.

E.1 Likelihood Definition

We define a binned-likelihood function as the product of the Poisson probabilities in each bin k, with n_k observed events and μ_k expected events,

$$L(\vec{x}|a,\vec{\Delta}) = \prod_k \frac{\mu_k(a,\vec{\Delta})^{n_k} e^{-\mu_k(a,\vec{\Delta})}}{n_k!}, \tag{E.1}$$

where $\vec{x}$ is the observed data, $\vec{\Delta} \equiv (\Delta_m, \Delta_\sigma, \mathscr{L}, \mathscr{B})$ are the nuisance parameters, and a is the variable of interest, that is, the cross section times acceptance times branching fraction of the resonance signal. The four nuisance parameters in this measurement correspond to the jet-energy scale (Δ_m), the jet-energy resolution (Δ_σ), the luminosity ($\mathscr{L}$), and the

background shape ($\mathscr{B}$).

The parameters a and $\vec{\Delta}$ enter through the mean number of events μ_k according to

$$\mu_k(a,\vec{\Delta}) = \mathscr{L}\cdot a\cdot \mathscr{S}'(m_k,\Delta_m,\Delta_\sigma)\,dm_k + N_{\mathscr{B}}\cdot \mathscr{B}(m_k)\,dm_k, \tag{E.2}$$

where the first and second terms in the expression are the number of signal and background events in bin k. These are calculated for each k by evaluating the continuous probability distribution functions (PDFs) $\mathscr{S}'$ and $\mathscr{B}$ in the bin center m_k and multiplying by the bin width dm_k[1]. The expressions $\mathscr{L}\cdot a$ and $N_{\mathscr{B}}$ are effectively normalizations of the PDFs. Although the parameter $N_{\mathscr{B}}$ should also be considered a nuisance parameter, in practice the number of data points is sufficiently large that the uncertainty contributes negligibly to final result.

We incorporate the jet-energy-scale and jet-energy-resolution nuisance parameters in the signal PDF construction by the following transformation:

$$\mathscr{S}'(m_k,\Delta_m,\Delta_\sigma) = \mathscr{S}\left(\Delta_m\cdot[\Delta_\sigma\cdot(m_k-m_0)+m_0]\right), \tag{E.3}$$

where m_0 is the theoretical resonance mass. Here, $\mathscr{S}(m)$ is the original PDF measured in simulation, while variations in Δ_m and Δ_σ result in a "shifting" and "stretching" of the PDF, respectively. This transformation therefore captures the essence of these systematic uncertainties.

The background PDF is determined by fits to the data of the functional form (Eq. 3.4). In order to have a conservative estimate of the credibility interval, we fit the data to a linear combination of the background and signal PDFs. The PDF with the best fit parameters is referred to as $\mathscr{B}_0$, while the PDF with the parameters varied $\pm 1\,\sigma$ about their uncertainties

[1]The careful reader will already note several differences with Appendix. D. Most prominently, we do not integrate over the PDFs but evaluate them at the bin center. This technique is enforced by ROOFIT which approximates integrals in this way. In order for this approximation to be valid, we bin the dataset very finely—approximately 1 GeV/bin. Using an unbinned-likelihood method would avoid this approximation, but it is computationally expensive because the number of data points is $> \mathscr{O}(10^5)$.

given by the diagonalized Hessian matrix are referred to as $\mathscr{B}_{\pm}$. We treat the distinct PDFs $\mathscr{B}_{0,+,-}$ as a discrete nuisance parameter, unlike the other continuous nuisance parameters.

E.2 Nuisance Parameters

In order to set upper-limits on the unknown parameter a, the likelihood function must be marginalized, that is, the nuisance parameters must be integrated out. Formally, this is expressed as

$$L'(\vec{x}|a) = \int L(\vec{x}|a,\vec{\Delta}) \cdot \pi(\vec{\Delta})\, d^4\vec{\Delta} \tag{E.4}$$

where $\pi(\vec{\Delta})$ is the PDF of the nuisance parameters. We assume that the nuisance parameters are uncorrelated in the expression so that the PDF is factorizable,

$$\pi(\vec{\Delta}) = \pi(\Delta_m) \cdot \pi(\Delta_\sigma) \cdot \pi(\mathscr{L}) \cdot \pi(\mathscr{B}). \tag{E.5}$$

We choose a lognormal distribution to describe the PDFs for Δ_m, Δ_σ, and $\mathscr{L}$, where the median of the distribution is chosen to be the best estimate of the nuisance parameter, and the shape parameter is chosen to be $\log(\delta+1)$, where δ is the uncertainty on the nuisance parameter. The background nuisance PDF $\pi(\mathscr{B})$ is discrete and is formally expressed as

$$\pi(\mathscr{B}) = \frac{1}{3}\delta(\mathscr{B}-\mathscr{B}_0) + \frac{1}{3}\delta(\mathscr{B}-\mathscr{B}_+) + \frac{1}{3}\delta(\mathscr{B}-\mathscr{B}_-). \tag{E.6}$$

Integrating over this nuisance parameter is mathematically equivalent to taking the average likelihood function evaluated for each $\mathscr{B}$.

E.3 Limit Setting

We use Bayes' Theorem to convert the marginalized likelihood into a posterior probability density for the parameter a:

$$p(a|\vec{x}) = \frac{L'(\vec{x}|a)\cdot\pi(a)}{\int L'(\vec{x}|a)\cdot\pi(a)\,da}. \tag{E.7}$$

We choose a flat prior bounded at 0, so that

$$\pi(a) = \Theta(a). \tag{E.8}$$

Because we do not see evidence of signal, we determine the 95% credibility limit a_0 for the unknown parameter a from the equation

$$\int_{-\infty}^{a_0} p(a|\vec{x})\,da = 0.95\int_{-\infty}^{\infty} p(a|\vec{x})\,da. \tag{E.9}$$

Although we have stated the formal expression above, the posterior probability is calculated in practice through a numerical integration technique. We compute the integral by randomly sampling the nuisance parameter PDFs and evaluating the posterior probability distribution at those values. The average of the posterior distribution over the sampled nuisance parameters is equal to the marginalized posterior in the limit of large samples:

$$p(a|\vec{x}) \propto L'(\vec{x}|a)\cdot\pi(a) = \int L(\vec{x}|a,\vec{\Delta})\cdot\pi(\vec{\Delta})\,d^4\vec{\Delta}\cdot\pi(a) \tag{E.10}$$

$$\propto \frac{1}{N}\sum_{i}^{N} L(\vec{x}|a,\vec{\Delta}_i)\cdot\pi(a) \tag{E.11}$$

where $\vec{\Delta}_i$ are the nuisance parameters sampled from $\pi(\vec{\Delta})$. All nuisance parameters are sampled in this way except for $\mathscr{B}$, for which we sample each of the three $\mathscr{B}_{0,\pm}$ once for each set of N samples of the other nuisance parameters.

Appendix F

Posterior Probability Densities

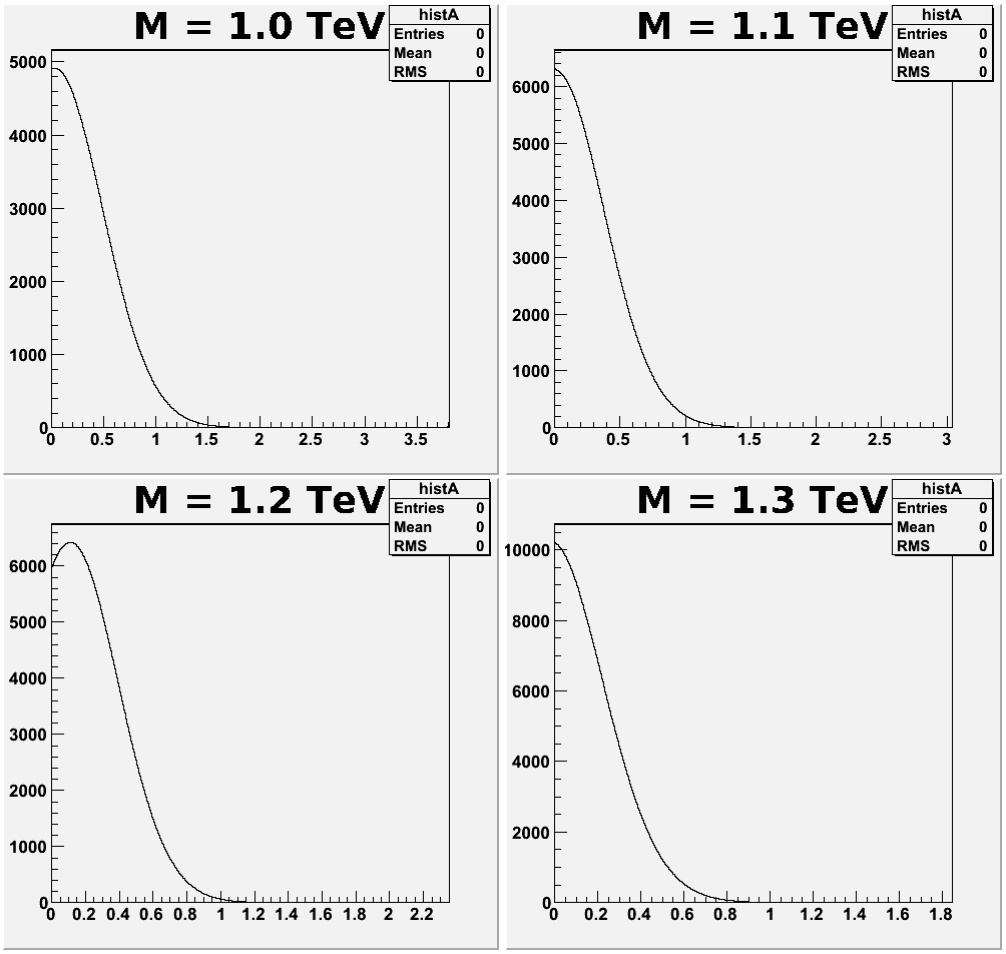

Figure F.1: Posterior probability at various excited quark resonance masses. This result include all systematics. The 95% CL upper limit is the value for which 95% of the probability corresponds to smaller cross section: the 95% quantile.

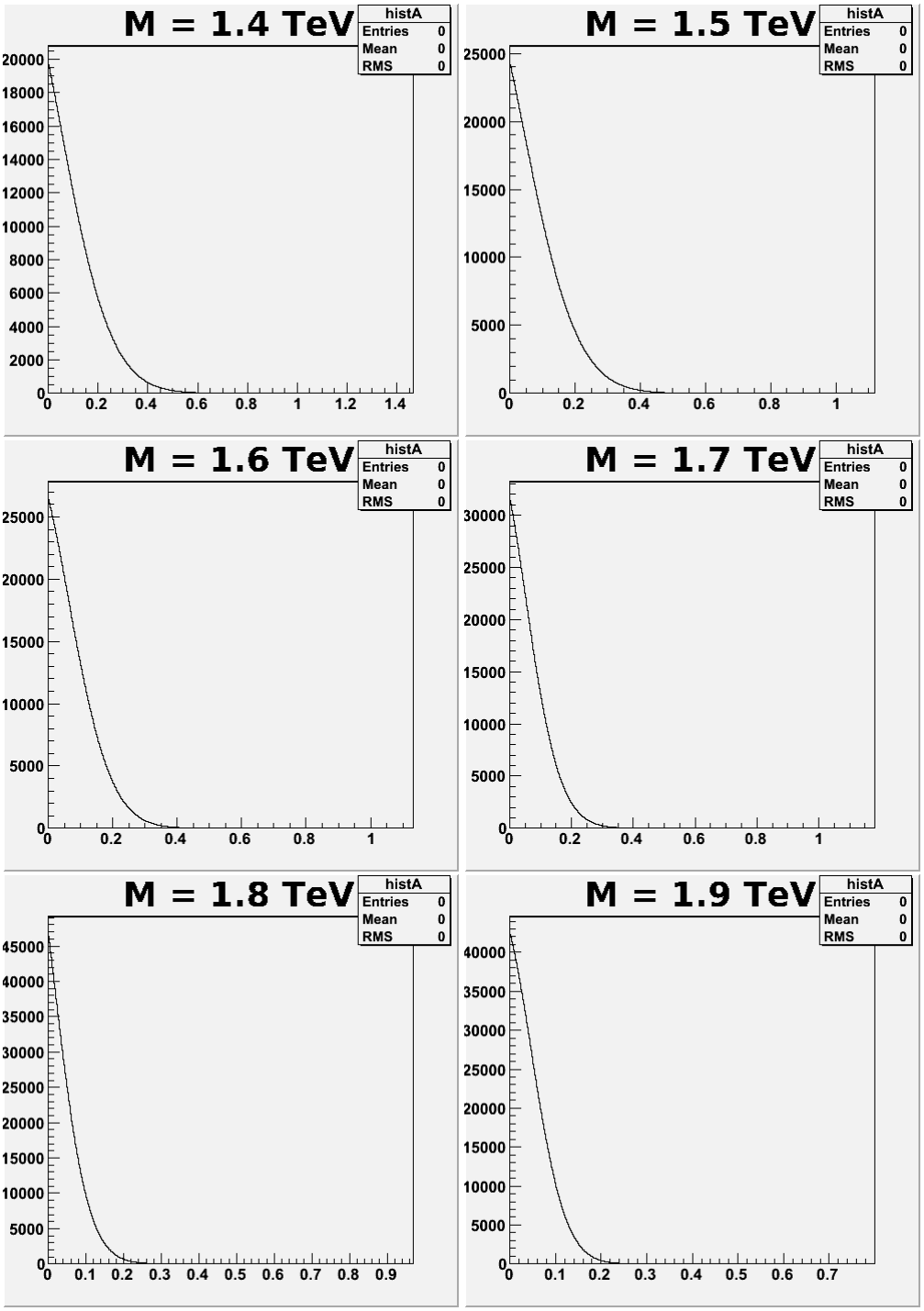

Figure F.2: Posterior probability at various excited quark resonance masses. This result include all systematics. The 95% CL upper limit is the value for which 95% of the probability corresponds to smaller cross section: the 95% quantile.

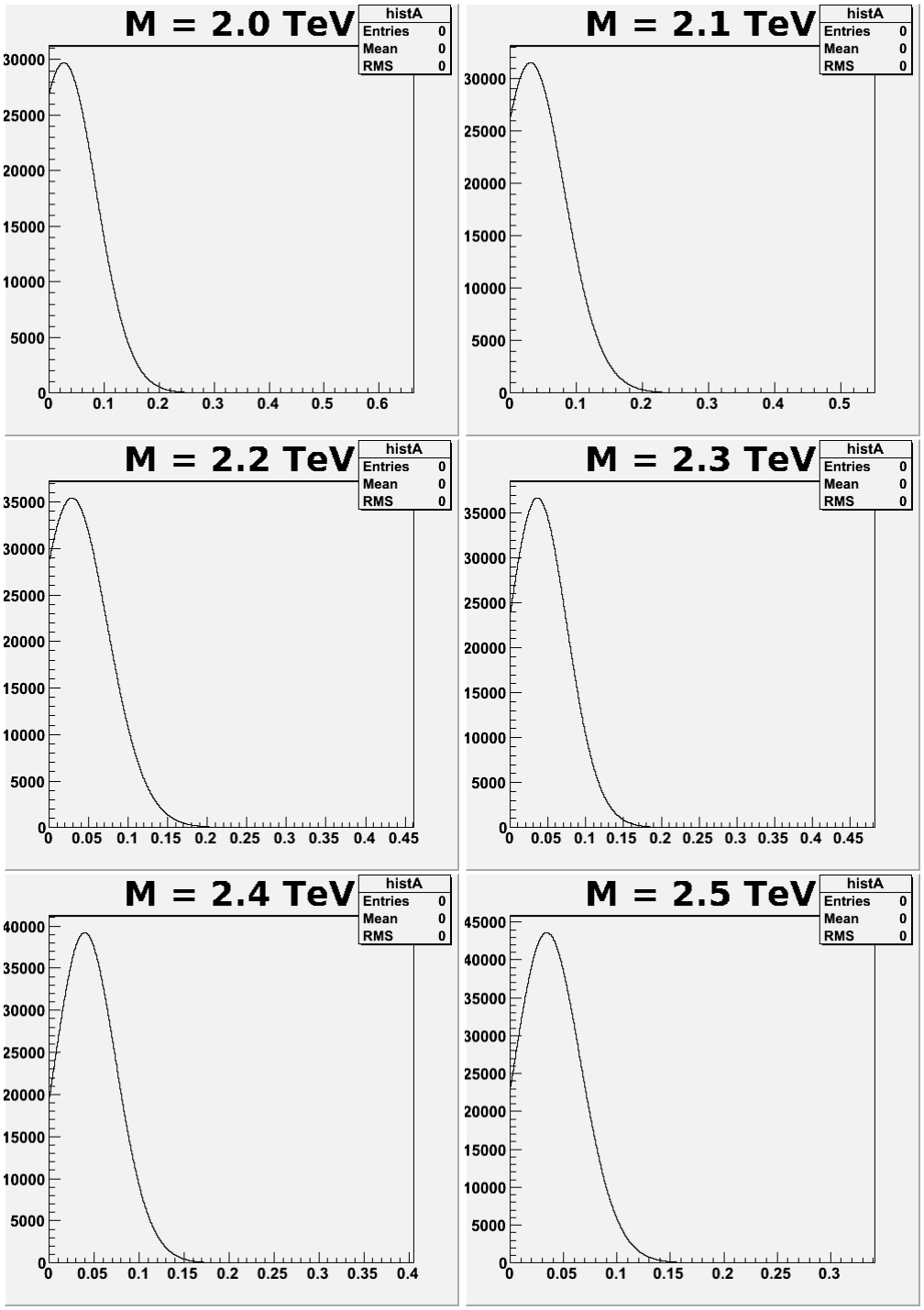

Figure F.3: Posterior probability at various excited quark resonance masses. This result include all systematics. The 95% CL upper limit is the value for which 95% of the probability corresponds to smaller cross section: the 95% quantile.

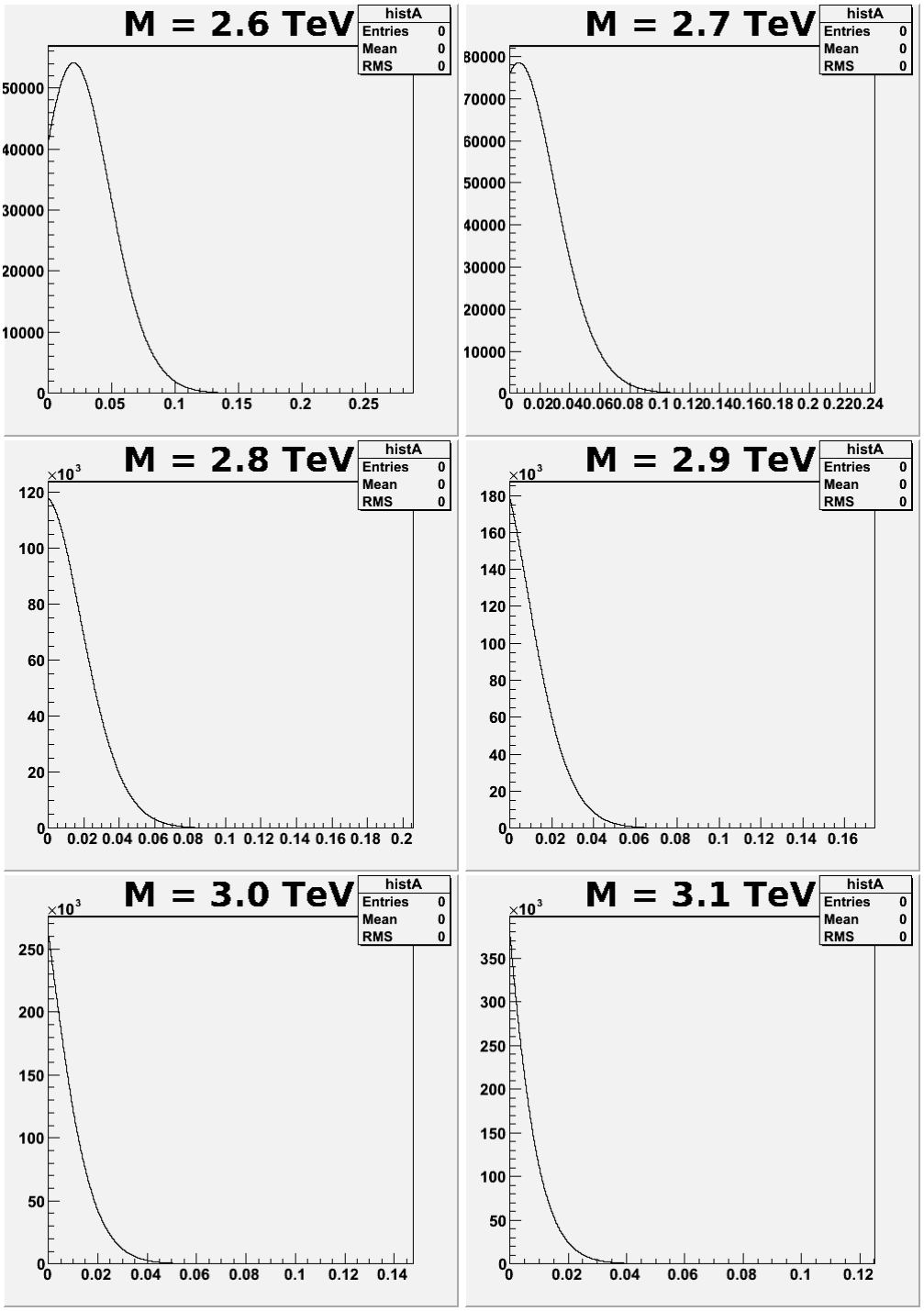

Figure F.4: Posterior probability at various excited quark resonance masses. This result include all systematics. The 95% CL upper limit is the value for which 95% of the probability corresponds to smaller cross section: the 95% quantile.

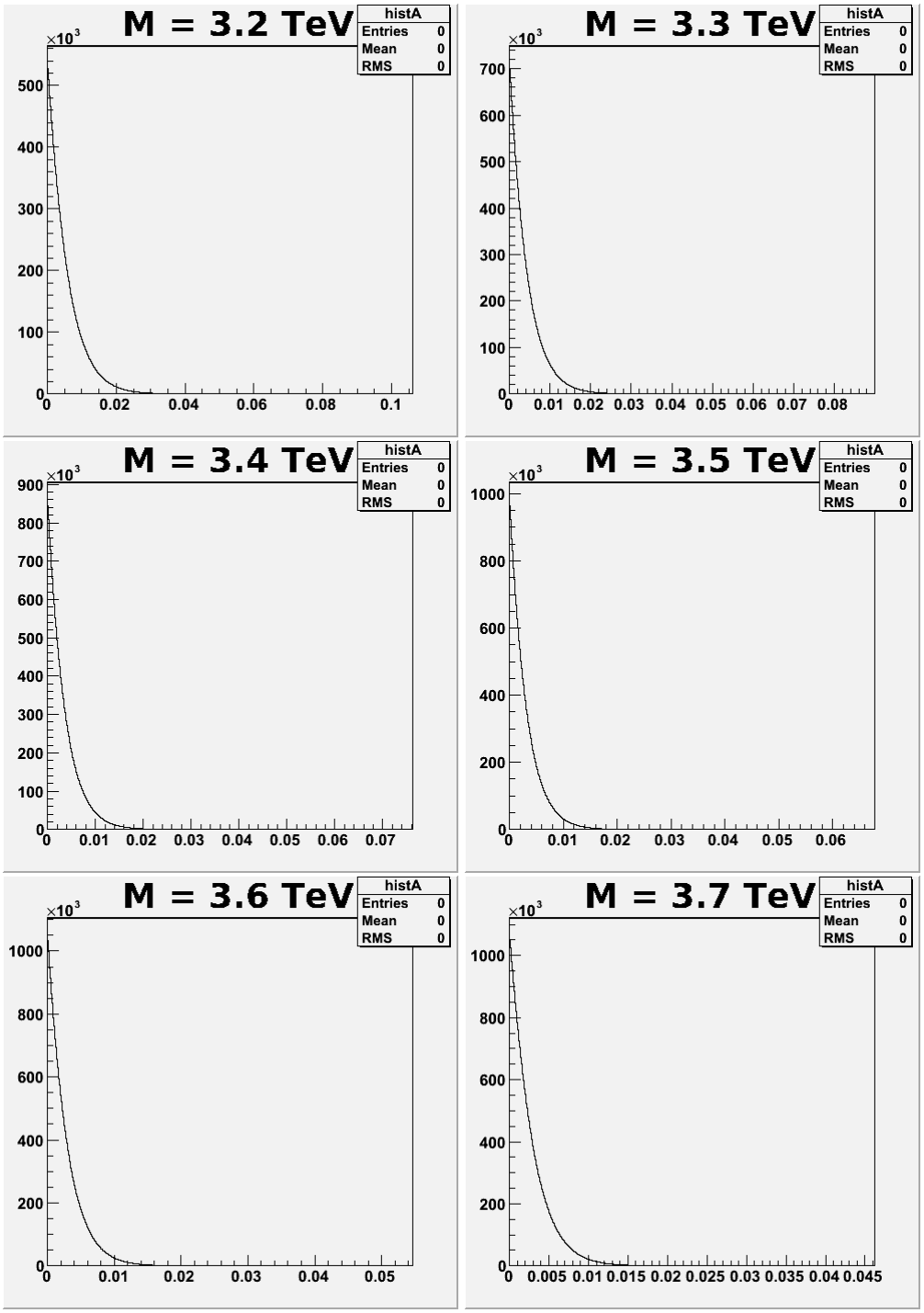

Figure F.5: Posterior probability at various excited quark resonance masses. This result include all systematics. The 95% CL upper limit is the value for which 95% of the probability corresponds to smaller cross section: the 95% quantile.

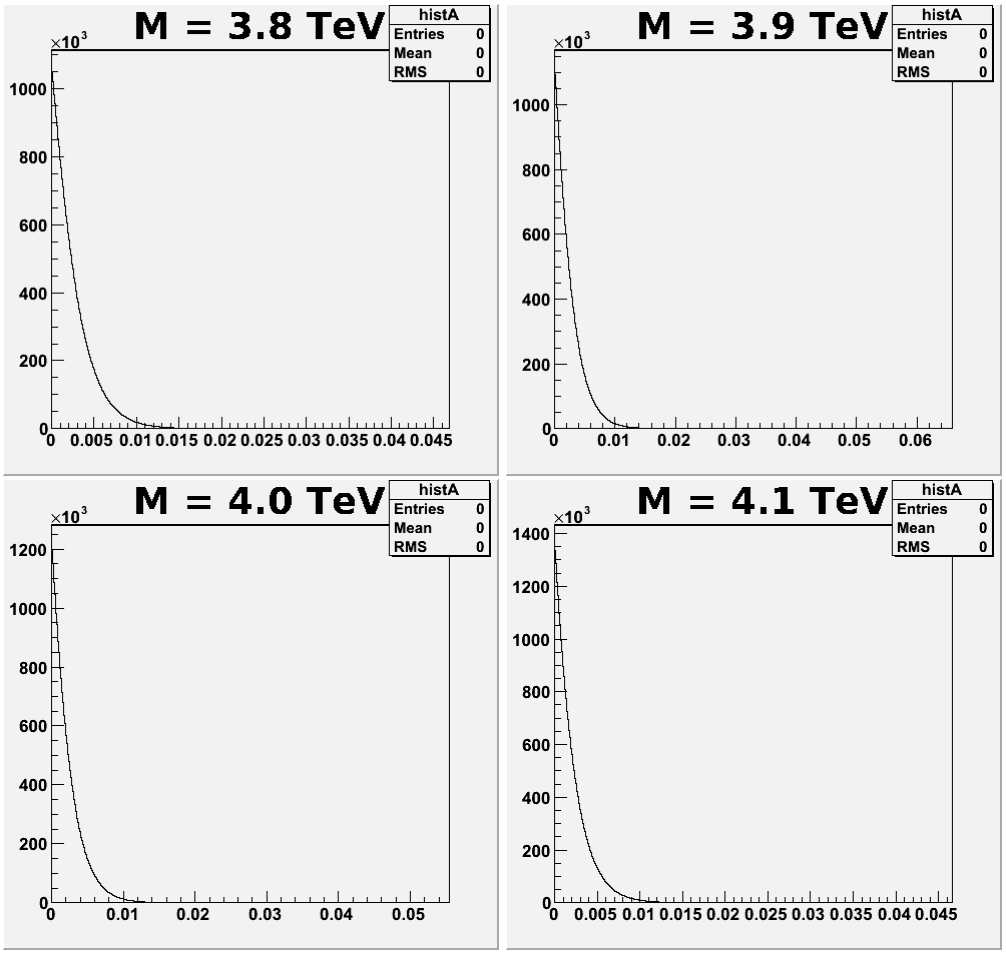

Figure F.6: Posterior probability at various excited quark resonance masses. This result include all systematics. The 95% CL upper limit is the value for which 95% of the probability corresponds to smaller cross section: the 95% quantile.

Table F.1: Best cross section values from fit for each resonance mass.

Resonance Mass (TeV)	best fit cross section for qq (pb)	best fit cross section for qg (pb)	best fit cross section for gg (pb)
1.0	0.008501 ± 0.6013	0.01450 ± 0.6158	0.02126 ± 0.6735
1.1	$2.080e^{-05} \pm 0.4613$	0.01187 ± 0.5290	0.04085 ± 0.4764
1.2	0.1403 ± 0.2494	0.1187 ± 0.2698	0.09215 ± 0.3106
1.3	0.03377 ± 0.2945	0.01794 ± 0.2922	0.03362 ± 1.077
1.4	$3.086e^{-08} \pm 0.07857$	$7.753e^{-10} \pm 0.09932$	$2.152e^{-09} \pm 0.1670$
1.5	$7.414e^{-09} \pm 0.07459$	$8.893e^{-10} \pm 0.08724$	$7.991e^{-12} \pm 0.1224$
1.6	$1.958e^{-07} \pm 0.07692$	$1.087e^{-09} \pm 0.08139$	$1.018e^{-09} \pm 0.1025$
1.7	$1.528e^{-05} \pm 0.09349$	$5.231e^{-07} \pm 0.09692$	$4.031e^{-07} \pm 0.1507$
1.8	$6.200e^{-08} \pm 0.03013$	$4.578e^{-08} \pm 0.04055$	$7.571e^{-09} \pm 0.06565$
1.9	$4.016e^{-07} \pm 0.03595$	$8.095e^{-08} \pm 0.04449$	$3.414e^{-08} \pm 0.06023$
2.0	0.02212 ± 0.04319	0.02397 ± 0.05598	0.02424 ± 0.07518
2.1	0.01266 ± 0.04045	0.02296 ± 0.04834	0.03476 ± 0.06361
2.2	0.01928 ± 0.03231	0.02655 ± 0.03955	0.03160 ± 0.05616
2.3	0.03627 ± 0.03011	0.04456 ± 0.03577	0.05604 ± 0.04918
2.4	0.04281 ± 0.02572	0.05005 ± 0.03074	0.06608 ± 0.04213
2.5	0.03464 ± 0.02193	0.04186 ± 0.02645	0.05891 ± 0.03643
2.6	0.01571 ± 0.01844	0.02221 ± 0.02256	0.03210 ± 0.03069
2.7	0.00724 ± 0.01555	0.01000 ± 0.01903	0.01387 ± 0.02506
2.8	0.009508 ± 0.01294	0.01012 ± 0.01589	0.01225 ± 0.02112
2.9	0.007164 ± 0.01082	0.007218 ± 0.01284	0.009048 ± 0.01739
3.0	0.001450 ± 0.006696	0.00059145 ± 0.0125	0.001116 ± 0.01925
3.1	$3.357e^{-11} \pm 0.003912$	$2.745e^{-10} \pm 0.005509$	$4.265e^{-10} \pm 0.009012$
3.2	$7.434e^{-10} \pm 0.001959$	$1.031e^{-08} \pm 0.002770$	$3.295e^{-08} \pm 0.004290$
3.3	$3.279e^{-08} \pm 0.001536$	$1.544e^{-08} \pm 0.001959$	$1.018e^{-13} \pm 0.002855$
3.4	$2.581e^{-08} \pm 0.001276$	$4.044e^{-08} \pm 0.001692$	$2.034e^{-08} \pm 0.002404$
3.5	$4.008e^{-14} \pm 0.001203$	$6.509e^{-14} \pm 0.001577$	$1.586e^{-07} \pm 0.002257$
3.6	$2.654e^{-12} \pm 0.001238$	$5.670e^{-13} \pm 0.001579$	$1.542e^{-07} \pm 0.002122$
3.7	$1.163e^{-10} \pm 0.001378$	$2.765e^{-13} \pm 0.001687$	$2.288e^{-08} \pm 0.002156$
3.8	$3.583e^{-13} \pm 0.001387$	$4.006e^{-12} \pm 0.001713$	$4.225e^{-07} \pm 0.002245$
3.9	$1.053e^{-10} \pm 0.001082$	$5.032e^{-14} \pm 0.001391$	$4.922e^{-08} \pm 0.001791$
4.0	$1.862e^{-08} \pm 0.0009348$	$1.635e^{-07} \pm 0.001220$	$2.309e^{-07} \pm 0.001563$
4.1	$2.040e^{-10} \pm 0.0008661$	$1.212e^{-08} \pm 0.001083$	$5.729e^{-10} \pm 0.001327$